Development and Implementation of a Cyclic Plasticity Model with Thermal Softening for Hot Work Tool Steel

DISSERTATION

zur Erlangung des akademischen Grades

Doktoringenieur
(Dr.-Ing.)

von Andreas Jilg, M.Sc.
geb. am 17. Januar 1988 in Wolfach
genehmigt durch die Fakultät für Maschinenbau
der Otto-von-Guericke-Universität Magdeburg

Gutachter:
Prof. Dr.-Ing. habil. Dr. h.c. mult. Holm Altenbach
Prof. Dr.-Ing. habil. Manja Krüger
Prof. Dr.-Ing. Thomas Seifert

Promotionskolloquium am 28. Juni 2019

Declaration of Honor

"I hereby declare that I produced this thesis without prohibited external assistance and that none other than the listed references and tools have been used. I did not make use of any commercial consultant concerning graduation. A third party did not receive any nonmonetary perquisites neither directly nor indirectly for activities which are connected with the contents of the presented thesis.

All sources of information are clearly marked, including my own publications.

In particular I have not consciously:

- Fabricated data or rejected undesired results
- Misused statistical methods with the aim of drawing other conclusions than those warranted by the available data
- Plagiarized data or publications
- Presented the results of other researchers in a distorted way

I do know that violations of copyright may lead to injunction and damage claims of the author and also to prosecution by the law enforcement authorities. I hereby agree that the thesis may need to be reviewed with an electronic data processing for plagiarism.

This work has not yet been submitted as a doctoral thesis in the same or a similar form in Germany or in any other country. It has not yet been published as a whole."

Andreas Jilg September 20, 2019

Kurzfassung

Warmumformwerkzeuge unterliegen während des Betriebes komplexen thermischen und mechanischen Beanspruchungen. In kritischen Bereichen können dadurch lokal Spannungen entstehen, die die Fließgrenze überschreiten. Bei der Serienproduktion führt dies zu zyklischen plastischen Verformungen und zu thermomechanischer Ermüdung, welche die Lebensdauer der Warmumformwerkzeuge maßgeblich beeinflussen kann.

Um den hohen Belastungen standzuhalten, werden die Warmumformwerkzeuge typischerweise aus vergüteten martensitischen Warmarbeitsstählen hergestellt. Während die Anlasstemperaturen der Werkzeugstähle gewöhnlich im Bereich zwischen 400 und 600 °C liegen, können die Stähle während der Warmformung sogar noch höhere Temperaturen ausgesetzt sein und daher durch Änderung der Mikrostruktur entfestigen.

Daher werden in dieser Arbeit die temperaturabhängigen zyklischen Materialeigenschaften des häufig verwendeten Warmarbeitsstahls 1.2367 (X38CrMoV5-3) bei verschiedenen Auslagerungszuständen untersucht. Zu diesem Zweck werden Härtemessungen durchgeführt. Des Weiteren werden durch das Institut für Umformtechnik und Umformmaschinen (IFUM) Versuchsergebnisse aus zyklischen Versuchen bei Temperaturen im Bereich von 20 °C (Raumtemperatur) bis 650 °C bereitgestellt. Zur Beurteilung der zeit- und temperaturabhängigen Entfestigung während des Auslagerns, wird ein kinetisches Modell zur Beschreibung der mittleren Teilchengröße von Sekundärkarbiden (Ostwaldreifung) entwickelt. Darüber hinaus werden sowohl mechanismenbasierte als auch phänomenologische Beziehungen für die zyklischen mechanischen Eigenschaften des Ramberg-Osgood-Modells in Abhängigkeit von der Karbidgröße und der Temperatur eingeführt. Aus den ermittelten Materialeigenschaften des kinetischen und mechanischen Modells lassen sich die gemessenen Spannungs-Dehnungs-Hysteresen für unterschiedliche Temperaturen und Auslagerungszustände gut beschreiben. Zudem eignet sich das Modell zur Einbindung in fortschrittliche mechanismenbasierte Lebensdauermodelle.

Da sich das Ramberg-Osgood-Modell nicht für Berechnung mit der Finite-Elemente-Methode (FEM) eignet, wird zudem ein tempe-

raturabhängiges inkrementelles zyklisches Plastizitätsmodell für den Warmarbeitsstahl vorgestellt. Somit kann die Entfestigung durch Teilchenvergröberung bei der Finite-Elemente-Berechnung berücksichtigt werden. Das Plastizitätsmodell nutzt Rückspannungen zur Beschreibung des Bauschinger-Effekts. Es ist über Subroutinen in das Finite-Elemente-Programm ABAQUS für implizite Integration (als UMAT bezeichnete Subroutine) und explizite Integration (als VUMAT bezeichnete Subroutine) implementiert.

Das implementierte Modell wird zur Berechnung eines exemplarischen Warmumformprozesses verwendet um die Auswirkungen der Entfestigung durch Teilchenvergröberung zu beurteilen. Dabei zeigt sich, dass die thermische Entfestigung durch hohe Temperaturen, die über eine längere Zeit an einem mechanisch hochbelasteten Bereich auftritt, einen großen Einfluss auf die plastische Verformung hat. Bleibt dieser Effekt bei der Werkzeugauslegung unberücksichtigt, kann es zu einem unerwarteten Werkzeugausfall kommen, der einen Stillstand der Produktion verursacht.

Abstract

Hot working tools are subjected to complex thermal and mechanical loads during service. Locally, the stresses can exceed the material's yield strength in highly loaded areas. During production, this causes cyclic plastic deformation and thus thermomechanical fatigue, which can significantly shorten the lifetime of hot working tools. To sustain this high loads, the hot working tools are typically made of tempered martensitic hot work tool steels. While the annealing temperatures of the tool steels usually lie in the range of 400 to 600 °C, the steels may experience even higher temperatures during hot working, resulting in softening of the material due to changes in microstructure.

Therefore, the temperature-dependent cyclic mechanical properties of the frequently used hot work tool steel 1.2367 (X38CrMoV5-3) after tempering are investigated in this work. To this end, hardness measurements are performed. Furthermore, the Institute of Forming Technology and Machines (IFUM) provides test results from cyclic tests at temperatures ranging from 20 °C (room temperature) to 650 °C. To describe the observed time- and temperature-dependent

softening during tempering, a kinetic model for the evolution of the mean size of secondary carbides based on Ostwald ripening is developed. In addition, both mechanism-based and phenomenological relationships for the cyclic mechanical properties of the Ramberg-Osgood model depending on carbide size and temperature are proposed. The stress-strain hysteresis loops measured at different temperatures and after different heat treatments can be well described with the proposed kinetic and mechanical model. Furthermore, the model is suitable for integration in advanced mechanism-based lifetime models.

However, since the Ramberg-Osgood model is not suitable for finite element implementation, a temperature-dependent incremental cyclic plasticity model is presented as well. Thus, softening due to particle coarsening can be applied in the finite element method (FEM). Therefore, a kinetic model is coupled with a cyclic plasticity model including kinematic hardening. The plasticity model is implemented via subroutines in the finite element program ABAQUS for implicit integration (subroutine called UMAT) and explicit integration (subroutine called VUMAT).

The implemented model is used for the simulation of an exemplary hot working process to assess the effects of softening due to particle coarsening. It shows that the thermal softening at high temperatures, which occur over a long time at a mechanically highly loaded area, has a great influence. If this influence is not considered in tool design, an unexpected tool failure might occur bringing the production to a standstill.

Contents

Notation

Bold letters indicate vectors and tensors. Fourth order tensors are indicated in blackboard bold. The identity tensors are Roman numerals, $\mathbf{I}$ for the second identity and $\mathbb{I}$ for the fourth identity tensor. Einstein convection, which sums over double occurring indices

$$\sum_{i=1}^{n} a_i b_i = a_i b_i$$

is used. Each dot between vectors and tensors indicates the presence of one Kronecker delta

$$\delta_{ij} = \begin{cases} 0 & \text{if } i \neq j \\ 1 & \text{if } i = j \end{cases} .$$

The following notations will be used for vector and tensor operations:

scalar product of two vectors $\boldsymbol{a} \cdot \boldsymbol{b}$

$$c = a_i b_i = a_i b_j \delta_{ij}$$

scalar product of two second order tensors $\boldsymbol{A} : \boldsymbol{B}$

$$c = A_{ij} B_{ij} = A_{ij} B_{kl} \delta_{ik} \delta_{jl}$$

inner product of two second order tensors $\boldsymbol{A} \cdot \boldsymbol{B}$

$$C_{il} = A_{ij} B_{jl} = A_{ij} B_{kl} \delta_{jk}$$

tensor product of two vectors $\boldsymbol{a} \otimes \boldsymbol{b}$

$$C_{ij} = a_i b_j$$

other product of second order tensor and vector $\boldsymbol{A} \cdot \boldsymbol{b}$

$$c_i = A_{ij} b_j = A_{ij} b_k \delta_{jk}$$

other product of fourth order and second order tensor $\mathbb{A} : \boldsymbol{B}$

$$C_{ij} = \mathbb{A}_{ijkl} B_{kl} = \mathbb{A}_{ijkl} B_{mn} \delta_{km} \delta_{ln}.$$

Additional notations for vectors are

nabla operator:	$\nabla = \left(\frac{\partial}{\partial x_1}, \cdots, \frac{\partial}{\partial x_n}\right)$
gradient:	$\mathrm{grad}(\boldsymbol{a}) = (\nabla \otimes \boldsymbol{a})^{\mathrm{T}}$
divergence:	$\mathrm{div}(\boldsymbol{a}) = \nabla \cdot \boldsymbol{a}$.

Additional notations for second order tensors are

symmetric part:	$\mathrm{sym}(\boldsymbol{A}) = \frac{1}{2}\left(\boldsymbol{A} + \boldsymbol{A}^{\mathrm{T}}\right)$
skew symmetric part:	$\mathrm{skew}(\boldsymbol{A}) = \frac{1}{2}\left(\boldsymbol{A} - \boldsymbol{A}^{\mathrm{T}}\right)$
trace:	$\mathrm{tr}(\boldsymbol{A}) = A_{ii}$
deviator:	$\mathrm{dev}(\boldsymbol{A}) = \boldsymbol{A} - \frac{1}{3}\mathrm{tr}(\boldsymbol{A})\mathbf{I}$.

Further notations:

time derivative:	$\dot{(\cdot)} = \frac{\mathrm{d}(\cdot)}{\mathrm{d}t}$
exponential integral:	$\mathrm{Ei}(x) = -\int_{-x}^{\infty} \frac{e^{-t}}{t}\,\mathrm{d}t$
natural logarithm:	$\ln(x) = \log_e(x)$ with the Euler's number e
Macaulay brackets:	$\langle x \rangle = \frac{1}{2}(a + \lvert a \rvert)$.

Chapter 1

Introduction

1.1 Motivation

Hot working is a reliable and relatively economic manufacturing process for metal parts. It is a process in which the metal parts are plastically formed above their recrystallization temperature. In the case of hot forging of steel the temperature of the material lies between 1000 and 1250 °C [DB10, p. 584]. In this state the blank is relatively soft, since the recrystallization produces new grain structure, which degrades dislocations [DeG03, pp. 387–389]. This allows the production of complex parts with high strength in a very short time.

In die forging, the tools consist of a punch at the top and a die at the bottom. They can be made of several parts and the forming process itself can be separated into stages. The tools partly contain the negative shape of the desired product. After external heating, the blank is inserted between the tools and the punch pushes the hot blank into the die to gain the desired shape.

During hot working, the tools are exposed to thermal and mechanical loads resulting in highly stressed regions such as small radii in die cavities. To sustain high loads, the hot work tools are typically made of martensitic hot work tool steels that are hardened and annealed in order to obtain a microstructure of the material resulting in the desired combination of strength, toughness and thermal stability.

However, in the highly stressed regions of forming tools local cyclic plastic deformations are still possible. Thus, temperature-dependent cyclic mechanical material properties of the hot work tool steels are required to assess the forming tools with respect to their fatigue life.

While temperatures for annealing of the tool steels usually lie in the range between 400 and 600 °C, the steels may experience even higher temperatures during hot working. According to the Tammann-rule, 40 % of the melting temperature can be assumed for an estimation of the recrystallization temperature [Sch91, p. 130]. Hence, a further evolution of the mechanical material properties during service is expected. Microstructural changes during tempering as coarsening of strengthening particles (e.g. secondary carbides) known as Ostwald ripening result in softening of the material [CSE$^+$02, ZDB04, HLWZ06, MBGA09]. If this softening is not considered in tool design, unexpected tool failures could occur.

In industry, usually pure linear elastic material behavior is assumed in finite element calculations of hot working tools. Furthermore, the tool temperature is usually assumed constant and not determined by a thermomechanically coupled simulation. Due to these simplifications, the complex material behavior can only be partially described, which can lead to an inappropriate tool design. Hence, there is a demand for models that describe the temperature-dependent cyclic mechanical properties even after softening at different tempering times and temperatures.

Instead of using a purely phenomenological description of softening, mechanism-based models could be used. The mechanism-based models allow the description of the evolution of material properties on the basis of the evolution of measurable microstructural quantities (e.g. mean particle size) with a relatively low number of material properties. As long as the mechanisms do not change, the models are often able to describe the material behavior also for loading conditions that are outside of the range of conditions used for the determination of the material properties. Models describing the coarsening of strengthening particles and reduction of the dislocation density are used in [EL88] to evaluate softening of a hot work tool steel. The coarsening kinetics of particles is considered in describing the loss of hardness during thermal loading in [CSE$^+$02]. However, in the latter two references the kinetic models are not incorporated into a model

to describe the time- and temperature-dependent cyclic mechanical material properties depending on the current tempering state.

1.2 Aim

It is the aim of the present work to develop and implement advanced material models including integrated descriptions of the mechanical behavior and microstructural changes for the frequently used hot work tool steel 1.2367 (X38CrMoV5-3). On the one hand, the development of an incremental cyclic plasticity model for the implementation in finite element programs is needed. On the other hand, a plasticity model for the integration in mechanism-based models for thermomechanical fatigue life prediction has to be developed. This enables to asses the effect of softening on the thermomechanical fatigue life of hot work tools.

1.3 Structure

The thesis is structured as follows: In the next chapter, the theoretical foundations required for this work are presented. Afterwards, the material behavior of hot work tool steels and existing material models, that have already been used by other researchers are presented in chapter 3. Then, the experimental material testing of the investigated steel is described in chapter 4. In chapter 5, which is a main contribution of this work, the material models including the kinetic model, the Ramberg-Osgood model and the incremental cyclic plasticity model are described. The cyclic mechanical material properties of the Ramberg-Osgood model are considered because they are the basic properties entering a mechanism-based model for thermomechanical fatigue crack growth and life prediction that is well established for hot parts in internal combustion engines and exhaust systems, e.g. [SR10, SSS$^+$10]. However, the Ramberg-Osgood model cannot be used in finite element calculations, where incremental models are needed. Hence, an incremental cyclic plasticity model including time- and temperature-dependent softening is additionally developed.

Chapter 6 deals with the model's implementation in the finite element program ABAQUS using the ABAQUS subroutines VUMAT for an explicit calculation and UMAT for an implicit one. After the model is applied to a die forging simulation, the results obtained are discussed in chapter 8. Finally, the works summary and the conclusions can be found in chapter 9.

Contents of this thesis are partly published in [JSB17, JS18a, JS18b].

Chapter 2

Theoretical foundations

In this chapter, theoretical foundations needed for this work are presented. First, the linear elasticity is described. Afterwards, elements of plasticity that are used for the materials description are shown. The special focus lies on the Ramberg-Osgood model and on incremental plasticity models. Finally, numerical methods, that will be used in this work are presented. In particular, the Newton-Raphson method, the FEM and gradient based optimization is described. The following presentations refer to the works [Alt18, Nas15, Sei15, Sei17, Wri08], where more detailed explanations can be found.

2.1 Linear elasticity

Linear elasticity is a branch of continuum mechanics, where a body is considered as the sum of its connected points. The displacement $\boldsymbol{u}$ of a point from an initial $\boldsymbol{X}$ to the current status $\boldsymbol{x}$ can be calculated by

$$\boldsymbol{u} = \boldsymbol{x} - \boldsymbol{X}. \tag{2.1}$$

Since the tools have to withstand several hot working cycles, small strains $\|\mathrm{grad}(\boldsymbol{u}) \ll 1\|$ can be assumed. Therefore, the infinitesimal strain tensor is used

$$\boldsymbol{\varepsilon} = \frac{1}{2}(\mathrm{grad}(\boldsymbol{u}) - \mathrm{grad}(\boldsymbol{u})^{\mathrm{T}}). \tag{2.2}$$

Now, the Cauchy stress tensor can be calculated by

$$\boldsymbol{\sigma} = \mathbb{C} : \varepsilon \tag{2.3}$$

with the continuum tangent $\mathbb{C}$.

For the purely isotropic (invariance to rotation) elastic case, equation (2.3) can be written as

$$\boldsymbol{\sigma} = \mathbb{C}^{\mathrm{e}} : \varepsilon^{\mathrm{e}} \tag{2.4}$$

with the isotropic elasticity tensor

$$\mathbb{C}^{\mathrm{e}} = \frac{E\nu}{(1-2\nu)(1+\nu)}\mathbf{I} \otimes \mathbf{I} + \frac{E}{1+\nu}\mathbb{I}\mathbb{I}, \tag{2.5}$$

the elastic strain $\boldsymbol{\varepsilon}^{\mathrm{e}}$, and the elastic properties Young's modulus E and Poisson's ratio ν. This relationship is also known as Hooke's law. The isotropic elasticity tensor can also be calculated by

$$\mathbb{C}^{\mathrm{e}} = \lambda_L \mathbf{I} \otimes \mathbf{I} + 2\mu_L \mathbb{I}\mathbb{I} \tag{2.6}$$

with the Lamé constants λ_L and μ_L, which can be calculated from the Young's modulus E and Poisson's ratio ν, compare equation (2.5).

2.2 Elements of plasticity

The mathematical description of the mechanical behavior of the investigated hot work tool steel is a main contribution of this work. Elastic-plastic material properties are to be considered, so that the elements of plasticity used in this work are addressed in this section. The total strain $\boldsymbol{\varepsilon}$ is additively decomposed into an elastic $\boldsymbol{\varepsilon}^{\mathrm{e}}$, a plastic $\boldsymbol{\varepsilon}^{\mathrm{p}}$ and a thermal part $\boldsymbol{\varepsilon}^{\mathrm{th}}$:

$$\boldsymbol{\varepsilon} = \boldsymbol{\varepsilon}^{\mathrm{e}} + \boldsymbol{\varepsilon}^{\mathrm{p}} + \boldsymbol{\varepsilon}^{\mathrm{th}}. \tag{2.7}$$

The thermal strain rate is given by

$$\dot{\boldsymbol{\varepsilon}}^{\mathrm{th}} = \alpha^{\mathrm{th}} \dot{\Theta} \mathbf{I} \tag{2.8}$$

with the temperature-dependent thermal expansion coefficient α^{th} and the time derivative of the temperature $\dot{\Theta}$. Assuming a constant thermal expansion coefficient in the temperature range ΔT, the thermal strain can be calculated by

$$\boldsymbol{\varepsilon}^{\mathrm{th}} = \alpha^{\mathrm{th}} \Delta T \mathbf{I}. \tag{2.9}$$

For the determination of plastic strain the Ramberg-Osgood plasticity and incremental plasticity is presented in the following sections. The Ramberg-Osgood plasticity is used, since it can be well integrated in mechanism-based lifetime models. Whereas the incremental plasticity is needed for implementation in finite element programs.

2.2.1 Ramberg-Osgood plasticity

Ramberg-Osgood plasticity describes nonlinear material with an explicit relation between stress and strain [RO43]. This implies, that the model has no history dependency. The plastic flow curve is described by power law hardening. In the uniaxial case, the plastic part of the Ramberg-Osgood model is described by

$$\varepsilon^{\mathrm{p}} = K \left(\frac{\sigma}{E} \right)^{\frac{1}{n}} \tag{2.10}$$

with the Young's modulus E and the material parameters K and n. With the $0.2\,\%$ offset yield strength $R_{\mathrm{p0.2}}$ the parameter K can be calculated

$$K = 0.002 \left(\frac{E}{R_{\mathrm{p0.2}}} \right)^{\frac{1}{n}}. \tag{2.11}$$

The integration of K in equation (2.10) leads to

$$\varepsilon^{\mathrm{p}} = 0.002 \left(\frac{\sigma}{R_{\mathrm{p0.2}}} \right)^{\frac{1}{n}}. \tag{2.12}$$

In the three-dimensional case for incompressible materials the plastic strain tensor is

$$\boldsymbol{\varepsilon}^{\mathrm{p}} = \frac{3}{2} 0.002 \left(\frac{\sigma_{\mathrm{eq}}}{R_{\mathrm{p0.2}}} \right)^{\left(\frac{1}{n}-1\right)} \frac{\mathrm{dev}(\boldsymbol{\sigma})}{R_{\mathrm{p0.2}}} \tag{2.13}$$

with the von Mises stress (also known as equivalent stress)

$$\sigma_{\mathrm{eq}} = \sqrt{\frac{3}{2}} \| \mathrm{dev}(\boldsymbol{\sigma}) \|. \tag{2.14}$$

For cyclic plasticity, the Ramberg-Osgood model is referenced to the reversal point. Therefore, from now on deltas of stress and strain are used with respect of the points of load reversal. Furthermore, a cyclic yield strength σ_{cy} and a cyclic hardening exponent n' is introduced. Together with Hooke's law, the cyclic Ramberg-Osgood model is given by

$$\delta\boldsymbol{\varepsilon} = \mathbb{C}^{\mathrm{e}^{-1}} : \delta\boldsymbol{\sigma} + \frac{3}{2} 0.002 \left(\frac{\delta\sigma_{\mathrm{eq}}}{\sigma_{\mathrm{cy}}} \right)^{\left(\frac{1}{n'}-1\right)} \frac{\mathrm{dev}(\delta\boldsymbol{\sigma})}{\sigma_{\mathrm{cy}}}. \tag{2.15}$$

2.2.2 Incremental plasticity

The elastic behavior is described by Hooke's law, see equation (2.4). If plastic flow in metals takes place, the von Mises yield criterion (plastic incompressibility)

$$\phi = \sqrt{\frac{3}{2}}\|\boldsymbol{\xi}\| - R \tag{2.16}$$

is equal to (plastic behavior) or greater than zero (viscoplastic behavior). R is the yield stress, which can include isotropic hardening. A backstress, which evolves with the thermomechanical load is taking into account via the von Mises stress, see equation (2.14). Therefore, the variable

$$\boldsymbol{\xi} = \operatorname{dev}(\boldsymbol{\sigma}) - \boldsymbol{\alpha} \tag{2.17}$$

is introduced. The backstress describes kinematic hardening and, thus, the Bauschinger effect, which leads to a lower flow stress after a reversal load compared to the previous flow stress. The evolution of the backstress is described by the Armstrong-Frederick kinematic hardening law [FA07]

$$\dot{\boldsymbol{\alpha}} = \frac{2}{3}C\dot{\boldsymbol{\varepsilon}}^{\mathrm{p}} - \gamma\dot{\bar{\varepsilon}}^{p}\boldsymbol{\alpha} + \frac{1}{C}\frac{\partial C}{\partial T}\dot{T}\boldsymbol{\alpha}, \tag{2.18}$$

where C and γ are temperature-dependent material properties.

The plastic part of the strain rate can be expressed in the general form

$$\dot{\boldsymbol{\varepsilon}}^{p} = \lambda \boldsymbol{N}, \tag{2.19}$$

where λ is a plastic multiplier, which corresponds to the amount of inelastic flow, and $\boldsymbol{N}$ is the flow direction, which can be calculated by the derivative of the yield criterion ϕ with respect to the stress tensor (normality rule):

$$\boldsymbol{N} = \frac{\partial \phi}{\partial \boldsymbol{\sigma}} = \sqrt{\frac{3}{2}}\frac{\boldsymbol{\xi}}{\|\boldsymbol{\xi}\|}. \tag{2.20}$$

In case of von Mises plasticity, the plastic multiplier corresponds to the accumulated plastic strain rate

$$\dot{\bar{\varepsilon}}^{\mathrm{p}} = \sqrt{\frac{2}{3}}\|\dot{\boldsymbol{\varepsilon}}^{\mathrm{p}}\| = \lambda. \tag{2.21}$$

2.3 Numerical methods

This section presents numerical methods used in this work. First, the Newton-Raphson method is described. On the one hand, it is used to calculate internal variables, see chapter 6. On the other hand, it is used for implicit finite element calculation. The FEM is a common method for continuum mechanical calculations and it is described in the following section. Thereby, the special focus lies on explicit and implicit time integration. Finally, the gradient-based optimization is described, which is a method used for parameter identification.

2.3.1 Newton–Raphson method

The Newton-Raphson method is a method for finding approximations to the roots of a function

$$f(x) = 0. \tag{2.22}$$

For this, the function is linearized at a starting point $(x_0|f(x_0))$, this means the tangent $t(x)$ is determined:

$$t(x) = f'(x_0)\,(x - x_0) + f(x_0). \tag{2.23}$$

With this tangent equation, the root is calculated to an approximation. The approximate solution then serves as the new starting point for the next iteration step. This leads to the following iteration rule:

$$x_{n+1} = x_n - \frac{f(x_n)}{f'(x_n)}. \tag{2.24}$$

In the multi-dimensional case the iteration rule is given by

$$\boldsymbol{x}_{n+1} = \boldsymbol{x}_n - (\boldsymbol{J}(\boldsymbol{x}_n))^{-1} \cdot \boldsymbol{f}(\boldsymbol{x}_n) = \boldsymbol{x}_n + \Delta\boldsymbol{x}_n \tag{2.25}$$

with the Jacobian matrix

$$\boldsymbol{J}(\boldsymbol{x}) = \frac{\partial f_i}{\partial x_j}. \tag{2.26}$$

Since the calculation of the inverse of the Jacobian matrix is numerically unfavorable, $\Delta\boldsymbol{x}_n$ is determined by solving the linear equation

$$\boldsymbol{J}(\boldsymbol{x}_n) \cdot \Delta\boldsymbol{x}_n = -\boldsymbol{f}(\boldsymbol{x}_n). \tag{2.27}$$

2.3.2 Finite element method

In hot working simulation, the tool analysis is carried out either coupled or decoupled. In the coupled analysis, the blank and the tools are modeled deformable. The coupled analysis is more realistic than the decoupled one, where the simulation is separated in two steps. First, a pure material flow simulation with rigid tools is performed. This is followed by the actual stress analysis of the tools, which are then modeled as deformable parts. The loads from material flow simulation are transferred to the tools.

Additionally, the thermodynamic problem can be calculated either thermomechanically coupled or decoupled. Since the mechanical and the thermal field influence each other, the thermomechanically coupled simulation is more realistic. For the coupled calculation, the balance law of linear momentum and the balance law of energy must be taken into account. For simplicity, the FEM is introduced on the basis of the balance law of linear momentum (here in the static case and in the strong form)

$$\operatorname{div}(\boldsymbol{\sigma}) + \varrho \boldsymbol{b} = \mathbf{0}, \tag{2.28}$$

where ϱ is the density and $\boldsymbol{b}$ is the body force per unit mass. In FEM, the weak form of the boundary value problem is used

$$\int_{\mathcal{B}} \boldsymbol{\sigma} : \operatorname{grad}(\delta \boldsymbol{u}) \mathrm{d}V - \int_{\mathcal{B}} \varrho \boldsymbol{b} \cdot \delta \boldsymbol{u} \mathrm{d}V - \int_{\partial \mathcal{B}^t} \boldsymbol{t} \cdot \delta \boldsymbol{u} \mathrm{d}a = \mathbf{0}, \tag{2.29}$$

where $\delta \boldsymbol{u}$ is a test function (virtual displacement), $\mathcal{B}$ the continuum body, and $\boldsymbol{t}$ are stress vectors on the surfaces $\partial \mathcal{B}^t$.

In the FEM the complex problem is divided in finite elements (spatial discretization), which are connected by nodes. The displacement of the nodes are the unknowns and they are summarized in the vector $\boldsymbol{u}^A$. The displacement field within an element $\boldsymbol{u}_e(\boldsymbol{x}_e)$ can be calculated by an interpolation of the individual displacements of the nodes with an interpolation function $\boldsymbol{N}_A$, resulting in

$$\boldsymbol{u}_e(\boldsymbol{x}_e) = \boldsymbol{N}_A(\boldsymbol{x}_e) \cdot \boldsymbol{u}^A. \tag{2.30}$$

This also works with the virtual displacement

$$\delta \boldsymbol{u}_e = \boldsymbol{N}_A \cdot \delta \boldsymbol{u}^A, \tag{2.31}$$

where

$$\operatorname{grad}(\delta \boldsymbol{u}) = \operatorname{grad}(\boldsymbol{N}_A) \cdot \delta \boldsymbol{u}^A = \boldsymbol{B}_A \cdot \delta \boldsymbol{u}^A. \tag{2.32}$$

Now, the equilibrium can be calculated by

$$\left[\int_{\boldsymbol{\mathcal{B}}_e} \boldsymbol{\sigma} : \boldsymbol{B}_A \mathrm{d}V - \int_{\boldsymbol{\mathcal{B}}_e} \boldsymbol{b} \cdot \boldsymbol{N}_A \varrho \mathrm{d}V - \int_{\partial \boldsymbol{\mathcal{B}}_e^t} \boldsymbol{t} \cdot \boldsymbol{N}_A \mathrm{d}a \right] \delta \boldsymbol{u}^A = \boldsymbol{0}. \tag{2.33}$$

Taking the zero product properties into account, the equilibrium of an element can be calculated by

$$\int_{\boldsymbol{\mathcal{B}}_e} \boldsymbol{\sigma} : \boldsymbol{B}_A \mathrm{d}V - \int_{\boldsymbol{\mathcal{B}}_e} \boldsymbol{b} \cdot \boldsymbol{N}_A \varrho \mathrm{d}V - \int_{\partial \boldsymbol{\mathcal{B}}_e^t} \boldsymbol{t} \cdot \boldsymbol{N}_A \mathrm{d}a = \boldsymbol{0} \tag{2.34}$$

with $\boldsymbol{\sigma}(\boldsymbol{\varepsilon}(\boldsymbol{u}))$. This equation can also be expressed in the form of $\boldsymbol{f}_{\mathrm{int}} = \boldsymbol{f}_{\mathrm{ext}}$, where the internal forces $\boldsymbol{f}_{\mathrm{int}} = \int_{\boldsymbol{\mathcal{B}}_e} \boldsymbol{\sigma} : \boldsymbol{B}_A \mathrm{d}V$ must have the same size as the external forces $\boldsymbol{f}_{\mathrm{ext}} = \int_{\boldsymbol{\mathcal{B}}_e} \boldsymbol{b} \cdot \boldsymbol{N}_A \varrho \mathrm{d}V + \int_{\partial \boldsymbol{\mathcal{B}}_e^t} \boldsymbol{t} \cdot \boldsymbol{N}_A \mathrm{d}a$. The relationship between stress and strain is defined by the material model. Finally, the relationship between displacement and strain is provided by equation (2.2).

The linearized equilibrium equations of the individual elements are assembled considering the nodal connectivity among the elements. Integrating the equations leads to a system of equations in the form of

$$\boldsymbol{R} = \boldsymbol{K}(\boldsymbol{u}) \cdot \boldsymbol{u} - \boldsymbol{P}(\boldsymbol{u}) = \boldsymbol{0}, \tag{2.35}$$

where $\boldsymbol{K}$ is the stiffness matrix and $\boldsymbol{P}$ are external forces. Since a numerical integration with a quadrature rule is used, the location of obtained stresses and strains are at integration points instead of nodal positions. The nodal solution can be calculated by an inter- and extrapolation. Using the Newton-Raphson method (section 2.3.1) the displacement can be calculated iterative by

$$\boldsymbol{u}_{n+1} = \boldsymbol{u}_n + \Delta \boldsymbol{u}, \tag{2.36}$$

where

$$\boldsymbol{K}_{\mathrm{T}} \cdot \Delta \boldsymbol{u} = \frac{\mathrm{d}\boldsymbol{R}}{\mathrm{d}\boldsymbol{u}} \cdot \Delta \boldsymbol{u} = -\boldsymbol{R} \tag{2.37}$$

with $\boldsymbol{K}_{\mathrm{T}}$ being the tangential stiffness matrix.

In the dynamic case, a term must be added to the balance law of linear momentum (2.29), since it no more equals zero. The momentum can be calculated by $\boldsymbol{I} = \varrho \boldsymbol{a}$, with the acceleration $\boldsymbol{a}$. Thus, the external forces result in

$$\boldsymbol{f}_{\text{ext}} = \int_{\boldsymbol{\mathcal{B}}_e} (\boldsymbol{b} - \boldsymbol{a}) \cdot \boldsymbol{N}_A \varrho \mathrm{d}V + \int_{\partial \boldsymbol{\mathcal{B}}_e^t} \boldsymbol{t} \cdot \boldsymbol{N}_A \mathrm{d}a. \tag{2.38}$$

Assembling and integrating the linearized equilibrium equations of the elements leads again to a system of equations. However, in the dynamic case the system is extended with a mass matrix $\boldsymbol{M}$ and a damping matrix $\boldsymbol{D}$:

$$\boldsymbol{R} = \boldsymbol{M} \cdot \ddot{\boldsymbol{u}} + \boldsymbol{K}(\boldsymbol{u}, \dot{\boldsymbol{u}}) \cdot \boldsymbol{u} + \boldsymbol{D}(\boldsymbol{u}, \dot{\boldsymbol{u}}) \cdot \dot{\boldsymbol{u}} - \boldsymbol{P}(\boldsymbol{u}, \dot{\boldsymbol{u}}) = \boldsymbol{0}. \tag{2.39}$$

This equation can be solved implicit or explicit, where no Newton iteration is needed, see sections below.

2.3.2.1 Explicit time integration

Due to time discretization in dynamic processes, time integration is required. Explicit time integration is suitable for short-term, highly nonlinear problems. In the explicit time integration, the displacements are independent from the accelerations at the current time t_{n+1}. The calculation for a two-step explicit procedure is given by

$$\boldsymbol{u}_{n+2} = \boldsymbol{u}_n + 2\Delta t \dot{\boldsymbol{u}}_{n+1} \tag{2.40}$$

with

$$\dot{\boldsymbol{u}}_{n+1} = \dot{\boldsymbol{u}}_{n-1} + 2\Delta t \ddot{\boldsymbol{u}}_n. \tag{2.41}$$

The internal forces

$$\boldsymbol{I} = \boldsymbol{D} \cdot \dot{\boldsymbol{u}} + \boldsymbol{K} \cdot \boldsymbol{u} \tag{2.42}$$

and the external forces $\boldsymbol{P}$ can be directly calculated with the variables from equation (2.40) and (2.40). The accelerations $\ddot{\boldsymbol{u}}$ at the time t_{n+1} can then be calculated by

$$\ddot{\boldsymbol{u}}_{n+1} = \boldsymbol{M}^{-1} \cdot (\boldsymbol{P}_{n+1} - \boldsymbol{I}_{n+1}). \tag{2.43}$$

Since the explicit method works without an iteration procedure, the computing effort for one time increment is small. Thus, the dynamic problem can be solved efficiently with a large number of small time increments. However, when the time increments exceed the stable time increment

$$\Delta t_{\text{stable}} = l\sqrt{\frac{\rho}{E}} \tag{2.44}$$

with the smallest element length l, the calculation becomes unstable. Therefore, the number of time increments is usually much larger compared to implicit simulation. Examples for explicit simulations are crash simulations or quasistatic analyses such as forming processes with complex contact conditions and nonlinear material behavior.

2.3.2.2 Implicit time integration

In implicit time integration, the displacements and velocities are dependent on the accelerations at the current time t_{n+1}. The calculation for a one-step implicit procedure is given by

$$\boldsymbol{u}_{n+1} = \boldsymbol{u}_n + \Delta t \dot{\boldsymbol{u}}_n + \frac{\Delta t^2}{2}\ddot{\boldsymbol{u}}_{n+1} \tag{2.45}$$

with

$$\dot{\boldsymbol{u}}_{n+1} = \dot{\boldsymbol{u}}_n + \frac{\Delta t}{2}\left(\ddot{\boldsymbol{u}}_n + \ddot{\boldsymbol{u}}_{n+1}\right). \tag{2.46}$$

For implicit time integration an iterative solution is required, see section 2.3.1. It has unconditional numerical stability compared to explicit integration. Therefore, linear and slight non-linear problems, can be efficiently solved. However, the implicit integration involves a high amount of computing effort per time step. High nonlinearities can cause convergence problems leading to an increased number of time increments. As a result, the computing effort can exceed that of the explicit time integration.

2.3.3 Gradient based optimization

For the determination of the material parameters $\boldsymbol{p}$, the method of least squares is a typical procedure. The material model calculates the stress in dependency of the material parameters $\boldsymbol{p}$. For optimization, the local minimum of the least square sum between calculated von Mises stress σ_{eq} and experimental stress σ_{exp} (from uniaxial tensile tests) has to be determined:

$$R^{\mathrm{sq}}(\boldsymbol{p}) = \frac{1}{2}\sum_{i=1}^{m}\left(\sigma_{\mathrm{eq},i}(\boldsymbol{p}) - \sigma_{\mathrm{exp},i}\right)^2 \tag{2.47}$$

with the number of data points m.

For the solution of this optimizing problem a gradient based algorithm is used. To find a local minimum, steps are performed that are proportional to the negative of the gradient at the current point:

$$\nabla R^{\mathrm{sq}} = \sum_{i=1}^{m}\left[\left(\sigma_{\mathrm{eq},i} - \sigma_{\mathrm{exp},i}\right)\frac{\partial \sigma_{\mathrm{eq},i}}{\partial \boldsymbol{p}}\right]. \tag{2.48}$$

Hence, the iteration rule is given by

$$\boldsymbol{p}^{n+1} = \boldsymbol{p}^{n} - \boldsymbol{\alpha}^{n}\nabla R^{\mathrm{sq},n} \tag{2.49}$$

with $\boldsymbol{\alpha}^n$ being the step size. In this work the Levenberg-Marquardt algorithm, also known as damped least-squares method is used [LY16, p. 213 ff.], [Mor77]. Thereby, the step size is a matrix calculated by

$$\boldsymbol{\alpha}^{n} = \left[\boldsymbol{H}^{n} + \lambda_{\mathrm{d}}^{n}\mathbf{I}\right]^{-1} \tag{2.50}$$

with the Hessian matrix

$$\boldsymbol{H} = \nabla\nabla R^{\mathrm{sq}} = \sum_{i=1}^{m}\left[\left(\frac{\partial \sigma_{\mathrm{eq},i}}{\partial \boldsymbol{p}}\right)^{T}\frac{\partial \sigma_{\mathrm{eq},i}}{\partial \boldsymbol{p}} + \left(\sigma_{\mathrm{eq},i} - \sigma_{\mathrm{exp},i}\right)\frac{\partial^2 \sigma_{\mathrm{eq},i}}{\partial \boldsymbol{p}\otimes\partial \boldsymbol{p}}\right], \tag{2.51}$$

the damping parameter λ_{d} and the identity matrix $\mathbf{I}$. The damping parameter λ_{d} enables the interpolation between the Gauss-Newton algorithm and the method of gradient descent, which makes it more robust than the Gauss-Newton algorithm. In this work, the gradient

and the Hessian are calculated numerically based on forward finite difference schemes with the first order finite difference approximation of the second order derivative:

$$\frac{\mathrm{d}R^{\mathrm{sq}}}{\mathrm{d}p_k} = \frac{R^{\mathrm{sq}}(p_k + \Delta p_k) - R^{\mathrm{sq}}(p_k)}{\Delta p_k} \tag{2.52}$$

and

$$\begin{aligned} \frac{\mathrm{d}^2 R^{\mathrm{sq}}}{\mathrm{d}p_k \mathrm{d}p_l} = \quad & \frac{1}{\Delta p_k \Delta p_l}[R^{\mathrm{sq}}(p_k + \Delta p_k, p_l + \Delta p_l) \\ & -R^{\mathrm{sq}}(p_k + \Delta p_k, p_l + \Delta p_l) - R^{\mathrm{sq}}(p_k, p_l)]. \end{aligned} \tag{2.53}$$

The projected Newton method from [Ber82] is used to keep the parameters within the given range.

Chapter 3

State of the art

The heat transfer from blank to tool generates a temperature gradient leading to thermal stresses. These thermal stresses and the mechanical stresses caused by the forming process superimpose each other. Despite the high strengths of the hot work tool steels, local plastic deformations can occur. Especially, tool radii and tool notches are threatened. The plastic deformations can cause microscopically small fatigue cracks (usually in the dimension of micro structural features such as the grain size or the length of martensite needles) at an early stage in tool life. Its growth determines the fatigue lifetime of the hot work tools. Therefore, it is of great interest for the tool design to have a simulation method with a precise description of the material behavior.

3.1 Material behavior

For a reliable assessment of hot work tools regarding their lifetime, the plasticity behavior in the complete operating temperature range must be well described. The steels are hardened and annealed in order to obtain a microstructure of the material resulting in the desired combination of strength, toughness and thermal stability. After quenching, the microstructure consists of martensitic laths, retained austenite, bainit and a small amount of primary carbides [ZDB07, BU17]. During annealing, the structure changes due to a diffusion type phase transformation to a structure with tempered martensit and bainite, retained austenite, primary carbides and newly formed martensit (from retained austenite decay) and secondary carbides [BU17, Sch12].

Figure 3.1 shows secondary carbides of a hot work tool steel measured by transmission electron microscopy. Typical carbides of the investigated steel (X38CrMoV5-3: chrome molybdenum vanadium alloyed steel) are for example vanadium-rich MC, chrome-rich $M_{23}C_6$ and molybdenum-rich M_6C and M_2C carbides [HLWZ06, Abe04, KPJ+15, LWL+15], where M stands for metallic element and C means carbon. The secondary carbides provide an increased carbide hardening in the material, which causes a heat resistance by preventing the motion of dislocations (Orowan mechanism) [BMN11, pp. 136–144].

During cyclic loading, the hardening of the material is significantly influenced by the Bauschinger effect. It leads to a lower flow stress after a reversal load compared to the previous flow stress. Cyclic plasticity experiments were carried out at temperatures of 20 to 600 °C for the material 55NiCrMoV7 [Ber99, ZBD08, ZDB07]. Ratchetting effects may appear due to occurring medium stresses. This means that no stationary plastic deformation occurs, however, the plastic deformation increases or decreases as well with increasing load cycles. This effect was observed for the material 55NiCrMoV7 at temperatures of 20 to 500 °C in [VBP06] and for a chromium nickel molybdenum hot working steel at temperatures of 250 to 550 °C under isothermal low cycle fatigue (LCF) and thermomechanical fatigue (TMF) in [JFG01].

At higher temperatures, such as those occurring in hot work tools,

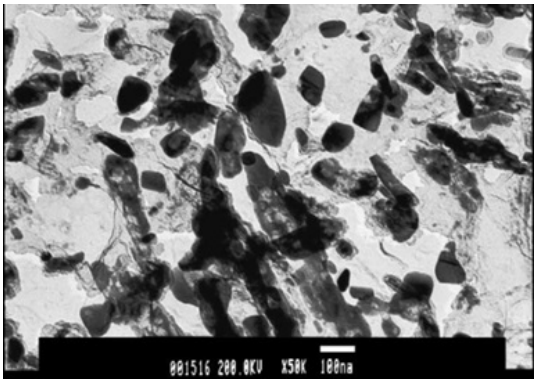

Fig. 3.1: Transmission electron microscopy measurement of a hot work tool steel [ZDB04]

thermally activated processes can take place. They can lead to a time-dependent material behavior such as stress relaxation, creep and the recovery of hardening. The time-dependent material behavior was determined experimentally in the temperature range of 20 to 600 °C for the material 55NiCrMoV7 [VBP06, ZBD08, ZDB07].

While temperatures for annealing of the tool steels usually lie in the range between 400 and 600 °C, the steels may experience even higher temperatures during hot forming, resulting in a further evolution of the mechanical material properties during service. An indication for this further evolution is a loss of strength that can be observed for different hot work tool steels. The softening can be explained by microstructural changes due to tempering as coarsening of strengthening particles (e.g. secondary carbides) while the volume fraction of the secondary carbides remains constant, as shown in [ZDB07]. This process is called Ostwald ripening and causes large particles to grow at the expense of small ones [LH14, pp. 965–968], which reduces the total number of particles, driven by the reduction of stored interfacial energy. Less carbides and the resulting larger distances eases dislocation motions, which causes a reduction in the strength. With a transmission electron microscope (TEM) the coarsening of carbides (especially $M_{23}C_6$) during aging tests at 550 and 650 °C for 9-chromium-tungsten-steels [Abe04] and at

700 °C for the high-temperature steel X40CrMoV5-1 [HLWZ06] was proved. Further tests were carried out at 600 and 650 °C for the hot work tool steel X38CrMoV5-3 [CSE+02] and for the hot work tool steels THG2000, QRO90 and MCG2006 at temperatures of 500 to 650 °C [MBGA09].

In [TKM01], a strain dependency of the carbide coarsening in a chromium-containing steel was determined. Furthermore, accelerated coarsening was observed in TMF tests. However, these tests were carried out at extremely high heating rates ($\dot{T} > 180$ K/s), whereby, additional effects could be superimposed since high tempreature gradients in the specimen can be expected. In [CSE+02], hardness curves for the steel X38CrMoV5-3 are shown, which indicate softening processes through Ostwald ripening. Similarly, the TMF tests indicate additional softening mechanisms, which have also been observed in [JFG01] for a chrome-nickel-molybdenum hot work tool steel. The materials have a longer lifetime under isothermal low cycle fatigue tests than under thermomechanical low cycle fatigue tests, although the maximum temperature does not exceed the isothermal temperature. This behavior can not be described by Ostwald ripening.

In [MBGA09], it is shown that the dislocation density of the tested hot work tool steels decreases further, if isothermal fatigue tests are carried out instead of aging tests at the same temperature and time. This is indicative of a mechanical softening of the steels (e.g. kinematic or isotropic softening). Moreover, a thermal based reduction of the dislocation density or a decrease in the lattice distortion as a result of thermally activated carbon diffusion may lead to a softening of the material. In addition, softening due to plasticity-induced changes in the dislocation structure can occur [GKS08].

In addition to time- and temperature-dependent plasticity, an understanding of damage mechanisms of the hot work tool steels is required to finally establish a reliable method for thermomechanical fatigue life prediction of hot work tools. In the case of thermomechanical fatigue stresses, the growth of microcracks plays a decisive role. The fatigue crack growth can also be accelerated by thermally activated processes such as creep and oxidation or corrosion and through softening of the material at relatively high operating temperatures.

For the hot work tool steel X38CrMoV5-1, the crack initiation was investigated in [GLS10] at isothermal (20, 300, 400 and 500 °C), and thermal fatigue tests from 100 to 650 °C. In the isothermal tests, only one major crack was detected, which grew until failure. During the thermal tests it was found that many small cracks with different lengths arose, and their frequency increased with increasing maximum temperature.

The crack growth was measured by [Eba10] for the hot work tool steel X37CrMoV5-1 with two different hardnesses at room temperature in the low-cycle fatigue area. A determined higher fatigue strength at the higher hardness was attributed to a delayed crack initiation, since the measured crack growth hardly differs. Additionally, thermal fatigue tests with maximum temperatures of 400, 600, 800 and 1000 °C were carried out and the crack length during the first 100 cycles was measured. At 400 °C no crack growth was observed, whereas, different growth rates were measured at the higher temperatures. In [MHKA14], crack growth measurements for the hot work tool steel X40CrMoV5-1 with two different hardnesses under thermal cycles from 25 to 750 °C can be found. The difference in the crack growth behavior can be attributed to the strongly different cyclic behavior of the two hardnesses (proportion of plastic deformation increases with lower strengths). In addition, crack growth measurements were carried out for the material X38CrMoV5 at 25 °C in the low-cycle fatigue area at different stress ratios [SMB+09].

3.2 Phenomenological models

In this section, advanced phenomenological models are presented, which are suitable for the description of cyclic plasticity of hot work tool steels and which can be implemented in finite-element programs for the analysis of hot working tools. Besides isotropic hardening, the models take also kinematic hardening and thus the Bauschinger effect (section 3.1) into account. They are typically based on the Chaboche model [Cha86, Cha89]. The time-dependent material behavior is thereby described by a power law in the flow rule (similar to the Norton creep law), which determines the evolution of the plastic strain tensor over time according to (2.19) and (2.20). The plastic multiplier is calculated by

$$\lambda = \langle \frac{\phi}{K} \rangle^n. \tag{3.1}$$

The Macaulay brackets indicate that the plastic deformation occurs only for positive overstresses ϕ. K and n are temperature-dependent material parameters.

In [Ber99], a plasticity model based on a Chaboche model is presented for the hot working tool steel 55NiCrMoV8. It is a model with a special focus to softening of the steel. The strength component through isotropic hardening R is calculated by a saturation function depending on the accumulated plastic strain $\bar{\varepsilon}^{\mathrm{p}}$:

$$R_{\bar{\varepsilon}^{\mathrm{p}}} = Q_1 \bar{\varepsilon}^{\mathrm{p}} + Q_2(q)(1 - e^{-b\bar{\varepsilon}^{\mathrm{p}}}) \tag{3.2}$$

with

$$Q_2(q) = Q_{\infty 2}(1 - e^{-2\mu q}), \tag{3.3}$$

where q represents the half of the current plastic strain range. Q_1, b, μ and $Q_{\infty 2}$ are material- and temperature-dependent parameters. Q_1 and $Q_{\infty 2}$ are negative, and thus describe softening. In this plasticity model, the Bauschinger effect is taken into account by two backstresses. Time- and temperature-dependent softening mechanisms, such as the coarsening of the carbides or the reduction of the dislocation density are not considered.

Another plasticity model can be found in [VBP06]. It is also an extension of the Chaboche model, which was developed for the

material 55NiCrMoV7. It contains two inelastic strain components and is therefore referred to as a non-unified plasticity model. The total plastic strain tensor thus consists of two parts:

$$\boldsymbol{\varepsilon}^{\mathrm{p}} = A_1 \boldsymbol{\varepsilon}_1^{\mathrm{p}} + A_2 \boldsymbol{\varepsilon}_2^{\mathrm{p}} \tag{3.4}$$

with the localization coefficients of the strain mechanisms A_1 and A_2. For each part, a separate flow rule exists. The splitting allows for example a good description of the material behavior for both high stresses (thermomechanical fatigue) and low stresses (creep) [CC89]. The softening and the Bauschinger effect are also taken into account via isotropic variables and back stresses respectively. With this model, a time-dependent softening can be described phenomenologically. However, this model does not consider softening effects as well.

Material models that describe softening of the material as a result of microstructural changes are now referred to as aging models. In [ZDB04] a time- and temperature-dependent aging model is introduced, which takes the aging of the material by a Johnson-Mehl-Avrami equation type into account:

$$\tau_v = 1 - e^{-(Dt)^m} = \frac{H_v - H_0}{H_\infty - H_0} \tag{3.5}$$

with

$$D = D_0 e^{-\frac{Q}{RT}}. \tag{3.6}$$

The tempering ratio τ_v is dependent on the diffusion coefficient D, the tempering exponent m and the tempering time t. The diffusion coefficient is, as usual, described by an Arrhenius approach, where D_0 is a temperature-independent prefactor, Q being the activation energy for the aging determining diffusion mechanism, and R is the universal gas constant. The hardness after quenching H_0 and the limit value (after long tempering) H_∞ must be known to determine the hardness after an arbitrary annealing step. The model was applied to the material 55NiCrMoV7. In [ZDB07], this model is tested at cyclic conditions as well, however, a cyclic softening could not be described. Thus, the softening model was embedded in a fully time-dependent plasticity model with isotropic softening and kinematic

hardening [ZBD08]. All temperature-dependent material parameters of the plasticity model are linearly dependent on the tempering ratio. This leads to a high number of material parameters, which must be determined on the basis of experimental data. Another application of the model is in the case of DM hot work tool steels, as shown in [ZXS+11].

The plasticity of the tool steels can be described with the phenomenological models presented so far, and in some cases the influence on the time- and temperature-dependent softening due to microstructural changes is considered phenomenologically. However, the models do not consider material damage by thermo-mechanical fatigue. An extension of the phenomenological models is achievable by introducing appropriate damage parameters. In [ØP00] a model for cold forming tools is shown, which is also an extension of the time-dependent Chaboche model with isotropic softening or hardening and kinematic hardening. In addition, it contains a damage parameter D, which can reach values from 0 (undamaged) to 1 (damaged):

$$\dot{D} = \frac{Y}{S}\dot{p}\alpha(p) \tag{3.7}$$

with

$$\alpha(p) = \begin{cases} 1 & \text{if } p \geqslant p_d \\ 0 & \text{if } p < p_d \end{cases}, \tag{3.8}$$

where Y is the strain energy release rate, p is the accumulated plastic strain, and S is a material parameter.

Another extended time-dependent Chaboche model with isotropic softening (including static recovery) and two kinematic hardening terms is presented in [SSW+07] for the hot work tool steel X36CrMoV5-1 for aluminum and copper extrusion and in [SSWR08] for the hot work tool steel X36CrMoV5-1 for aluminum extrusion. In the aging model, a time depending decrease of the viscosity coefficient K in the flow rule equation (3.1) is implemented:

$$K = K_0(T)\kappa \tag{3.9}$$

with

$$\dot{\kappa} = \frac{g}{K_0}\left(\frac{\langle K - K_\infty \rangle}{K_0 - K_\infty}\right)^z \tag{3.10}$$

and

$$\kappa(t=0)=1. \tag{3.11}$$

The quantities g, z, K_∞ and K_0 (initial viscosity coefficient) are temperature-dependent material parameters. The quantity κ is a phenomenological aging variable which can reach values between 0 (fully aged) and 1 (unaged). As K becomes smaller, the plastic strain rate increases, which on the one hand, build up lower overstresses and on the other hand, reduce already built-up overstresses more quickly.

The damage in this model is calculated by [SSW+07, SSWR08, SWHR08]:

$$\dot{D}=\left(\frac{\sigma_{\mathrm{eq}}}{A}\right)^m\left(\frac{\lambda}{\lambda_0}\right)^n\lambda_0. \tag{3.12}$$

The material parameters A and m describe the stress dependence, the material-specific exponent n considers the influence of dwell times in low-cycle fatigue tests, and λ_0 is a normalization constant. The model describes the experimental data quite well, but a large number of material parameters has to be determined. A further phenomenological evolution law for a damage parameter, which also takes the mean stress into account but includes even more material parameters than the previously presented models, was applied in [VBDP05] to the martensitic steel X38CrMoV5. Similarly, a good description of the data is achieved.

While material stresses have been determined by advanced plasticity models up to this point, in [BM05], an advanced statistical approach to lifetime assessment of the hot work tool steel X37CrMoV5-1 is shown. It is using the response surface methodology (RSM). This method is a mathematical and statistical technique for modeling mechanisms that depend on several variables [MR10]. In this case, there are three variables: the maximum temperature $x_1 = T_{\max}$, the minimum temperature $x_2 = T_{\min}$ and the ratio of equivalent stress to the temperature-dependent yield strength $x_3 = \sigma_{eq}/Y(T)$. The lifetime, i.e. the number of cycles to failure,

was modeled with a second order polynomial:

$$N = \beta_0 + \sum_{i=1}^{k} \beta_i x_i + \sum_{i=1}^{k} \beta_{ii} x_i^2 + \sum_{i<j} \sum \beta_{ij} x_i x_j + \varepsilon \tag{3.13}$$

The model parameters β_i and β_{ij} and the measurement error ε are determined based on experimental test results. For the measurement error ε, a normal distribution was determined. Even if decent predictions can be made with this model, these are only correct for a small predetermined range of application. Thus a generalization is not possible.

The models can basically describe the material behavior measured in the respective experiments. However, due to the increasing complexity, the phenomenological models contain an ever increasing number of material parameters, which must be determined on the basis of corresponding experiments. A generalization is complex and associated with uncertainties. By taking into account prior knowledge of the material and its mechanical relationships a reduction in the number of material parameters is possible. This leads to mechanism-based models presented in the following section.

3.3 Mechanism-based models

In this section, mechanism-based models whose functional dependencies relate to physical mechanisms are introduced. In this way a well-founded basis is provided leading to more reliable predictions and generalizations. The predominantly investigated mechanism in this work is particle coarsening, because Ostwald ripening is a major mechanism resulting in thermal softening of the hot work tool steels, see section 3.1. However, also mechanism-based model for TMF life prediction are presented here, since related softening-dependent material properties will be addressed in this work.

In [EL88], an aging model for the hot work tool steel X40CrMoV5-1 is presented, which is based on the Ostwald ripening, describing the coarsening of particles (for example secondary carbides in case of hot work tool steels). The modeling follows the

LSW theory, by Lifshitz, Slyozov and Wagner [SN14]:

$$\frac{\mathrm{d}r}{\mathrm{d}t} = \frac{1}{r^2} \frac{B_1}{\left(1 - B_2\sqrt{f}\right) T} e^{-\frac{Q}{RT}}. \tag{3.14}$$

The evolution of the average particle radius r is a thermally activated process with the activation energy Q. The material properties B_1 and B_2 are temperature-independent quantities, and f is the volume fraction of the particles.

In [Abe04], the mechanism of particle coarsening according to Ostwald for a martensitic steel is demonstrated. For this purpose, $M_{23}C_6$ carbides are measured and their coarsening is modeled by the solution of the LSW theory in the isothermal case:

$$r^3 - r_0^3 = kt = f(T, t). \tag{3.15}$$

It is the result of equation (3.14) after integration from an initial radius r_0 in the isothermal case. The particle radius r depends on the coarsening constant $k\,(T)$ and the time t. It is additionally shown, that the degradation of dislocation density due to coarsening of martensite laths accelerate creep.

In [TKM01], another coarsening term is introduced, which takes the strain rate into account, and thus leading to:

$$r^3 - r_0^3 = kt = f(T, t) + f(T, \varepsilon). \tag{3.16}$$

In [HLWZ06], the LSW theory for the steel X40CrMoV5-1 was validated by means of transmission electron microscopy measurements.

None of these mechanism-based aging models for the description of the softening is integrated into a cyclic plasticity model. For that reason, they cannot be used in finite element calculations to assess the fatigue life of the tools. However, they are generally suitable for integration into an advanced material model such as the Chaboche model.

Mechanism-based models to asses lifetime are based on the damage mechanisms associated with thermomechanical fatigue. The Sehitoglu model [NS89a, NS89b], which is a model available in commercial lifetime programs, considers damage fractions due to fatigue (fat), oxidation (ox), and creep damage (creep). A linear damage

accumulation is assumed, so that the number of cycles to failure can be calculated by

$$\frac{1}{N_\mathrm{f}} = \frac{1}{N_\mathrm{f}^\mathrm{fat}} + \frac{1}{N_\mathrm{f}^\mathrm{ox}} + \frac{1}{N_\mathrm{f}^\mathrm{creep}} \tag{3.17}$$

This method was applied in [EBHG+17] to hot work tool steels for a tube-manufacturing process. While oxidation damage is due to the mechanism of repeated growth and rupture of an oxide layer, the models of creep damage and fatigue damage are phenomenological. The calculation of fatigue damage is only based on the phenomenological Coffin-Manson-Basquin equation. In addition, a large number of material parameters are needed to describe all damage fractions whose determination is complex. Since the dominant mechanism in thermo-mechanical fatigue is crack growth, [SB97] presents a crack propagation-based model for the hot work tool steel X40CrMoV5-1. First, the crack initiation is determined by a Manson-Coffin relationship [Man54, Cof54] describing the plastic strain amplitude

$$\frac{\Delta\varepsilon^\mathrm{p}}{2} = \varepsilon_\mathrm{f}' \left(2N\right)^c \tag{3.18}$$

with the fatigue ductility coefficient ε_f', the number of cycles N and the fatigue ductility coefficient c. Then, the crack rate per cycle is modeled by Paris Law

$$\frac{\mathrm{d}a}{\mathrm{d}N} = C\Delta K^m, \tag{3.19}$$

where

$$\Delta K = Y\Delta\sigma\sqrt{\pi a} \tag{3.20}$$

with the material properties C and m, the cyclic stress intensity factor ΔK and the geometry factor Y. The cycles to fatigue failure can be calculated by integrating from a presumed initial crack length to a given length of the technical crack.

In [SMB+09], the Paris Law is applied to the hot work tool steel X38CrMoV5. However, the Paris Law is a model of linear-elastic fracture mechanics. Although it is also commonly used on metals (assuming a small plastic zone around the crack tip), the predictive power is limited in high stress areas, where significant plastic deformations occur [RBH06].

For low-cycle and thermomechanical fatigue, where plastic deformation is assumed, the description of the rate of crack growth via the cyclic crack tip opening displacement $\Delta CTOD$ has proved to be useful [Rie87, pp. 365 ff.]

$$\frac{\mathrm{d}a}{\mathrm{d}N} = \beta \Delta CTOD. \tag{3.21}$$

As a crack growth mechanism, this model is based on the idea that blunting of the crack tip and the following opening of the crack creates a fresh metallic surface at the crack tip. The surface is covered by oxygen from the environment and is rough, so that no re-welding takes place when closing the crack. $\Delta CTOD$ can be estimated by means of elastic-plastic fracture mechanics via the cyclic J-integral ΔJ [Wüt82]

$$\Delta CTOD = d_n \frac{\Delta J}{\sigma_{\mathrm{cy}}} \tag{3.22}$$

where d_n is a function depending on the hardening of the material according to the Ramberg-Osgood model. For short cracks, which are significantly smaller than characteristic dimensions of the component, an analytical solution for ΔJ exists, which interpolates between elastic and fully plastic solutions [KGS81]:

$$\Delta CTOD = d_{n'} \frac{Z_D}{\sigma_{\mathrm{cy}}} a, \tag{3.23}$$

where Z_D is a damage parameter according to Heitmann.

With creep fracture mechanics, the influence of the time-dependent material behavior on the crack opening can be taken into account. This finally leads to the damage parameter D_{TMF} [SSS$^+$10]

$$\Delta CTOD = d_{n'} D_{\mathrm{TMF}} a. \tag{3.24}$$

The crack growth law, see equation (3.21), can now be integrated with the relationships for $\Delta CTOD$ for time-dependent elastic-plastic material behavior from an initial crack length a_0 (typically associated with a characteristic length of the microstructure) up to a defined

crack length of the technical crack a_f. This results in the number of cycles up to the technical crack

$$N_\mathrm{f} = \frac{ln\left(\frac{a_\mathrm{f}}{a_0}\right)}{\beta d_{n'} D_\mathrm{TMF}}. \tag{3.25}$$

By introducing the parameters A and B, which are determined from experimental data, the formula can be generalized with

$$N_\mathrm{f} = \frac{A}{\left(d_{n'} D_\mathrm{TMF}\right)^B} \tag{3.26}$$

and thus, is more widely applicable [SR10, SSS+10]. The D_TMF model is of special interest for this work because it contains explicitely the mechanical material properties of the considered material. Changing material properties due to softening, thus, directly have an effect on the fatigue life.

Chapter 4

Experimental

This chapter describes the hot work tool steel considered in this work, the performed material tests and the measured test results. In particular, these are hardness and tensile tests after time and temperature-dependent softening.

4.1 Material

To sustain the high loads, the hot working tools are typically made of heat-treated martensitic hot work tool steels. In this work, the hot work tool steel 1.2367 (X38CrMoV5-3) is investigated. The chemical composition determined by melt analysis is summarized in table 4.1. The hardened and annealed material with a hardness of 54 HRC defines the initial as received state. In the following, the material in the initial state is denoted as HT0 (heat treatment 0).

C	Si	Mn	P	S	Cr	Mo	V
0.36	0.39	0.43	0.019	0.0008	4.99	2.85	0.53

Table 4.1: Chemical composition of the investigated material in %

4.2 Tempering

To investigate time- and temperature-dependent softening, the HT0 material was tempered for different tempering times and at different tempering temperatures in a heat-treatment furnace. The temperature range was between 450 °C and 650 °C. The longest tempering time was 14000 min (= 9 d 17 h 20 min). In particular, tempering at 600 °C for 350 min will be referred as HT1 (heat treatment 1) and tempering at 650 °C for 1000 min as HT2 (heat treatment 2).

Besides isothermal tempering, a non-isothermal temperature history is applied, where in the first 15 min the furnace was heated from 600 °C to 650 °C with constant heating rate (part 1). Then, the temperature was held constant until minute 150 (part 2), followed by cooling of the furnace to 600 °C with constant cooling rate until minute 350 (part 3). Finally, the temperature was held constant at 600 °C (part 4).

4.3 Mechanical testing

Mechanical material tests were performed on untempered and tempered specimen to determine the mechanical material properties and their evolution during softening of the material. On the one hand, the hardness according to the standard DIN EN ISO 6507 was measured on specimen with a diameter of 36 mm and a height of 10 mm.

For the generation of a correlation plot of hardness and 0.2 % offset yield strength, room temperature tensile tests according to the standard DIN EN ISO 6892 are performed on the other hand. The tensile specimens were produced according to DIN EN ISO 50125 with the geometry DIN 50125-A10x50. Seven tensile tests are done with specimen S1 to S6 being tempered according to the tempering time and temperature compiled in table 4.2 and specimen S7 being tempered up to 7174 min using the non-isothermal temperature history.

For the determination of cyclic mechanical material properties, stress-strain hysteresis loops were measured in cyclic tests with a dilatometer at the IFUM [BBB+17]. These tests were performed at room temperature, 200, 300, 400, 500 and 600 °C with HT0,

T in °C	time in min					
	100	187	350	1000	1600	2850
600		S6		S5	S4	
650	S3			S2		S1

Table 4.2: Isothermal tempering conditions of tensile specimens S1 to S6

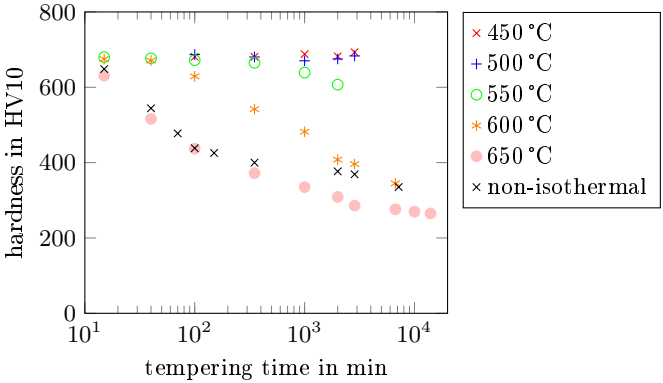

Fig. 4.1: Measured tempering hardness curves

HT1 and HT2 material. The German research foundation Deutsche Forschungsgemeinschaft (DFG) funded the tests as part of the joint research project 'Entwicklung einer Methodik zur Bewertung der Ermüdungslebensdauer von hochbelasteten Warmumformwerkzeugen auf Basis fortschrittlicher Werkstoffmodelle' (Bo 3616/5-1).

4.4 Results

In figure 4.1 the results of the isothermal and the non-isothermal tempering hardness curves are shown. A noticeable drop in hardness can be observed especially at the higher temperatures (600 and 650 °C).

For the material tempered at isothermal conditions (table 4.2), the measured room temperature 0.2 % offset yield strengths $R_{p0.2}$ in

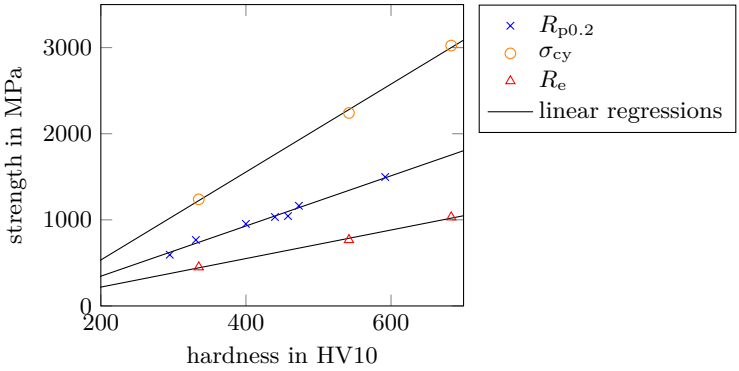

Fig. 4.2: Correlation plot of hardness and strength

dependency of the measured hardness are shown as symbols in the correlation plot in figure 4.2. A linear correlation is existent, which will be exploited in section 5.1 for the mathematical description of the mechanical properties.

The measured stress-strain hysteresis loops are shown in figures 4.3 to 4.5. The axis format has been retained in all three figures for a better comparison. A comparison of the figures shows a decrease in strength with increasing temperature as well as with increasing tempering.

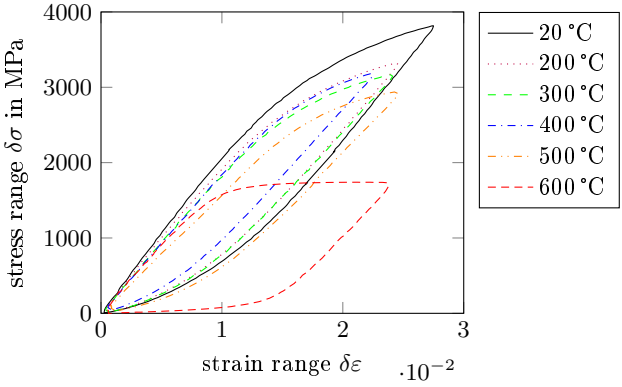

Fig. 4.3: Measured isothermal stress-strain hysteresis loops with HT0 material

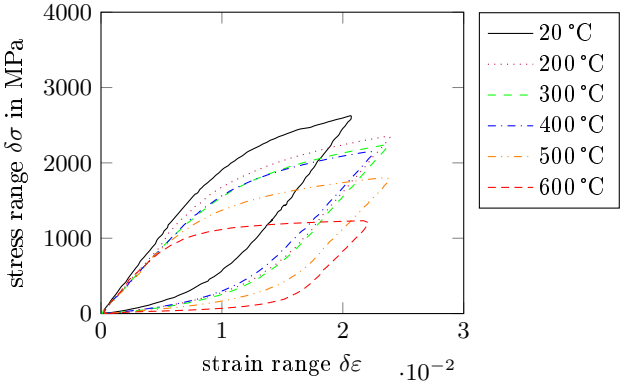

Fig. 4.4: Measured isothermal stress-strain hysteresis loops with HT1 material

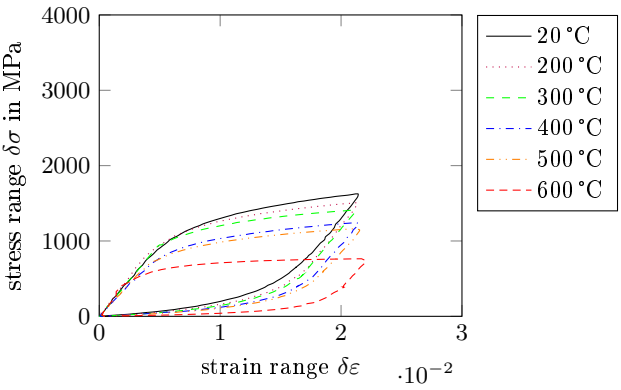

Fig. 4.5: Measured isothermal stress-strain hysteresis loops with HT2 material

Chapter 5

Material model

In this chapter, a kinetic model for the evolution of the mean size of secondary carbides based on Ostwald ripening is coupled with mechanical models to describe the thermal softening of the considered hot work tool steel. The stress-strain hysteresis loops measured in the cyclic mechanical tests are described with the Ramberg-Osgood model on the one hand, and with an incremental plasticity model including kinematic hardening on the other hand. While the Ramberg-Osgood model is directly involved in the mechanism-based D_{TMF} model for TMF life prediction (section 3.3), the incremental cyclic plasticity model is necessary in order that time- and temperature-dependent softening can be accounted for in finite element calculations. In the next section, the kinetic model for the description of the evolution of carbide's mean radius and its effect on the room temperature yield stress and hardness is developed, followed by the mechanical models in the subsequent sections.

5.1 Kinetic model

In the following, a kinetic model that describes coarsening of the secondary carbides, and a correlation of the size of the carbides with hardness is presented. The secondary carbides are not further specified (e.g. as $M_{26}C_6$ or M_6C). Instead, it is assumed that one carbide

species dominates softening, resulting in a mechanism-based engineering approach.

The yield strength σ_y of the material is described by the sum of the intrinsic strength $\sigma_{y,i}$ and the contribution of particle hardening $\Delta\sigma_p$ of the material:

$$\sigma_y = \sigma_{y,i} + \Delta\sigma_p. \tag{5.1}$$

Assuming particle hardening due to the Orowan mechanism, the dependency of particle hardening $\Delta\sigma_p$ on the mean particle radius r (assuming spherical particles) is, e.g. [RBH06, pp. 189–214]

$$\Delta\sigma_p = \frac{GbM\sqrt{f}}{\sqrt{2}}\frac{1}{r} = \frac{B_y}{r}, \tag{5.2}$$

where G is the shear modulus, b is the Burgers vector, f is the volume fraction of the particles and M is the Taylor factor relating the critical resolved shear stress of single crystals and to the yield stress of a polycrystal. Hence, the strength decreases with increasing mean radius of the particles. This relationship between hardness and particle size is demonstrated in [ZDB04] for a different hot work tool steel. Assuming that the volume fraction f of secondary carbides remain constant during coarsening (as shown in [ZDB04]), the process can be described by Ostwald ripening, where large particles grow at the expense of small particles, reducing the stored interfacial energy. Hence, the constants in equation (5.2) are combined to one material property related to particle hardening B_y, which has the same temperature dependency as the shear modulus, i.e. $B_y \propto G$.

Lifshitz, Slyozov and Wagner described in the LSW-Theory the evolution of the mean particle radius at constant volume fraction by [SN14, p. 521], [EL88]

$$\dot{r} = \frac{k}{r^2}. \tag{5.3}$$

k is the coarsening constant, defined as

$$k = \frac{4}{9}D\Omega c_\infty L, \tag{5.4}$$

where Ω is the atomic volume, c_∞ is the equilibrium concentration and D is the diffusion coefficient, given by the Arrhenius equation

$$D = D_0 e^{-\frac{Q}{RT}}. \tag{5.5}$$

T is the absolute temperature, R the universal gas constant, D_0 the temperature-independent pre-factor and Q the activation energy for diffusion. Since $L \propto 1/T$ holds for the capillary length L, the expression for the coarsening constant can be put in the engineering form

$$k = k_1 \frac{e^{-\frac{Q}{RT}}}{T} \tag{5.6}$$

with the material property k_1. Both, Q and k_1, are determined on the basis of the measured isothermal tempering hardness curves in the next section. To this end, the analytical solution to equation (5.3) for isothermal conditions, see equation (3.15), with the mean particle radius r_0 at the beginning of the coarsening process is used and the linear correlation of yield stress and hardness is exploited, see figure 4.2. Hence, from equations (5.1), (5.2) and (3.15), the expression for the yield stress

$$\sigma_\mathrm{y} = \sigma_{\mathrm{y,i}} + \frac{B_\mathrm{y}}{\sqrt[3]{kt + r_0^3}} \tag{5.7}$$

is obtained, resulting in the expression in terms of hardness

$$H = H_\mathrm{i} + \frac{B_H}{\sqrt[3]{kt + r_0^3}} \tag{5.8}$$

with the intrinsic hardness H_i and the material property $B_H \propto B_\mathrm{y} \propto G$.

5.1.1 Determination of the parameters

To describe the tempering hardness curves with the model, see equation (5.8), the intrinsic hardness H_i, the room temperature value of material property B_H, and the coarsening constant k for each tempering temperature are fitted such that a good description of the experimental data is obtained, see section 2.3.3. $r_0 = 0.1\,\mu\mathrm{m}$ is used

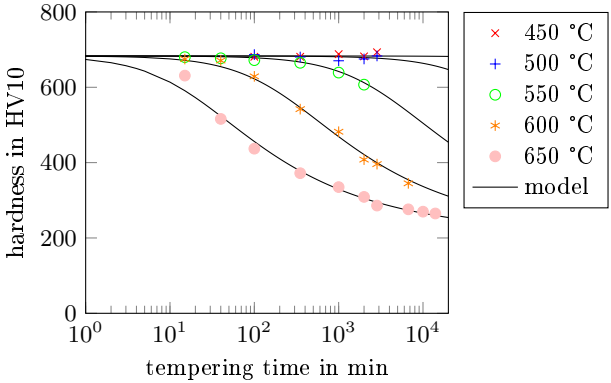

Fig. 5.1: Isothermal tempering hardness curves

as initial mean particle radius, which is in the order of comparable steels [HLWZ06, Abe04, LWL+15]. The black lines in figure 5.1 show a good model description using the following fitted parameters: The intrinsic hardness is 208.58 HV10 and the room temperature value of material property B_H is 47.42 HV10. The fitted values of the coarsening constant k are shown in figure 5.2 for each tempering temperature. The coarsening constant exponentially increases with temperature. For the mathematical description of the temperature-dependent coarsening constant k, the engineering expression given in equation (5.6) is applied. The activation energy Q and the material property k_1 are determined such that the temperature dependency of the coarsening constant is described well, resulting in $Q = 340.2\,\mathrm{mol/kJ}$ and $k_1 = 10^{-18}\,\mu\mathrm{m}^3/(\mathrm{minK})$. Figure 5.2 shows that the temperature dependency is well described by the model.

5.1.2 Validation

The determined material parameters are validated on the basis of the non-isothermal tempering hardness curve shown in figure 5.3. A temperature range from 600 to 650 °C, where the coarsening constant changes significantly, and different constant temperature rates $\dot{T}$ dur-

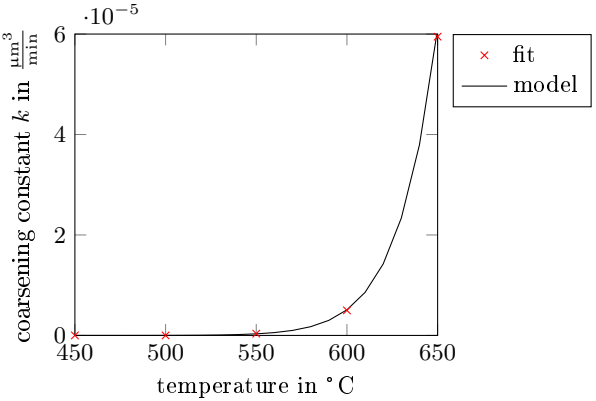

Fig. 5.2: Temperature dependency of coarsening constant k

ing heating and cooling are used, see section 4.2.

For the calculation of the non-isothermal tempering hardness curve, equation (3.15) is used for the isothermal parts of the temperature history. For the heating and cooling parts of the history, the solution of equation (5.3) for a linear temperature variation from an initial temperature T_i is used:

$$\frac{1}{3}\left(r^3 - r_0^3\right) = \frac{k_1}{\dot{T}}\left(\mathrm{Ei}\left(\frac{-Q}{T_i R}\right) - \mathrm{Ei}\left(\frac{-Q}{R\left(\dot{T}t + T_i\right)}\right)\right). \tag{5.9}$$

Figure 5.3 shows the evolution of the hardness predicted by the model for the non-isothermal loading history. The measured and the calculated non-isothermal tempering hardness curves are in good agreement.

5.2 Ramberg-Osgood model

The cyclic Ramberg-Osgood model provides an explicit relation between the stress $\delta\sigma$ and the strain $\delta\varepsilon$ with respect to the point of load reversal, see section 2.2.1. Since cyclic tests are performed, the

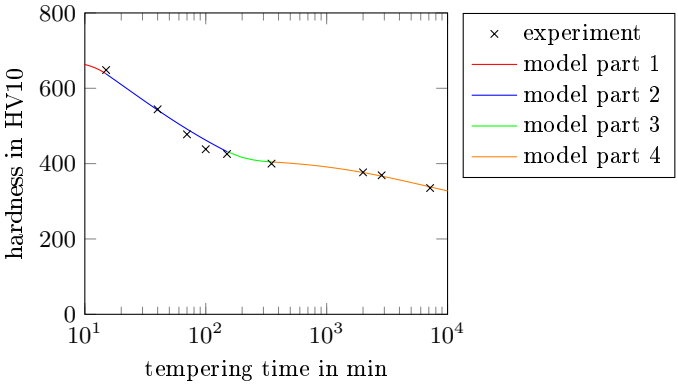

Fig. 5.3: Non-isothermal tempering hardness curve

uniaxial description of the cyclic Ramberg-Osgood model is used:

$$\delta\varepsilon = \frac{\delta\sigma}{E} + 0.002\frac{\delta\sigma}{\sigma_{\mathrm{cy}}}^{\frac{1}{n'}} \tag{5.10}$$

In the next section, the material properties E, n' and σ_{cy} are fitted to each cyclic mechanical test individually, before the mathematical description of the properties depending on temperature and on heat treatment is developed in section 5.2.2.

5.2.1 Determination of properties

Young's modulus E is determined by a linear regression of the hysteresis loading branch to the apparently linear part of the branch. In figure 5.4, the determined temperature-dependent values are plotted for the three different heat treatments (HT0, HT1 and HT2) as symbols. Additionally, values from a data sheet [vBE17] at 20, 500 and 600 °C are presented. The values determined in this work are close to the values of the data sheet. A dependency of Young's modulus on the heat treatment is not observed, confirming the assumption that the volume fractions of the carbides remain constant during tempering.

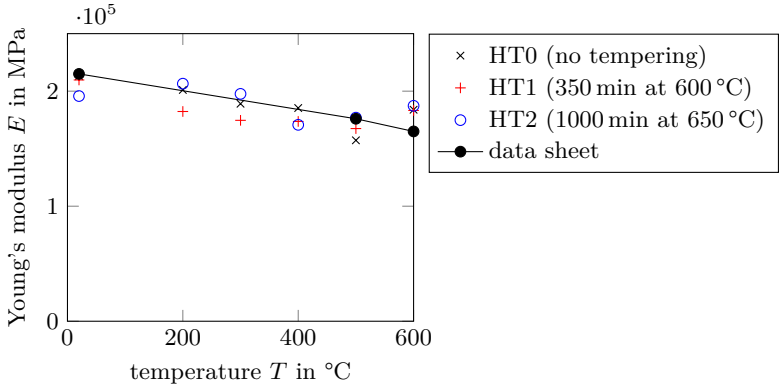

Fig. 5.4: Temperature dependency of Young's modulus E for different heat treatments

The cyclic yield stress σ_{cy} is directly obtained from the measured stress-strain hysteresis loops as the stress $\delta\sigma$ at plastic strain $\delta\varepsilon = 0.2\,\%$. In figure 5.5, the determined temperature-dependent values of σ_{cy} for HT0, HT1 and HT2 are shown as symbols. Due to coarsening of the carbides during tempering, the cyclic yield stress strongly depends on the heat treatment. While for HT1 and HT2 an expected decrease of cyclic yield stress with increasing temperature is observed, the cyclic yield stress shows a peak at 400 °C for the HT0 material. A possible explanation for the peak is the presence of dynamic strain aging at the considered temperatures and strain ranges [MZ14, pp. 231–235]. However, the typical serrated flow is not found in the stress-strain data. The determined cyclic yield stress indicates also a linear correlation, see figure 4.2.

The hardening exponent n' is finally determined by fitting to the stress-strain hysteresis loops using gradient based optimization, see section 2.3.3. The temperature-dependent values for HT0, HT1 and HT2 are plotted in figure 5.6 as symbols. For the lower temperatures, there is no unique dependency of the hardening exponent on the heat treatment and relatively low variation of the values. For the higher temperatures, however, the exponent is decreasing with an increasing temperature also depending on the heat treatment.

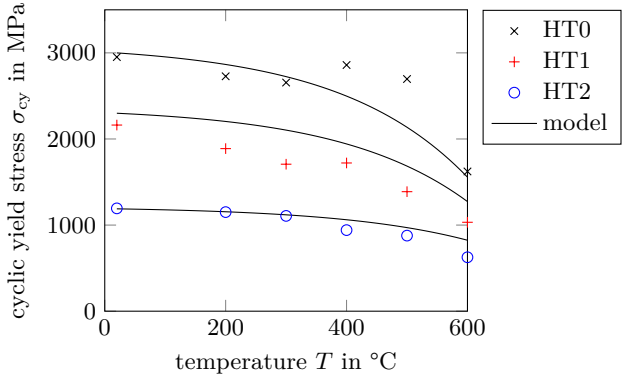

Fig. 5.5: Temperature dependency of cyclic yield stress σ_{cy} for different heat treatments

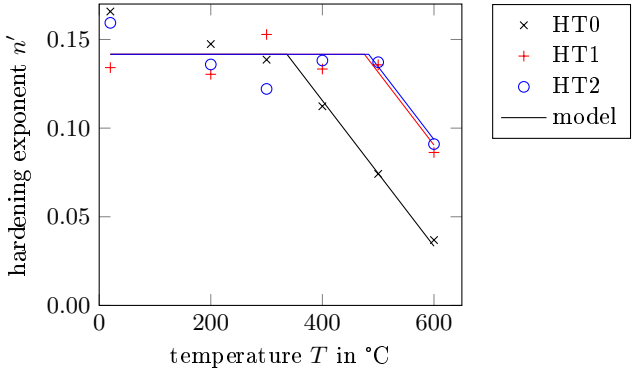

Fig. 5.6: Temperature dependency of hardening exponent n' for different heat treatments

With the material properties of the Ramberg-Osgood model that are fitted for each stress-strain hysteresis loop individually, a good description of each experimentally measured hysteresis loop is possible (figures 5.7 to 5.12).

5.2.2 Mathematical description of properties

For Young's modulus E, only a dependency on temperature is considered. A quadratic function is used to describe the E values of the data sheet (figure 5.4). Assuming a constant Poisson's ratio, $G \propto E$ is assumed for the shear modulus.

The dependency of the cyclic yield stress on the heat treatment is described in analogy to the dependency of the yield stress in equation (5.2), resulting in

$$\sigma_{\mathrm{cy}} = \sigma_{\mathrm{cy,i}} + \frac{B_{\mathrm{cy}}}{r}. \tag{5.11}$$

From the linear correlations of cyclic yield stress, yield stress and hardness, the room temperature value of the material property B_{cy} can directly be obtained from the already determined room temperature value of B_H, namely $B_{\mathrm{cy}} = 211,6\,\mathrm{MPa}$. The temperature dependency of B_{cy} is given by $B_{\mathrm{cy}} \propto G$. Temperature dependency of the intrinsic cyclic yield strength $\sigma_{\mathrm{cy,i}}$ is described with a mechanism-based approach as follows:

The resistance against plastic yielding (i.e. against dislocation glide) is decomposed in an athermal and thermal part [MZ14, pp. 207–217]. The athermal part is influenced by long-range internal stress fields acting over higher number of atomic distances. Like it is the case for particle hardening with its long-range internal stress fields, the temperature dependency of the athermal part corresponds to the temperature dependency of G. Hence, an athermal part of the cyclic yield stress $\sigma_{\mathrm{cy,i}}^{\mathrm{atherm}}$ is defined with $\sigma_{\mathrm{cy,i}}^{\mathrm{atherm}} \propto G$. The thermal part $\sigma_{\mathrm{cy,i}}^{\mathrm{therm}}$, however, is influenced by short-range internal stress fields and thermal fluctuations that support dislocations in overcoming barriers. It can be described by [MZ14, p. 213]:

$$\sigma_{\mathrm{cy,i}}^{\mathrm{therm}} = \sigma_{\mathrm{cy},0}\left[1 - \left(\frac{T}{T_0}\right)^{n_{\mathrm{cy}}}\right]^{m_{\mathrm{cy}}}, \tag{5.12}$$

where the material properties $\sigma_{\mathrm{cy},0}$, m_{cy} and n_{cy} do not depend on temperature. At temperature T_0 only thermal energy is required to overcome barriers. In general, it depends on strain rate, however it is assumed constant in this work since the same strain rate is used in the mechanical tests. According to data sheets of the hot work tool

steel, the strength strongly reduces at 700 °C [DES18]. Therefore, $T_0 = 700\,°\mathrm{C}$ is assumed.

Using the thermal and athermal part to the cyclic yield stress, one obtains the mechanism-based approach for the temperature dependency

$$\sigma_{\mathrm{cy}} = \sigma_{\mathrm{cy,i}}^{\mathrm{atherm}} + \sigma_{\mathrm{cy},0}\left[1 - \left(\frac{T}{T_0}\right)^{n_{\mathrm{cy}}}\right]^{m_{\mathrm{cy}}} + \frac{B_{\mathrm{cy}}}{r}. \tag{5.13}$$

The proportionality constants in $\sigma_{\mathrm{cy,i}}^{\mathrm{atherm}} \propto G$ and $B_{\mathrm{cy}} \propto G$ as well as the material properties $\sigma_{\mathrm{cy},0}$, n_{cy} and m_{cy} are determined on the basis of the measured cyclic yield stresses. The values for the yield stresses at 400 and 500 °C are not taken into account since the model cannot describe the observed peak. The following values are obtained: the proportionality constants are $3.75 \cdot 10^{-4}$ and $9.84 \cdot 10^{-4}\,\mu\mathrm{m}$ and $\sigma_{\mathrm{cy},0} = 629\,\mathrm{MPa}$, $m_{\mathrm{cy}} = 4$ and $n_{\mathrm{cy}} = 5.76$. The lines in figure 5.5 show the model description that is in good agreement with the considered measured values.

A purely phenomenological description of the dependency of the hardening exponent n' on temperature T and mean particle radius r on the basis of the measured exponents

$$n' = \begin{cases} n'_0 & \text{if } T < T_{\mathrm{start}}(r) \\ mT + c & \text{if } T > T_{\mathrm{start}}(r) \end{cases} \tag{5.14}$$

with

$$T_{\mathrm{start}}(r) = (T_{\mathrm{max}} - T_{\mathrm{min}})(1 - e^{-d(r-r_0)}) + T_{\mathrm{min}} \tag{5.15}$$

is proposed. n'_0, m, c, T_{min}, T_{max} and d are temperature-independent parameters. T_{min} and T_{max} indicate the lowest and the highest temperature at which the reduction of the parameter n' begins. In figure 5.6, the model description obtained with the fitted parameters and the measured values for n' for the different temperatures and heat treatments are plotted.

5.2.3 Stress-strain hysteresis loops

In figures 5.7 to 5.12, the stress-strain hysteresis loops computed with the mathematically described material properties (gray dashdotted

lines) are compared with the measured stress-strain hysteresis loops (solid lines) and the loops computed using the material properties determined individually for each test (black dashed lines). The same scale is used in all figures to visualize the temperature dependency of the material behavior. A good overall description of the stress-strain hysteresis loops for all temperatures depending on the time- and temperature-dependent softening during heat treatment is obtained. The discrepancy at 400 and 500 °C for HT0 material occurs since these temperatures are not considered in the mathematical description of the material properties.

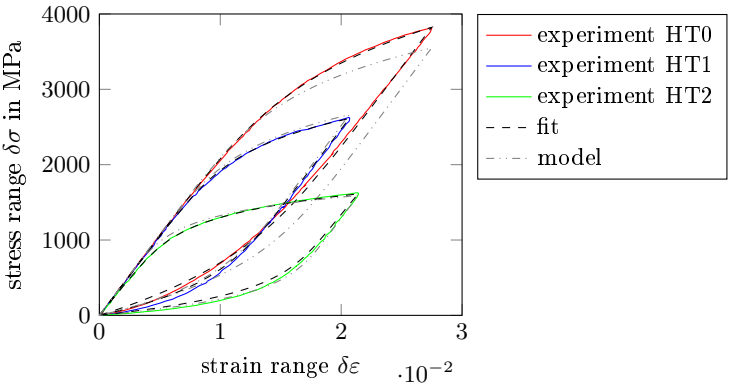

Fig. 5.7: Measured and calculated stress-strain hysteresis loops at 20 °C for different heat treatments; for the calculation, the individually fitted material properties and the mathematically described material properties are used

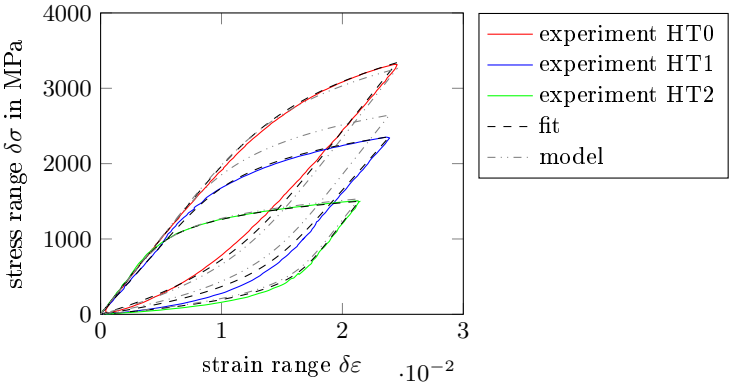

Fig. 5.8: Measured and calculated stress-strain hysteresis loops at 200 °C for different heat treatments; for the calculation, the individually fitted material properties and the mathematically described material properties are used

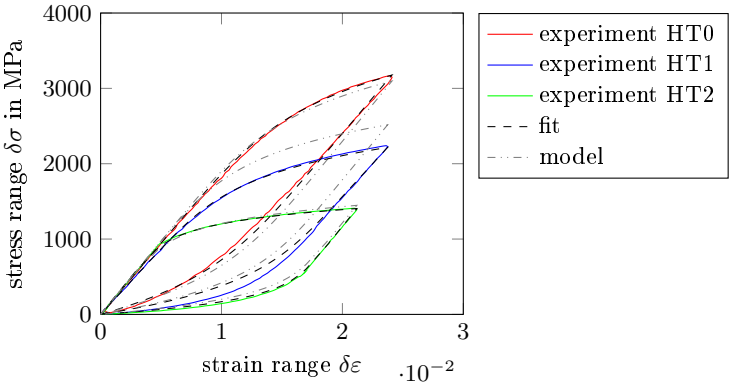

Fig. 5.9: Measured and calculated stress-strain hysteresis loops at 300 °C for different heat treatments; for the calculation, the individually fitted material properties and the mathematically described material properties are used

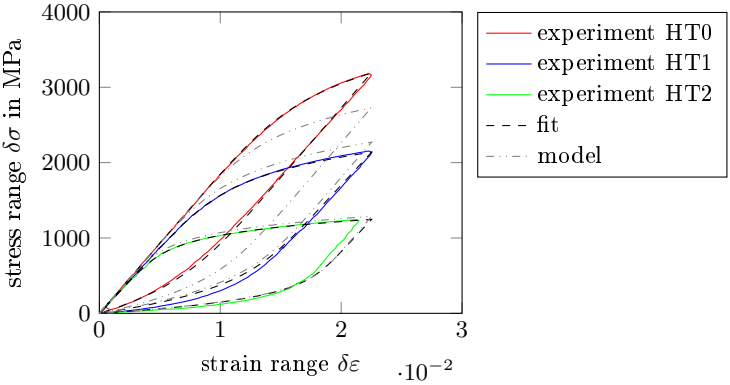

Fig. 5.10: Measured and calculated stress-strain hysteresis loops at 400 °C for different heat treatments; for the calculation, the individually fitted material properties and the mathematically described material properties are used

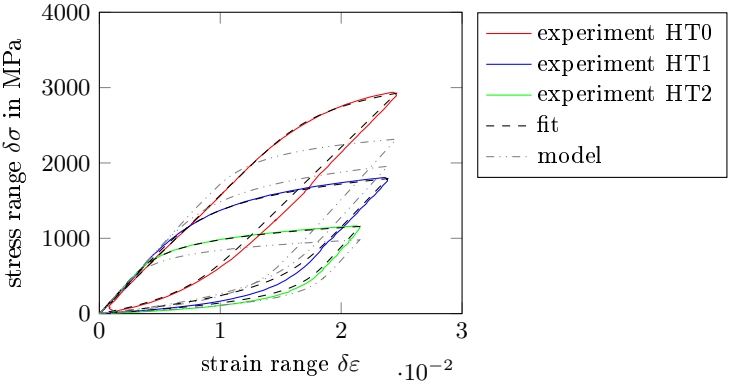

Fig. 5.11: Measured and calculated stress-strain hysteresis loops at 500 °C for different heat treatments; for the calculation, the individually fitted material properties and the mathematically described material properties are used

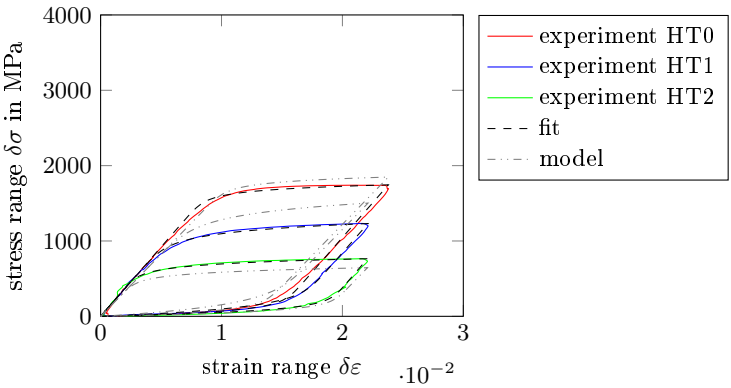

Fig. 5.12: Measured and calculated stress-strain hysteresis loops at 600 °C for different heat treatments; for the calculation, the individually fitted material properties and the mathematically described material properties are used

5.3 Incremental cyclic plasticity model

In this section, the stress-strain hysteresis loops measured in the cyclic mechanical tests are described with an incremental plasticity model including kinematic hardening, see section 2.2.2. In the following, the uniaxial formulation of the cyclic plasticity model is presented, as it is used for the determination and mathematical description in the next sections. In the uniaxial formulation the elastic strain can be calculated by

$$\varepsilon^e = \frac{\sigma}{E}. \tag{5.16}$$

The yield criterion is defined as

$$\phi = |\sigma - \alpha| - R_e. \tag{5.17}$$

The evolution of the backstress is described by

$$\dot{\alpha} = C\dot{\varepsilon}^p - \gamma\dot{\bar{\varepsilon}}^p\alpha + \frac{1}{C}\frac{\partial C}{\partial T}\dot{T}\alpha \tag{5.18}$$

and the flow rule is

$$\dot{\varepsilon}^p = \dot{\bar{\varepsilon}}^p \frac{\partial \phi}{\partial \sigma} \tag{5.19}$$

with

$$\dot{\bar{\varepsilon}}^p = |\dot{\varepsilon}^p|. \tag{5.20}$$

5.3.1 Determination of properties

The material properties for the incremental plasticity model are again determined by gradient based optimization, see section 2.3.3. In this way, the obtained curves are fitted to the measured cyclic stress-strain loops (full parameter fit). The determined temperature-dependent values of Young's modulus E are plotted for the three different heat treatments (HT0, HT1 and HT2) in figure 5.13 as symbols. The determined room temperature values for the initial yield strength R_e of the HT0, HT1 and HT2 material show once more a linear correlation with hardness, see figure 4.2. The determined temperature-dependent values of R_e for HT0, HT1 and HT2 material are shown as symbols in figure 5.14. For the HT1 and HT2 material an expected decrease with increasing temperature due to carbide coarsening is observed. However, for the HT0 material the yield strength shows again the peak at 400 °C, see section 5.2.1.

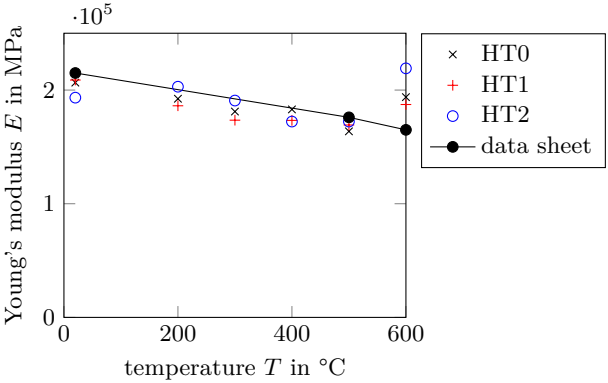

Fig. 5.13: Temperature dependency of Young's modulus E for different heat treatments

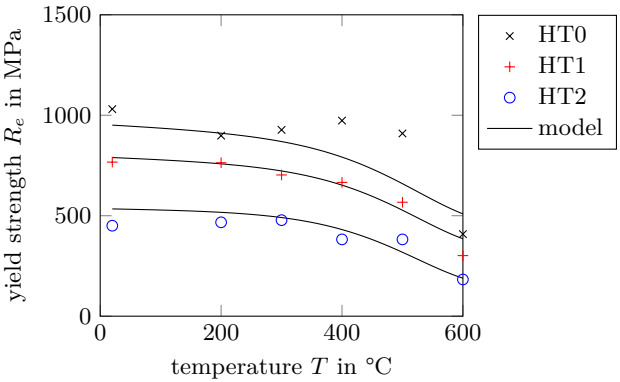

Fig. 5.14: Temperature dependency of yield strength R_e for different heat treatments

The kinematic hardening modulus C was found to be not temperature-dependent and its values are shown as symbols in figure 5.15. The determined temperature-dependent values of the kinematic hardening $C_\infty = C/\gamma$ are shown in figure 5.16. A good description of the measured stress-strain hysteresis loops is possible with the fitted material properties (figures 5.17 to 5.22).

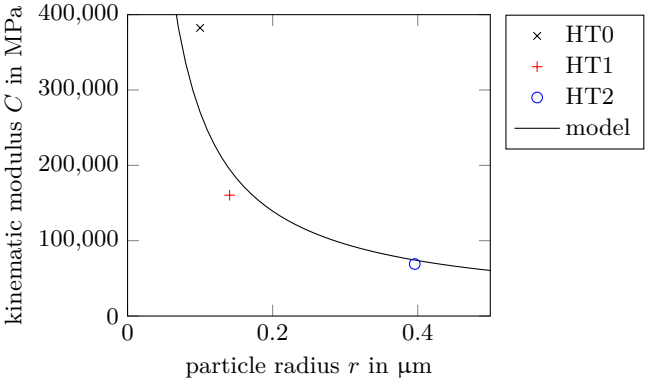

Fig. 5.15: Kinematic modulus C for different heat treatments

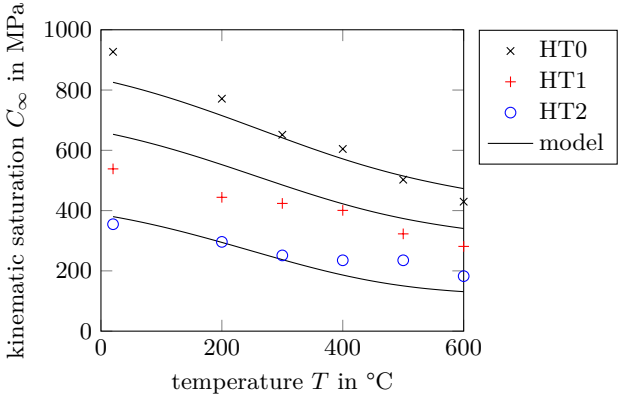

Fig. 5.16: Temperature dependency of Kinematic saturation value C_∞ for different heat treatments

5.3.2 Mathematical description of properties

For the description of the dependency of yield strength R_e on heat treatment, the linear correlation of yield strength and hardness at room temperature is employed, resulting in

$$R_e = R_{\mathrm{e,i}}^{\mathrm{atherm}} + R_{\mathrm{e},0}\left[1 - \left(\frac{T}{T_0}\right)^{n_\mathrm{e}}\right]^{m_\mathrm{e}} + \frac{B_\mathrm{e}}{r}. \tag{5.21}$$

The first two terms represent the intrinsic yield strength, which is, according to the mechanism-based approach derived in [JS18a], separated into an athermal part $R_{\mathrm{e,i}}^{\mathrm{atherm}} \propto G$ and a thermal part. $G \propto E$ is the temperature-dependent shear modulus (constant Poisson's ratio assumed). $R_{\mathrm{e},0}$, m_e and n_e are temperature-independent material properties. T_0 is the temperature, where only thermal energy is required to overcome barriers and it is set to $T_0 = 700$ °C, see section 5.2.2. The room temperature value of the material property B_e can again directly be obtained from the already determined room temperature value of B_H, namely $B_\mathrm{e} = 55,8$ MPa. The temperature dependency of B_e is given by $B_\mathrm{e} \propto G$.

The proportionality constants in $R_{\mathrm{e,i}}^{\mathrm{atherm}} \propto G$ and $B_\mathrm{e} \propto G$ as well as the material properties $R_{\mathrm{e},0}$, n_e and m_e are determined on the ba-

sis of the measured yield strength. The values for the yield strengths at 400 and 500 °C are not taken into account since the model cannot describe the observed peak. The following values are obtained: the proportionality constants are $2,99 \cdot 10^{-04}$ and $2.60 \cdot 10^{-07}$ µm, $R_{e,0} = 328.8\,\mathrm{MPa}$, $m_\mathrm{e} = 4$ and $n_\mathrm{e} = 7.5$. The lines in figure 5.14 show the model description that is in good agreement with the considered measured values. For the material property C, no temperature dependency was observed. Since it is also a property with the unit of the stress a description in analogy of equation (5.8) is used:

$$C = C_\mathrm{i} + \frac{B_\mathrm{c}}{r} \tag{5.22}$$

with an intrinsic property C_i and a material property related to particle hardening B_c, figure 5.15. Their obtained values are: $C_\mathrm{i} = 7964,7\,\mathrm{MPa}$ and $B_\mathrm{c} = 26255,4\,\mathrm{MPa/\mu m}$. The description for the material property C_∞ is based on equation (5.21) as it is also describing the strength

$$C_\infty = C_{\infty,\mathrm{i}}^{\mathrm{atherm}} + C_{\infty,0}\left[1 - \left(\frac{T}{T_0}\right)^{n_\infty}\right]^{m_\infty} + \frac{B_\infty}{r}. \tag{5.23}$$

The identical temperature dependencies are assumed and the following values are obtained for the proportionality constants: $8.7 \cdot 10^{-05}$ and $2.77 \cdot 10^{-04}$ µm. $C_{\infty,0} = 246.1\,\mathrm{MPa}$, $m_\infty = 4$ and $n_\infty = 2.73$ are determined. The description is in good agreement with the considered measured values, as shown in figure 5.16.

5.3.3 Stress-strain hysteresis loops

In figures 5.17 to 5.22 the measured stress-strain hysteresis loops at the temperatures from 20 to 600 °C are shown. At each temperature, a measured loop is plotted for each softening condition. Additionally, for each measured loop (solid lines) there is a loop, computed with the mathematically described material properties (gray dashdotted lines) and a loop computed using the material properties determined individually for each test (black dashed lines). For the visualization of the temperature dependency of the material behavior, the same scale is used in all figures. The measured and the calculated loops

are in good agreement at all temperatures depending on the time- and temperature-dependent softening during heat treatment. The discrepancy at 400 and 500 °C for HT0 material is also evident here and it occurs since these temperatures are not considered in the mathematical description of the material properties.

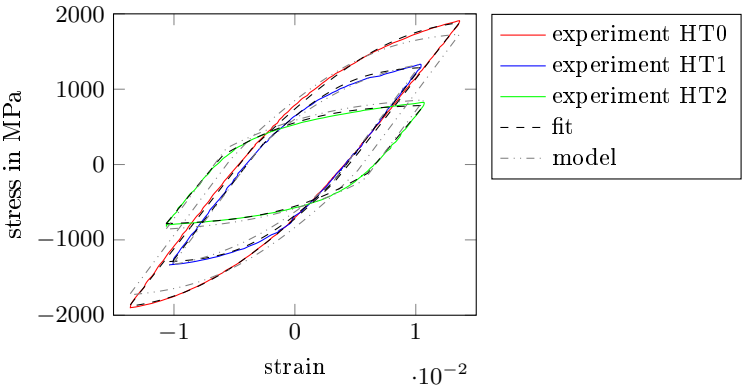

Fig. 5.17: Measured and calculated stress-strain hysteresis loops at 20 °C for different heat treatments; for the calculation, the individually fitted material properties and the mathematically described material properties are used

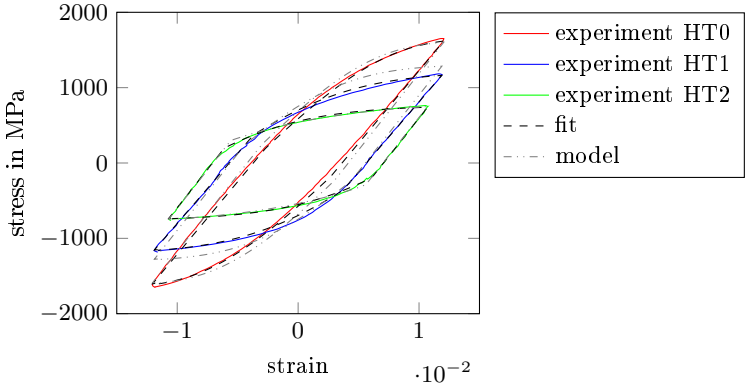

Fig. 5.18: Measured and calculated stress-strain hysteresis loops at 200 °C for different heat treatments; for the calculation, the individually fitted material properties and the mathematically described material properties are used

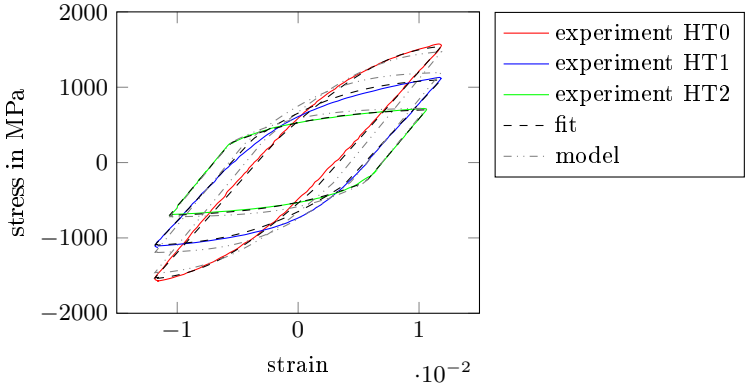

Fig. 5.19: Measured and calculated stress-strain hysteresis loops at 300 °C for different heat treatments; for the calculation, the individually fitted material properties and the mathematically described material properties are used

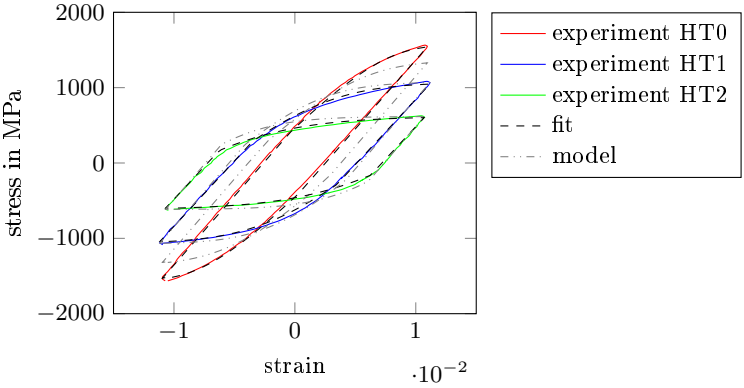

Fig. 5.20: Measured and calculated stress-strain hysteresis loops at 400 °C for different heat treatments; for the calculation, the individually fitted material properties and the mathematically described material properties are used

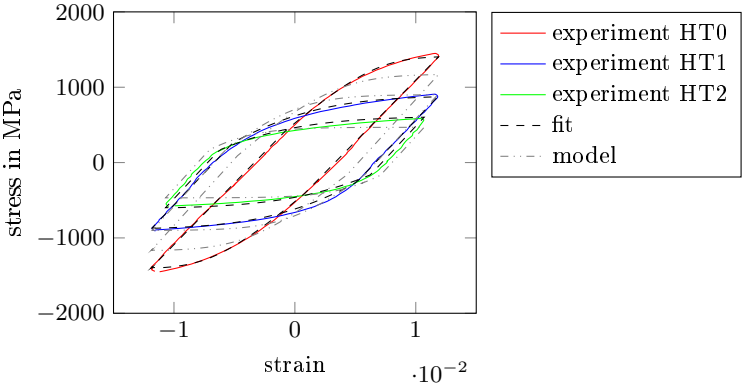

Fig. 5.21: Measured and calculated stress-strain hysteresis loops at 500 °C for different heat treatments; for the calculation, the individually fitted material properties and the mathematically described material properties are used

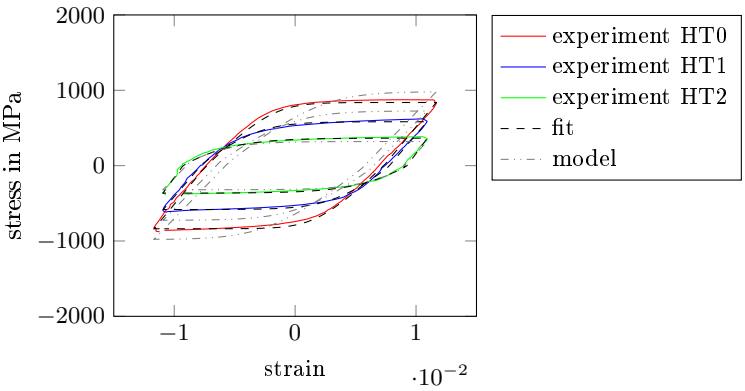

Fig. 5.22: Measured and calculated stress-strain hysteresis loops at 600 °C for different heat treatments; for the calculation, the individually fitted material properties and the mathematically described material properties are used

Chapter 6

Finite element implementation

The implementation of the described material model is performed with the finite element program ABAQUS. In the next sections the schematic structure of the algorithm and the used predictor-corrector method is described. Large deformations, non-linear plastic behavior and many contact conditions lead to a highly nonlinear overall problem for FEM simulations. Explicit time integration is suitable for such highly nonlinear problems. Therefore, hot working processes are often calculated with explicit solvers. Thus, the model is implemented via a subroutine (VUMAT) in ABAQUS/Explicit (implementation in cooperation with Simon Schilli).

The detailed investigation of small critical areas requires strong mesh refinements. However, the critical step size for the explicit calculations depends on the minimal element length l, see equation (2.44). Thus, strong mesh refinements lead to high computing power. Therefore, the material model is also implemented in ABAQUS/Standard using the subroutine UMAT.

6.1 Algorithm structure

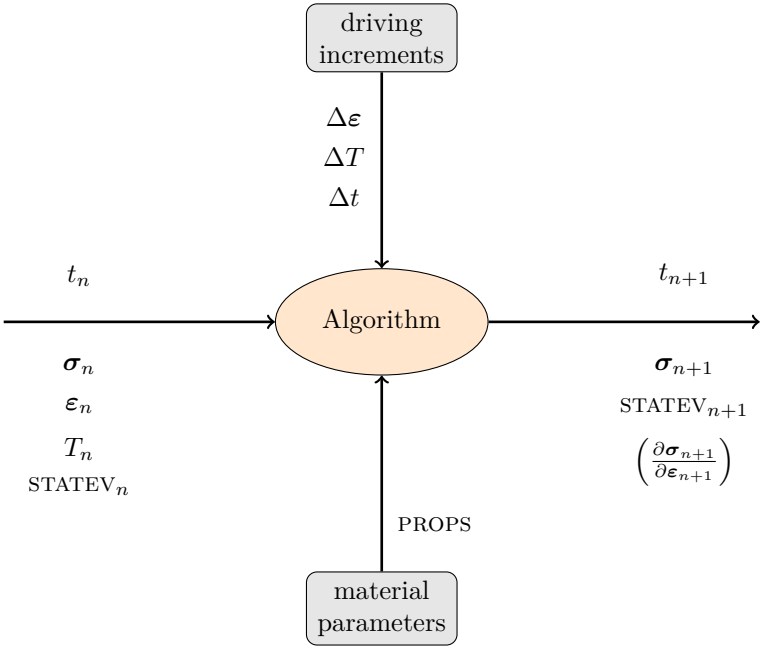

Fig. 6.1: Structure of algorithms

Figure 6.1 shows the input and output variables of the algorithm. It calculates the variables at time t_{n+1} out of the input variables at time t_n. ABAQUS provides the variables stress $\boldsymbol{\sigma}_n$, strain $\boldsymbol{\varepsilon}_n$ and temperature T_n at time t_n, as well as the driving increments of strain $\Delta\varepsilon$, temperature ΔT and time Δt. Further variables required for the calculation must be stored as internal variables (stored in an array STATEV). The material properties are provided to the algorithm in an array PROPS. The internal variables are integrated numerically implicit in the general form

$$x_{n+1} = x_n + \Delta x_{n+1} = x_n + \Delta t \dot{x}_{n+1}. \tag{6.1}$$

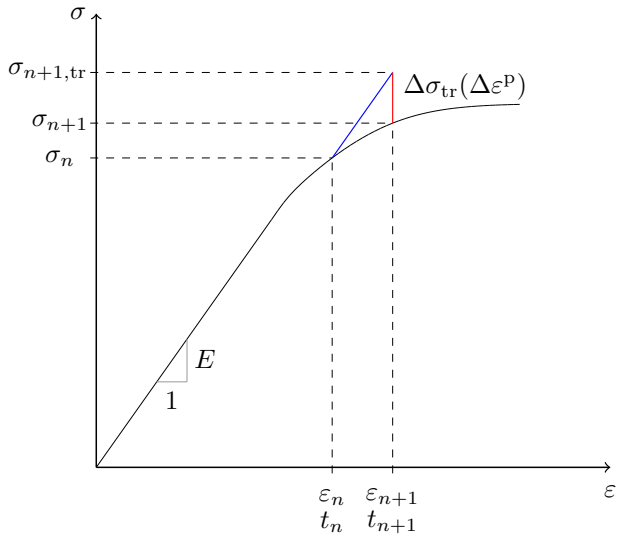

Fig. 6.2: Predictor-corrector-method using the example of a uniaxial tensile test [Sch18, p. 25]

The advantage of the implicit method is its unconditional stability. After the calculation, the algorithm passes the stress $\boldsymbol{\sigma}_{n+1}$, the internal variables STATEV_{n+1} and in the case of UMAT, the derivative $\partial\boldsymbol{\sigma}_{n+1}/\partial\boldsymbol{\varepsilon}_{n+1}$ (required for implicit time integration) to ABAQUS.

6.2 Predictor-corrector method

Both subroutines use a predictor-corrector method. This method is particularly suitable for material models in which elastic and plastic effects are connected in series. First, a purely elastic predictor step is made. Then it is checked whether the result is in the elastic range. If necessary, the result is optimized by a subsequent corrector step [Wri08, pp. 239–242]. In figure 6.2, the procedure of the predictor-corrector method using the example of a uniaxial tensile test is shown. First, for the determination of the stress at time t_{n+1}, the purely elastic trial stress $\sigma_{\text{tr},n+1}$ (predictor, blue) is calculated.

The slope of the straight line corresponds to the Young's modulus. If the yield criterion is greater than the specified tolerance, the stress is corrected by the plastic corrector (red), so that the yield criterion is within the tolerance. In figure 6.3, the schematic structure of the used predictor-corrector method is shown.

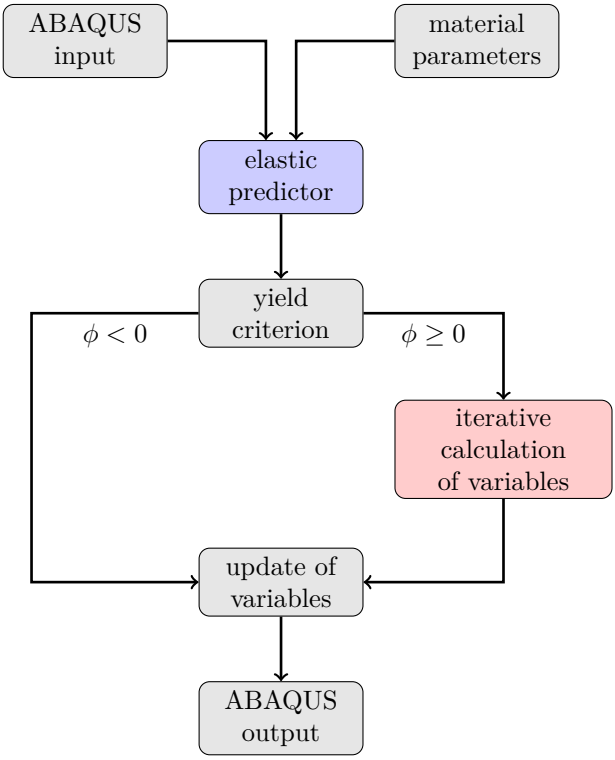

Fig. 6.3: Schematic structure of predictor-corrector-method

6.3 Integration algorithm

The variables are determined implicitly. The plastic strain $\boldsymbol{\varepsilon}^p$, backstress $\boldsymbol{\alpha}$, particle radius r and accumulated strain $\overline{\varepsilon}^p$ are combined in one vector

$$\boldsymbol{Y} = \left[\begin{array}{cccc} \boldsymbol{\varepsilon}^p & \boldsymbol{\alpha} & r & \overline{\varepsilon}^p \end{array} \right]^T. \tag{6.2}$$

The first three entrees of the vector $\boldsymbol{Y}$ at time t_{n+1} can be calculated by equation (6.1) together with the rates of $\boldsymbol{\varepsilon}^p$ (2.19), $\boldsymbol{\alpha}$ (2.18) and r (5.3) leading to

$$\bar{\boldsymbol{Y}}_{n+1} = \bar{\boldsymbol{Y}}_n + \Delta t \lambda_{n+1} \bar{\boldsymbol{D}}_{n+1} + \bar{\boldsymbol{M}}_{n+1}, \tag{6.3}$$

where $\bar{(\cdot)}$ cuts off the last entry of the vectors. The flow directions $\bar{\boldsymbol{D}}_{n+1}$ can be calculated by

$$\bar{\boldsymbol{D}}_{n+1} = \left[\begin{array}{ccc} \boldsymbol{N}_{n+1} & \frac{2}{3} C_{n+1} \boldsymbol{N}_{n+1} - \gamma_{n+1} \boldsymbol{\alpha}_{n+1} & 0 \end{array} \right]^T \tag{6.4}$$

and the static contributions $\bar{\boldsymbol{M}}_{n+1}$ (i.e. contributions independent on plastic deformations) by

$$\bar{\boldsymbol{M}}_{n+1} = \left[\begin{array}{c} 0 \\ \frac{\boldsymbol{\alpha}_{n+1}}{C_{n+1}} \frac{\partial C_{n+1}}{\partial r_{n+1}} \mathrm{d}r \\ \Delta t \frac{k_{n+1}}{r_{n+1}^2} \end{array} \right]. \tag{6.5}$$

The second entry of $\boldsymbol{M}_{n+1}$ must be taken into account, since C depends on particle radius, see equation (5.22). This is done in analogy to the temperature history effect when the parameter C is depending on temperature [Cha89]. However, the temperature history effect itself need not be taken into account, since no temperature dependency for C was observed. Transforming equation (6.3) into a residual one obtains

$$\bar{\boldsymbol{R}}(\boldsymbol{Y}_{n+1}) = \bar{\boldsymbol{Y}}_{n+1} + \bar{\boldsymbol{Y}}_n + \Delta t \lambda_{n+1} \bar{\boldsymbol{D}}_{n+1} + \bar{\boldsymbol{M}}_{n+1}. \tag{6.6}$$

For the elastic predictor step λ_{n+1} is set to zero, whereas, for plastic behavior it is calculated by

$$\lambda_{n+1} = \frac{\overline{\varepsilon}^p_{n+1} - \overline{\varepsilon}^p_n}{\Delta t}. \tag{6.7}$$

Here, it is helpful to insert the side condition $\phi = 0$ in the residual leading to

$$\boldsymbol{R}\left(\bar{\boldsymbol{Y}}_{n+1}, \phi_{n+1}\right) = \begin{bmatrix} -\bar{\boldsymbol{Y}}_{n+1} + \bar{\boldsymbol{Y}}_n + \Delta t \lambda_{n+1} \bar{\boldsymbol{D}}_{n+1} + \bar{\boldsymbol{M}}_{n+1} \\ \phi_{n+1} \end{bmatrix}. \tag{6.8}$$

This equation can be solved with the Newton's method, see section 2.3:

$$\boldsymbol{Y}^{i+1}_{n+1} = \boldsymbol{Y}^{i}_{n+1} - (\boldsymbol{J}(\boldsymbol{Y}^{i}_{n+1}))^{-1} \cdot \boldsymbol{R}(\boldsymbol{Y}^{i}_{n+1}) = \boldsymbol{Y}^{i}_{n+1} + \delta \boldsymbol{Y}^{i}. \tag{6.9}$$

$\delta \boldsymbol{Y}^i$ is determined by solving

$$\boldsymbol{J}(\boldsymbol{Y}^{i}_{n+1}) \delta \boldsymbol{Y}^{i} = -\boldsymbol{R}(\boldsymbol{Y}^{i}_{n+1}) \tag{6.10}$$

using linear solvers. Calculating the Jacobian matrix one obtains

$$\frac{\partial \bar{\boldsymbol{R}}}{\partial \boldsymbol{Y}_{n+1}} = -\boldsymbol{I}\boldsymbol{I} + \Delta t \bar{\boldsymbol{D}}_{n+1} \otimes \frac{\partial \lambda_{n+1}}{\partial \boldsymbol{Y}_{n+1}} + \Delta t \lambda_{n+1} \frac{\partial \bar{\boldsymbol{D}}_{n+1}}{\partial \boldsymbol{Y}_{n+1}} + \frac{\partial \bar{\boldsymbol{M}}_{n+1}}{\partial \boldsymbol{Y}_{n+1}} \tag{6.11}$$

and

$$\frac{\partial R_\phi}{\partial \boldsymbol{Y}_{n+1}} = \begin{bmatrix} \frac{\partial R_\phi}{\partial \boldsymbol{\varepsilon}^{\mathrm{p}}} & \frac{\partial R_\phi}{\partial \boldsymbol{\alpha}} & \frac{\partial R_\phi}{\partial r} & \frac{\partial \boldsymbol{R}_\phi}{\partial \phi} \end{bmatrix}. \tag{6.12}$$

The analytical derivatives are implemented in the subroutines and documented in Appendix. The Newton's method is carried out until the largest value among the residuals $\max(R_i)$ is less than a specified tolerance. Once $\boldsymbol{Y}_{n+1}$ and thus $\boldsymbol{\varepsilon}^{\mathrm{e}} = \boldsymbol{\varepsilon} - \boldsymbol{\varepsilon}^{\mathrm{p}}$ is determined, the stress at time t_{n+1} can be calculated with equation (2.4).

In implicit time integration (UMAT), the weak form of the FEM balance law of linear momentum, see equation (2.29), must be solved in each time increment. Therefore, the derivative of the stress in respect to strain (also called consistent tangent) must be calculated:

$$\frac{\partial \boldsymbol{\sigma}_{n+1}}{\partial \boldsymbol{\varepsilon}_{n+1}} = \frac{\partial \boldsymbol{\sigma}_{n+1}}{\partial \boldsymbol{\varepsilon}^{p}_{n+1}} \cdot \frac{\partial \boldsymbol{\varepsilon}^{p}_{n+1}}{\partial \boldsymbol{\varepsilon}_{n+1}}. \tag{6.13}$$

Together with equation (2.4) and (2.7) the first factor results in

$$\frac{\partial \boldsymbol{\sigma}_{n+1}}{\partial \boldsymbol{\varepsilon}^{p}_{n+1}} = -\mathbb{C}^{e}_{n+1}. \tag{6.14}$$

For the second factor it is helpful to build the total differential of $\boldsymbol{R}\left(\boldsymbol{Y}\left(\boldsymbol{\varepsilon}\right),\boldsymbol{\varepsilon}\right)$ in respect to total strain

$$\frac{\mathrm{d}\boldsymbol{R}}{\mathrm{d}\boldsymbol{\varepsilon}_{n+1}} = \frac{\partial \boldsymbol{R}}{\partial \boldsymbol{\varepsilon}_{n+1}} + \frac{\partial \boldsymbol{R}}{\partial \boldsymbol{Y}_{n+1}} \cdot \frac{\partial \boldsymbol{Y}_{n+1}}{\partial \boldsymbol{\varepsilon}_{n+1}} = \boldsymbol{0} \tag{6.15}$$

leading to

$$\frac{\partial \boldsymbol{Y}_{n+1}}{\partial \boldsymbol{\varepsilon}_{n+1}} = -\left[\frac{\partial \boldsymbol{R}}{\partial \boldsymbol{Y}_{n+1}}\right]^{-1} \cdot \frac{\partial \boldsymbol{R}}{\partial \boldsymbol{\varepsilon}_{n+1}}. \tag{6.16}$$

Since the first entries of $\boldsymbol{Y}$ correspond with the plastic strain, the second factor of the consistent tangent can now be calculated. $\partial \boldsymbol{R}/\partial \boldsymbol{\varepsilon}_{n+1}$ results in the identity tensor (at the first entries) and $\partial \boldsymbol{R}/\partial \boldsymbol{Y}_{n+1}$ is the Jacobian matrix, see equation (6.11). Now all variables are available for the ABAQUS input.

6.4 Validation

Before the model was implemented in the user subroutines UMAT and VUMAT, its uniaxial formulation was implemented in the programming language Python. For the validation of the correct implementation, the results of the ABAQUS subroutines are compared with the Python implementation. For the ABAQUS simulations, a model is needed, in which no model dependent influences exist. Therefore a simple one-element-model is created in ABAQUS. On this model, a uniaxial cyclic load is used for investigating the cyclic behavior. During monotonic tensile loading, the resulting stress response is equivalent to the von Mises stress.

Since the investigated material model shows only a microstructural evolution at high temperatures, the model at low temperatures can additionally validated by analytical calculations. Analytical calculations can also be made in case of thermal softening without additional mechanical load according to equation (3.15).

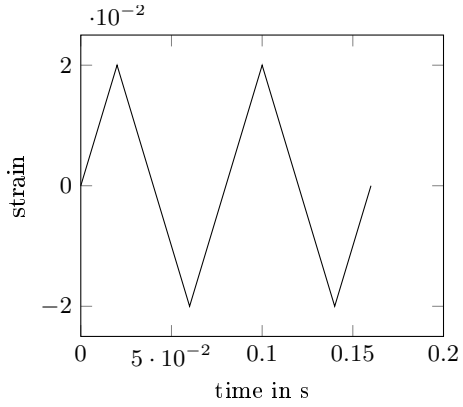

Fig. 6.4: Strain-time curve for loading history 1 (LH1) and loading history 3 (LH3)

For the validation, three different loading histories are investigated. At first a cyclic leading history is applied at room temperature, and it will be referred as LH1 (Loading History 1), shown in figure 6.4. Then a tempering process is investigated with tempering for 350 min at 600°C (LH2). The third loading history LH3 is a combined one: history two followed by history one.

The used material parameters are the determined ones from section 5.1.1 and 5.3.2. The stress responses of the three different loading histories are shown in figure 6.5 to 6.7. Since LH2 is a long term process, the computing effort for an explicit calculation is very high. Thus, only the first two seconds of the VUMAT results are compared and it shows that the slope of the curve is of the same amount as at the other calculations. Generally, all stress responses for each loading history show a very small deviation, which indicates the correct implementations for both subroutines.

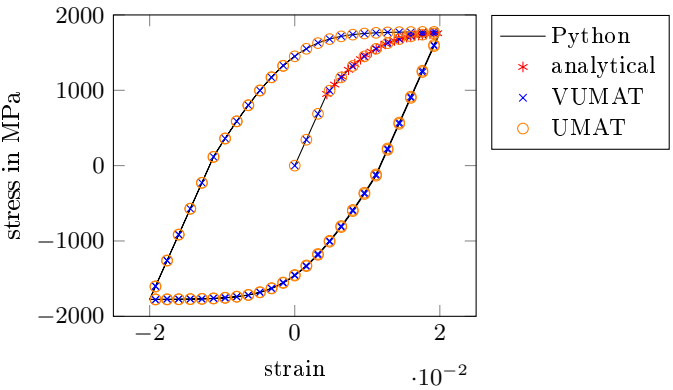

Fig. 6.5: Stress-strain curves for loading history 1 (LH1)

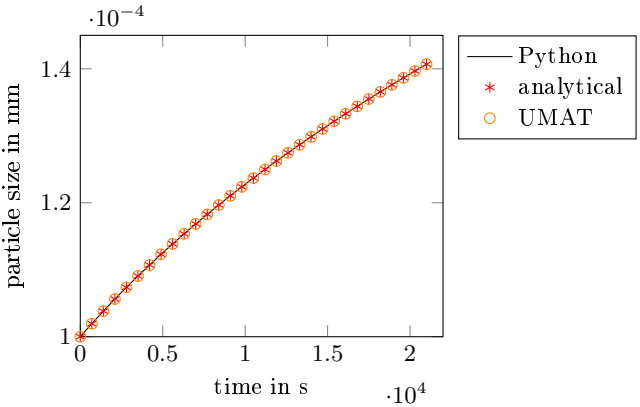

Fig. 6.6: Coarsening curve for loading history 2 (LH2)

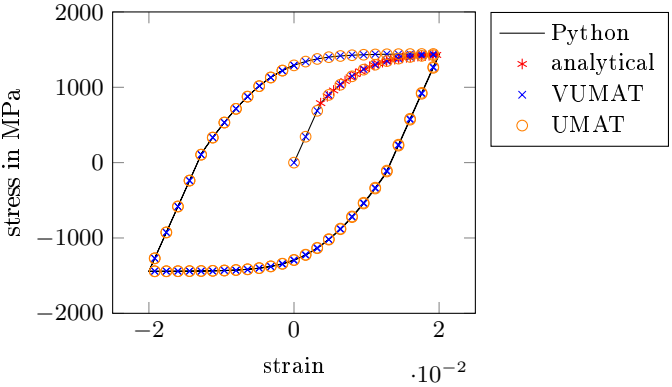

Fig. 6.7: Stress-strain curves for loading history 3 (LH3)

Chapter 7

Influence of thermal softening during die forging

A forming process is selected for which experimental tests were carried out at the IFUM [BBB+17]. The structure of the simulation model is presented in the next section. Followed by the simulation results at non-isothermal conditions with and without thermal softening.

7.1 Simulation model

The investigated process is a die forging process. Figure 7.1 and figure 7.2 illustrate the schematic process, where red areas indicate high temperatures. A hot working cycle is separated into four steps with equally time intervals: forging, unloading, ejection and cooling.

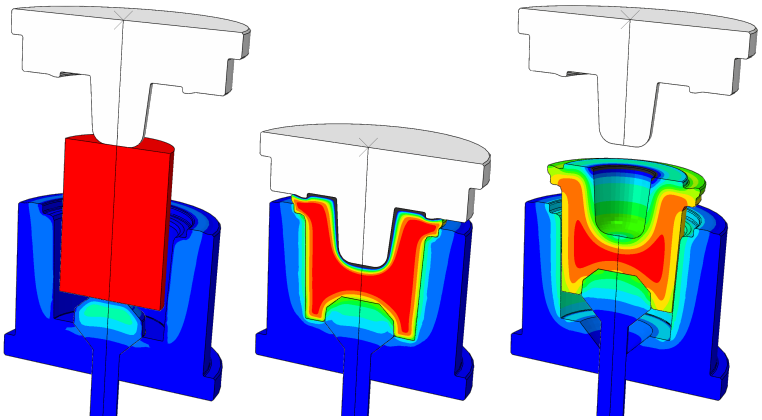

Fig. 7.1: Schematic forming process, first half cycle

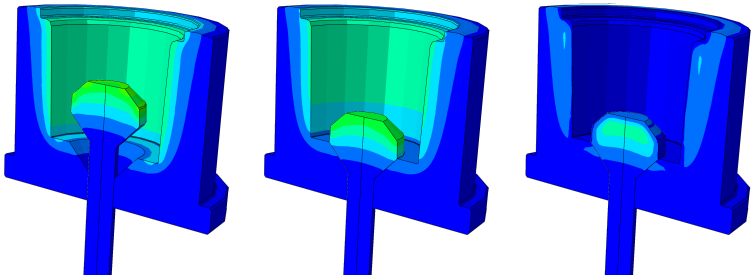

Fig. 7.2: Schematic forming process, second half cycle

7.1.1 Parts

The chosen geometries of the parts correspond to the used parts in experimental tests. The assembly consists of a blank, a punch, a die and an ejector. Their dimension is provided by the IFUM and can be found in Appendix. However, no measure of the radius in the cavity of the die is specified. Therefore, a measure is used, which turns out due to industrial production. For the production of sharp edges for hot work tools possible cutting tools have a cutting radius

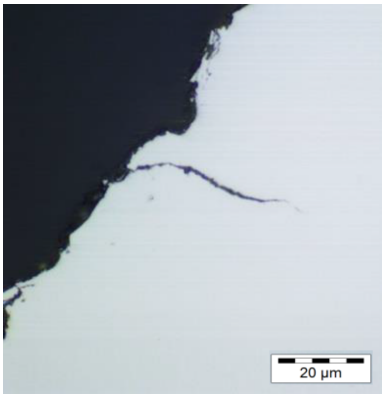

Fig. 7.3: Crack formation in the radius of die after several hot working cycles, provided by the IFUM

of approximately 0.4 mm. Therefore, this value is chosen for the radius. The simulation model is 2-dimensional and axisymmetrical. The experimental lifetime tests showed, that the die is the critical part, see figure 7.3. Hence, the punch is defined as a rigid body for saving computing effort.

7.1.2 Mesh

In case of ABAQUS/Explicit, a thermomechanically coupled simulation is used to calculate the temperature distribution after several hot working cycles. Therefore, elements out of the family 'Coupled Temperature-Displacement' are used. Since explicit dynamics do not require an equation solver, the total computing time depends largely on the number of integration points. Therefore, linear, reduced integrated elements that have only one central integration point are used. This reduces the computing time by factor three to five compared to fully integrated elements [Nas15, p. 122]. To reduce the risk of hourglassing, an artificial stiffness, using the default settings is implemented. This results in elements with the ABAQUS specific name: CAX4RT (a 4-node thermally coupled axisymmetric quadrilateral, bilinear displacement and temperature, reduced integration,

hourglass control).

To allow the blank to be able to flow in all cavities, the mesh must be chosen fine enough. On the other hand, the mesh should not be too fine to reduce computing effort. Hence, a suitable element length for the blank's mesh was found to be 0.6 mm (approximate global size), see figure 7.4 a). Since large deformations take place during the investigated hot working process, Arbitrary Lagrangian-Eulerian (ALE) adaptive meshing is used for the blank's mesh. The ALE technique is a combination of a Lagrangian and an Eulerian mesh. For the edges, the Langragian mesh, which is firmly connected to the part is used. For the internal elements, however, the Eulerian mesh is used. As a result, the inner nodes can move independently of the part, and thus avoid inappropriate element geometries. As a consequence, the ALE technique enables to maintain a high-quality mesh throughout the analysis [Sys16]. The used element length for the tools (punch, ejector and die) is 2 mm.

For the calculation with ABAQUS/Standard, the die's mesh is refined in the critical area (in the radius of the cavity) with a element length of 0.5 mm, see figure 7.4 b). In this case, no thermomechanically coupled simulation is needed, since the temperature distribution is predetermined through the results of the explicit calculation, see section 7.1.7. Additionally, no reduced integrated elements for reducing computing effort are needed. Therefore, elements with the ABAQUS specific name CAX4 (a 4-node bilinear axisymmetric quadrilateral) are used.

7.1.3 Mechanical boundary conditions

For the blank and the ejector, an x-symmetry ($u_1 = u_2 = ur_3 = 0$) is chosen on the center line (symmetry axis). The bottom line of the die is fixed in Y-direction. For the rigid body punch a sinusoidal movement according to the pressing curve of the eccentric press is used. For avoiding inertia (resistance to change in position) problems, the movement of the punch is implemented by initial velocity. The velocity time curve is shown in figure 7.5. The red dashed line indicates the end of the actual forming process. The movement of the ejector, which begins after the actual forming process is added as well.

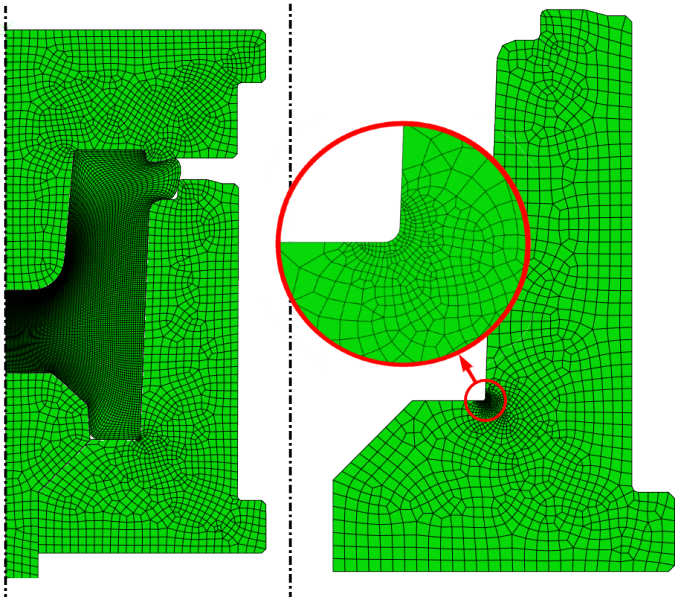

Fig. 7.4: a) mesh whole model b) die with mesh refinement

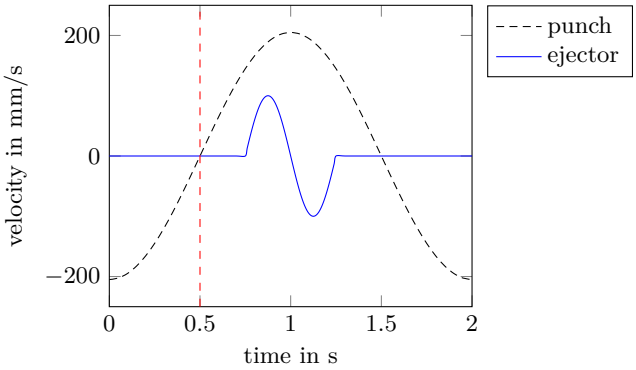

Fig. 7.5: Velocity-time curve of the hot working tools

7.1.4 Thermal boundary conditions

For the start temperature of the tools, a value of 500 °C is defined. The temperature distribution within the cycles result from friction, conduction and convection.

In cooperation with Dennis Tritschler [Tri18], the thermomechanical properties for friction, radiation and conduction were determined. The heat radiation makes a very small contribution to the temperature development during the short cycle time. Hence, it is neglected in the simulation model. The used material parameters for conductivity and specific heat can be found in [Tri18].

The cooling by injection of emulsion is approximated by convection. Therefore, the convection coefficient at the surface of the tool cavity is chosen such that the surface temperature at the end of the cycle approaches the start temperature. The resulting convection coefficient for this area is 100 $\mathrm{mW/(mm^2K)}$ and the sink temperature is 500 °C. In addition, the free convection of the outer surface is considered. It is calculated with the parameters and empirical formulas from [VDI13]. Although the condition of the small temperature difference is not met, the case of independent material properties is nevertheless assumed for the sake of simplicity. The reference temperature is chosen to be 250 °C. The calculated convection coefficient for the outer surface is 0.06 $\mathrm{mW/(mm^2K)}$, and corresponds to moderately moving air perpendicular to a metal wall [Kuc14, p. 646]. The ambient temperature is 20 °C.

7.1.5 Contact definitions

The contact type surface to surface with penalty contact method is used. The friction coefficient is set to 0.1, which is between the dry sliding friction (0.15) and the greased sliding friction (0.05) of steel on steel [BB17, p. 93]. For heat generation it is assumed that all dissipated energy is converted to heat.

7.1.6 Materials

The blank's material was defined in cooperation with Johannes Kurz [Kur16]. The required material parameters were provided by

the IFUM. The yield stress is calculated using the Hensel-Spittel approach [HS78]

$$k_f = Ae^{m_1 T}\phi^{m_2}\dot{\phi}^{m_3}e^{\frac{m_4}{\phi}} \tag{7.1}$$

with the temperature-independent material parameters A, m_1, m_2, m_3 and m_4. The values for the material 1.7225 (42CrMo4) are summarized in table 7.1.

A	1872
m_1	-0.0029
m_2	-0.1123
m_3	0.1437
m_4	-0.0488

Table 7.1: Hensel-Spittel-factors for 1.7225

The application range of the calculated flow curves lies between the strains 0.04 and 4, between the strain rates of 0.001 and 500 1/s and between the temperatures of 687.6 and 1250 °C. The flow curves calculated from equation (7.1) at the initial temperature of 1200 °C in the specified range $0.04 \leq \phi \leq 4$ are shown in figure 7.6. To generate a distinctive plastic zone in the radius of the die, these flow curves of the blank are scaled by scaling factor 2. The calculated flow curves are tabular implemented in ABAQUS using strain-, strain-rate- and temperature-dependent data.

For the material of the punch, ejector and die, the user subroutines UMAT or VUMAT, respectively with the determined material parameters are implemented, see section 6.3. Additionally, a simplified model based on the measured stress-strain curves is used to reduce computing effort, see section 7.1.7.

7.1.7 Simulation technique

Figure 7.7 summarizes the simulation technique. First, the whole model is used to determine the temperature distribution and the mechanical loads during a stabilized cycle. This calculation is performed due to the high nonlinearities with ABAQUS/Explicit. The results are then passed to a submodel that consists only of the die

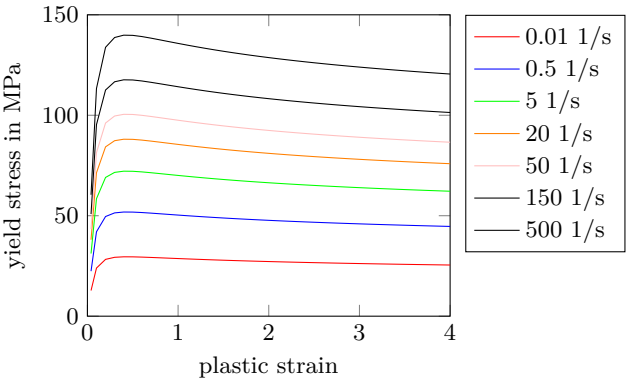

Fig. 7.6: Hensel-Spittel flow curves at 1200 °C for 1.7225

with a mesh refinement at the critical point (radius of the cavity). Due to the mesh refinement and the missing contact, the simulation continues using ABAQUS/Standard. With the unstressed die, three cycles are simulated to achieve an almost stabilized hysteresis. Then, the tempering process itself takes place, where 10000 cycles are simulated by one scaled cycle. Finally, six cycles are performed in the tempered condition.

For the determination of the temperature distribution, a dynamic (quasi-static), thermomechanically coupled analysis is used. For improving computational efficiency, mass scaling is used by scaling to a specified minimum stable time increment, see equation (2.44). The mass scaling is chosen in order that the kinetic energy generated by inertial effects is lower than 5 % of the total strain energy [Nas15, p. 124]. Since very little time passes during the first cycles, the influence of thermal softening is negligible in determining the temperature curve within a cycle. This is why kinematic plasticity which is already implemented in ABAQUS is used. Thus, the VUMAT is not needed and computing time is reduced. The used parameters (at $r_0 = 0.1\mu\text{m}$) are shown table 7.2.

For saving even more computing effort, the second half cycle (ejection and cooling) is simulated in a new job without blank and

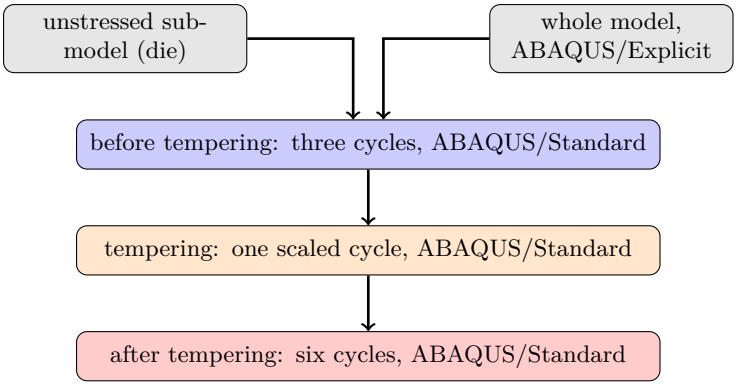

Fig. 7.7: Schematic structure of simulation technique

temperature in °C	yield stress in MPa	kinematic modulus C in MPa	kinematic hardening exponent γ
20	950.9	270518.7	327.7
200	910.6	270518.7	378.2
300	869.1	270518.7	421.8
400	791.8	270518.7	473.3
500	659.5	270518.7	525.4
600	509.1	270518.7	572.1

Table 7.2: Parameters for kinematic hardening

punch. Since blank and punch are not in contact with the other parts during the second half cycle, an exclusion does not affect the simulation results of the die. With predefined fields, the results of the previous simulation (last step, last increment) can be defined as initial state for die and ejector.

For the following cycles, the results of the previous calculation are transmitted. Therefore, the results of the last step are again defined as a 'predefined field' in the initial state. In this way, the cycles are repeated until the cyclic temperature distribution in the surface within the current cycle hardly changes compared to the previous

one. The simulation has shown that this condition is reached after approximately ten cycles.

Then, the last cycle is used to transfer its results (temperatures and loads) to a submodel. The submodel consists only of the die, since it contains the critical area. The mesh in this critical area is refined (element length of 0.1 mm) for further investigations. Because of the small elements and the absence of complex contacts, the static implicit calculation with ABAQUS/Standard using the described UMAT (section 6.3) is better suited, compare section 2.3.2.

In order to reach the stabilized hysteresis, three cycles are simulated. With the third cycle, the material's behavior before tempering should be evaluated. Afterwards, the tempering during 10000 cycles (approximate limit of LCF [RBH06, p. 361]) is calculated. For saving computing time, one cycle is scaled in a way to obtain the same effects as at many single cycles. To this end, the aging parameter (here the particle radius r) should show the same evolution in this cycle as it would be the case in many cycles. Through separation of the variables in the evolution of the particle radius equation (5.3) one obtains

$$r^2 \mathrm{d}r = k \mathrm{d}t = k_1 \frac{e^{-\frac{Q}{RT}}}{T} \mathrm{d}t. \tag{7.2}$$

Integrating the left side leads to

$$\frac{r^3}{3} - \frac{r_0^3}{3} = \int_0^t k \mathrm{d}t = \int_0^t k_1 \frac{e^{-\frac{Q}{RT}}}{T} \mathrm{d}t. \tag{7.3}$$

Assuming that the same temperature curve is repeated n times, the right side may be expressed by

$$n \int_0^{t_{\mathrm{cy}}} k(t) \mathrm{d}t = n \left[K(t) \right]_0^{t_{\mathrm{cy}}} \tag{7.4}$$

with t_{cy} being the cycle time and $K(t)$ being the integral of $k(t)$. For the scaled cycle, the time is scaled by the inverse of the cycle number n. Thus, the scaled cycle time is $n\, t_{\mathrm{cy}}$. The integral of the scaled cycle can now be calculated by

$$\int_0^{n\, t_{\mathrm{cy}}} k \left(\frac{t}{n} \right) \mathrm{d}t = \left[nK \left(\frac{t}{n} \right) \right]_0^{n\, t_{\mathrm{cy}}}. \tag{7.5}$$

Both cases, equation (7.4) and equation (7.5) result in

$$n\left(K(t_{\mathrm{cy}}) - K(0)\right). \tag{7.6}$$

Thus, the scaled long cycle can be used instead of n (=10000) short cycles without losing computing accuracy. Then, six cycles are simulated to reach a stabilized hysteresis and to evaluate the material's behavior after tempering.

7.2 Results

For direct comparison of the simulations, the same result variables and representations are used. These are in particular temperature, von Mises stress, accumulated plastic strain and in case of particle hardening the particle size. For the generation of stress-strain hysteresis, the direction must be assigned to stresses and strains. This can be achieved through the hydrostatic pressure $\sigma_{\mathrm{m}} = -1/3\,\mathrm{tr}(\boldsymbol{\sigma})$. For this purpose, the sign information of the von Mises stress is assigned by

$$\sigma_{\mathrm{eq,sgn}} = \sigma_{\mathrm{eq}}\ \mathrm{sgn}\left(\sigma_{\mathrm{m}}\right). \tag{7.7}$$

For the accumulated plastic strain, the sign information is iterative added by

$$\bar{\varepsilon}^{\mathrm{p}}_{\mathrm{sgn},n+1} = \bar{\varepsilon}^{\mathrm{p}}_{\mathrm{sgn},n} + \Delta\bar{\varepsilon}^{\mathrm{p}}\ \mathrm{sgn}\left(\sigma_{\mathrm{m}}\right). \tag{7.8}$$

The temperature distribution in the tenth cycle, before the cooling takes place (right after ejection) is shown in figure 7.8. The most critical point in regard of lifetime is marked with red cycles in the section area. The temperature curve of this critical point (radius in the cavity) within the tenth cycle is shown in figure 7.9. When the curve is compared with figure 4.1, it shows that a significant coarsening is to be expected.

7.2.1 Without thermal softening

For the simulation without thermal softening, the particle radius is held constant ($r = 0.1\,\mu\mathrm{m}$) in the UMAT (no particle coarsening). Figure 7.10 shows the stress-strain hysteresis loops that arise when no thermal softening is considered. The loops show a ratcheting

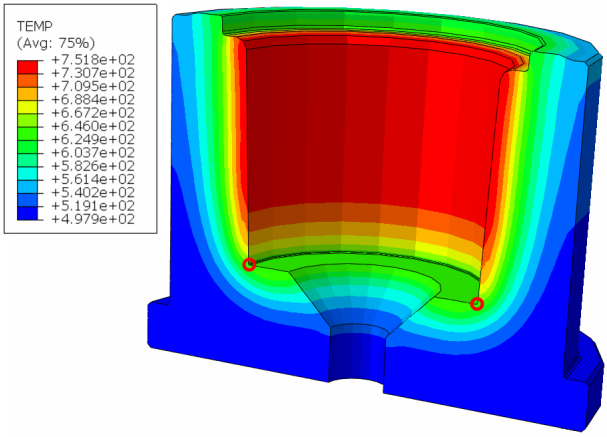

Fig. 7.8: Temperature distribution in the tenth cycle, before cooling (after ejection)

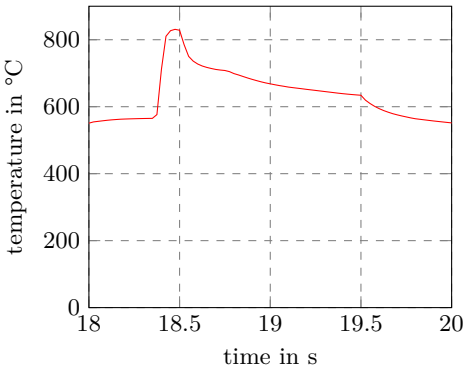

Fig. 7.9: Temperature curve of the critical point within the tenth cycle

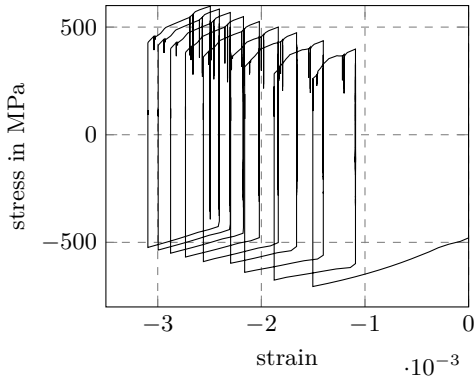

Fig. 7.10: Hysteresis loops in critical area without thermal softening

effect. However, the ratcheting strain continues to decline and a steady hysteresis seems to approach. Furthermore, there is almost no difference between the cycles before aging (first three) and after aging (following six).

7.2.2 Including thermal softening

Since the thermal softening is no longer suppressed in current calculation, the distribution of the particle radius can be investigated, see Fig. 7.11 a), where the output SDV26 corresponds to the variable r. The distribution is shown at the end of simulation. The largest particle sizes do not occur in the radius. In addition, the particle radius in the surface area are larger than in areas with a larger distance from the surface. This is due to the fact, that the number of previous simulations to determine the temperature distribution is not sufficient to completely heat the die. However, the focus lies on the near surface regions (especially at the critical radius), where a constant temperature profile is already reached after the explicit simulation. Although the particle radius in the critical area is not maximal, this remains the highest loaded area. This is clarified in figure 7.11 b), where von Mises stress is shown and its maximum can be found in the radius of the cavity.

Figure 7.12 shows the accumulated plastic strain (SDV25 corre-

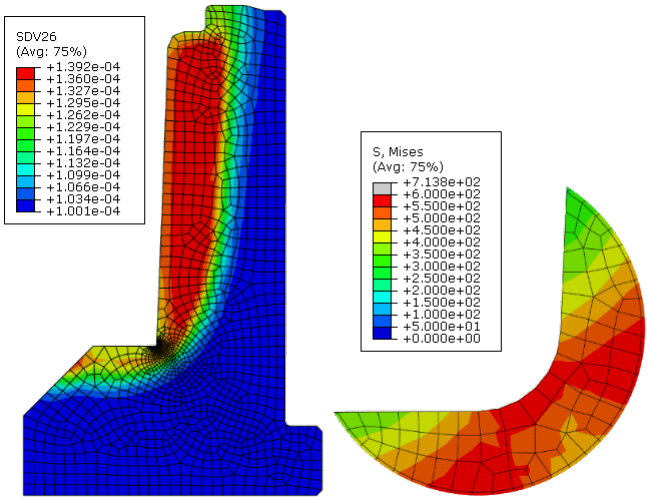

Fig. 7.11: a) Particle distribution after simulation b) von-Mises stress

sponds to $\bar{\varepsilon}^p$) after the simulation. The largest accumulated plastic strain occurs in the radius. Therefore, this area is shown enlarged. The maximum occurring accumulated plastic strain is 2.0 %. However, the strains are very localized. Stress peaks on surface nodes could be caused by inaccurate extrapolation due to a rough mesh. However, the values of the nearest integration points are 1.8 % and 1.5 %, and indicate a strong concentration in this area.

Figure 7.13 shows the stress-strain hysteresis in the radius. Here, a clear influence by softening (between third and fourth cycle) can be seen. Analogous to figure 7.10, a ratcheting effect occurs, which decreases, and thus presumably approaches a steady state. To compare the two stress-strain hysteresis, both are shown in figure 7.14. The first three cycles are not shown because they match exactly, whereas, the following six cycles show a clear deviation. In particular, the strain range is much larger with thermal softening than without.

For further comparison, the accumulated plastic strains are shown in figure 7.15. The strain range per cycle is about twice as large when the thermal softening is considered. The strain range is

a critical quantity for lifetime evaluations and often correlates with the fatigue life. Hence, a significant reduction of lifetime can be assumed. The negligence of the thermal softening in tool design can lead to unexpected tool failure.

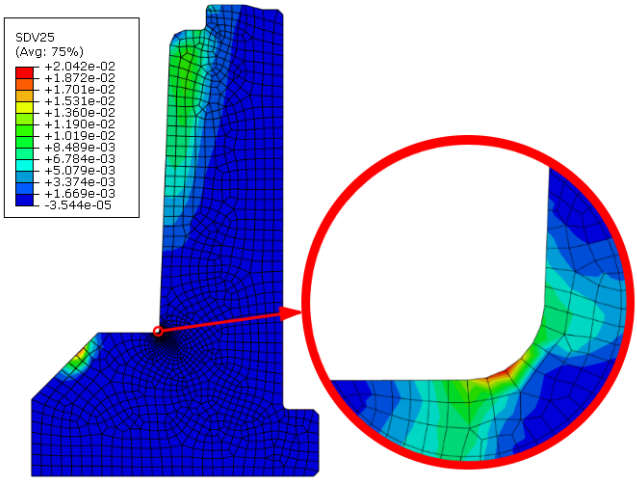

Fig. 7.12: Accumulated plastic strain distribution

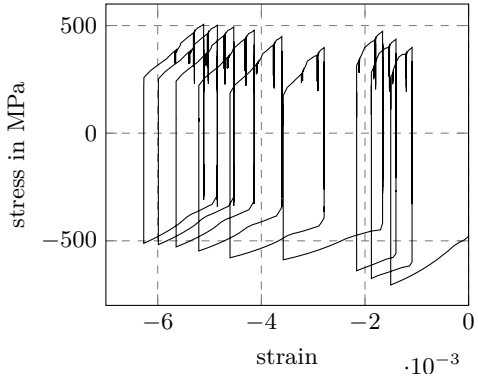

Fig. 7.13: Hysteresis loops in critical area including thermal softening

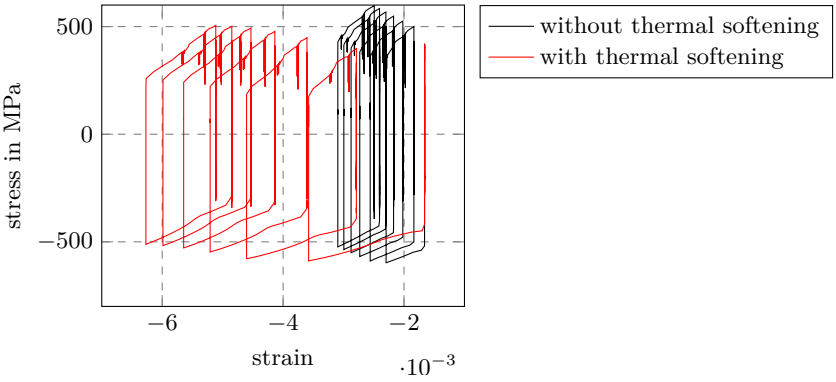

Fig. 7.14: Hysteresis loops in critical area after tempering

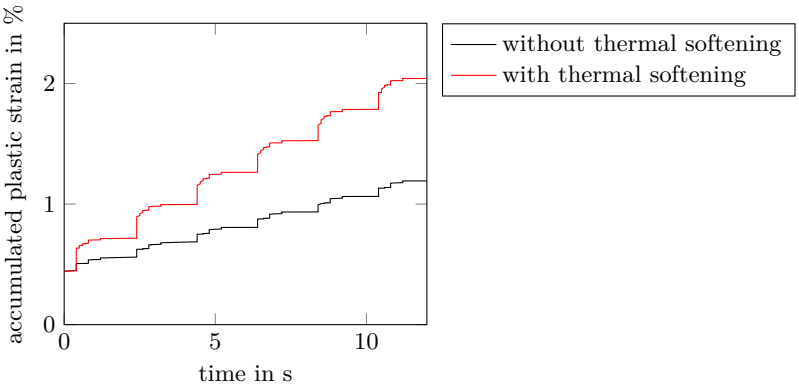

Fig. 7.15: Accumulated plastic strain after tempering

Chapter 8

Discussion

In this work, models for the description of time- and temperature-dependent plasticity are developed and applied to describe the stress-strain hysteresis loops measured at different temperatures and for different heat treatments. The models consist of a kinetic model and a mechanical model. Currently, an interaction of both models is not included, so that the evolution of the microstructure has an effect on the mechanical behavior but not vice versa. Generally, additional dependencies can be included into the kinetic model by adding, e.g. contributions to the evolution of the mean particle radius by plastic deformations to consider an accelerated diffusion by pipe diffusion with moving dislocations, see equation (3.16). In this work, however, the mechanical properties are investigated on specimen that did not experience plastic deformations during tempering rather than on specimen that continuously softened during a mechanical test. The latter is advisable for future investigations to gain information on the interaction. Furthermore, these investigations could validate if the model is already able to describe continuous softening of a specimen that softens during cyclic loadings at higher temperatures.

In the kinetic model, the evolution of the mean particle radius is described for one type of particle species. It is assumed that one carbide species exists that dominantly determines the mechanical properties. For hot work tool steels, however, several carbides can be identified [Abe04, HLWZ06, KPJ+15, LWL+15]. Microstruc-

tural investigations should clarify which carbides primarily prevent dislocation motions for the considered hot work tool steel 1.2367. Nevertheless, a good description of the isothermal hardening curves as well as the non-isothermal hardening curve is obtained with the current model and the determined material properties. In particular, the determined temperature dependency of the coarsening constant corresponds very well to the description with the Arrhenius equation with a reasonable value for the activation energy for diffusion of 235 kJ/mol. This value is in the order of typical values for the activation energy of diffusion [CDW+09, HHH98, Tru08].

Generally, since only one cyclic test per material state and thermal and mechanical loading condition is performed, some scatter in the experimental data can be expected. However, a good overall description of the temperature-dependent cyclic material properties after time and temperature-dependent softening is achieved with the models. The peak in cyclic yield stress (Ramberg-Osgood), as well as in yield strength (cyclic plasticity model) observed for the untempered (HT0) material is maybe due to dynamic strain aging. However, serrated flow is not found in the related stress-strain data. Further investigations could give more insight in which temperature and strain rate range and for which material state dynamic strain aging occurs. The observed higher yield stresses for 400 and 500 °C for the HT0 heat treated material could be described using a phenomenological approach based on the results of further investigations.

Since a mechanism-based approach is developed for the description of the kinetics and the temperature-dependent cyclic yield stress, it can be assumed that the models as well as the methodology for the determination of the corresponding material properties can be applied to other hot work tool steels as well as long as the mechanisms are the same (i.e. Ostwald ripening, Orowan mechanism). The temperature and particle radius dependencies of the material properties C_∞ and C are also based on this mechanism-based approach since it provides a good description of the considered measured values and the properties also have the unit of the stress. The transferability of the developed models to other hot work tool steels is, however, only possible if the linear correlations between yield stress, cyclic yield stress and hardness prevail. Linear correlations between yield

stress and hardness of various nonaustenitic, hypoeutectoid steels are documented in [Pv08]. Moreover, the temperature dependency of the hardening exponent is based on a purely phenomenological equation that might need adaption if another steel is considered. A mechanism-based approach to describe the temperature dependency of the hardening exponent is desired but not known by the author.

The material properties $m_{\mathrm{cy}} = 4$ for the description of the thermal part of the cyclic yield stress and as well as $m_{\mathrm{e}} = 4$ in the description of yield strength are consistent with the documented one in [MZ14, p. 213], whereas, the material property $n_{\mathrm{cy}} = 5.76$ (Ramberg-Osgood model) and $n_{\mathrm{e}} = 7.5$ respectively (cyclic plasticity model) differs from the documented value of $n = 1$. The higher values of n provide a better fitting of the observed loss in strength at higher temperatures as it would be the case for $n = 1$. For the description of C_∞ the material property m_∞ was also found to be 4 and the obtained value of $n_\infty = 2.73$ was even closer to the documented one of 1.

The Ramberg-Osgood model can well be integrated into the mechanism-based model for thermomechanical fatigue crack growth in [SR10, SSS$^+$10], see section 3.3. Thus, the combination of the Ramberg-Osgood model with its time and temperature-dependent material properties and the model for thermomechanical fatigue crack growth enables the integration of softening into fatigue life assessment of hot work tools. However, it is not suitable for the integration into finite element programs.

The incremental plasticity model is implemented in the finite element program ABAQUS. In section 6.4 the ABAQUS subroutines UMAT and VUMAT are compared with a Python implementation and partly with analytical solutions. Since a very good agreement has been shown, a correct implementation of the model can be assumed.

With the VUMAT a thermomechanically coupled analysis can be performed to determine the temperature distribution within the die. However, this is not possible with the current UMAT. Since implicit time integration requires the derivation of the weak form of the FEM balance law of linear momentum, see equation (2.29), and the energy balance in case of a thermomechanical coupled analysis, the stress must also be derived with respect to temperature ($\partial \boldsymbol{\sigma}_{n+1} / \partial T_{n+1}$).

This can be achieved in analogy to $\partial\boldsymbol{\sigma}_{n+1}/\partial\boldsymbol{\varepsilon}_{n+1}$ in section 6.3:

$$\frac{\partial\boldsymbol{\sigma}_{n+1}}{\partial T_{n+1}} = \frac{\partial\boldsymbol{\sigma}_{n+1}}{\partial\boldsymbol{\varepsilon}^{p}_{n+1}} \cdot \frac{\partial\boldsymbol{\varepsilon}^{p}_{n+1}}{\partial T_{n+1}} \tag{8.1}$$

with

$$\frac{\partial\boldsymbol{\sigma}_{n+1}}{\partial\boldsymbol{\varepsilon}^{p}_{n+1}} = -\mathbb{C}_{n+1}. \tag{8.2}$$

For the second factor, it is again helpful to build the total differential of $\mathbf{R}$, but this time in respect to temperature

$$\frac{\mathrm{d}\mathbf{R}}{\mathrm{d}T_{n+1}} = \frac{\partial\mathbf{R}}{\partial T_{n+1}} + \frac{\partial\mathbf{R}}{\partial\mathbf{Y}_{n+1}} \cdot \frac{\partial\mathbf{Y}_{n+1}}{\partial T_{n+1}} = \mathbf{0} \tag{8.3}$$

leading to

$$\frac{\partial\mathbf{Y}_{n+1}}{\partial T_{n+1}} = -\left[\frac{\partial\mathbf{R}}{\partial\boldsymbol{Y}_{n+1}}\right]^{-1} \cdot \frac{\partial\mathbf{R}}{\partial T_{n+1}}. \tag{8.4}$$

As described in section 6.3, the first entries of $\mathbf{Y}$ correspond with the plastic strain, and thus the second factor can now be calculated. However, the derivatives $\partial\mathbf{R}/\partial T_{n+1}$ must be calculated (at the first entries), but $\partial\mathbf{R}/\partial\boldsymbol{Y}_{n+1}$ is the already calculated Jacobian matrix, see equation (6.11). Then, all variables are available for extension of the UMAT to provide thermomechanical simulation with ABAQUS/Standard. In this work, this extension is not necessary because the forming process is simulated explicit due to its high nonlinearities. However, in other applications (low nonlinearities, high mesh refinements), the model's extension may be necessary.

For the application several simplifications were made, which can strongly influence the simulation results. However, the associated goal is the evaluation of the developed model and not the evaluation of a forming process. Due to the selected boundary conditions a strong influence of thermal softening is visible in the investigated case. Nevertheless, no conclusions about forming processes in general can be made with this arbitrary application. Whether the model has an influence or not must be investigated in each specific case. The decisive factors are the temperature and the time at which it occurs. For example, a tempering time of five hours and a temperature of 500 °C leads to a mean particle radius of 100.1 nm according to equation (3.15), and thus to a yield strength of 658.8 MPa at 500 °C, see

equation (5.21). This is a very small coarsening since the initial particle radius being 100 nm. However, if the same tempering time takes place at a temperature of 600 °C, this leads to a mean particle radius of 136.3 nm, and thus to a yield strength of 537.9 MPa at 500 °C. This corresponds to a reduction of 18.4%. If high temperatures take place for a long time on mechanically highly stressed areas, this can lead to a considerable increase in plastic strain, and thus leading to a significant shortening of the lifetime.

In the investigated process, a doubling of the strain range has been shown by the consideration of the softening. This is a significant increase, which probably greatly reduces the lifetime. If, in this case, the developed model is not used for tool design, it can lead to an unexpected tool failure, and thus bringing the production to a standstill.

In the current plasticity model, time-dependent behavior as stress relaxation, creep and strain rate dependency are not yet considered. These phenomena might, however, occur at the high temperatures considered. The extension of the plasticity model used in this work to time-dependent behavior can easily be done by introducing a corresponding flow rule using an overstress formulation [Cha86, Cha89]. Therefore, values greater than zero must be allowed for ϕ in equation (2.16). The plastic multiplier λ can be calculated by equation (3.1) to take viscoplastic behavior into account. Furthermore, the last entry of the residual must be replaced by

$$R_{\bar{\varepsilon}^p} = -\bar{\varepsilon}^p_{n+1} + \bar{\varepsilon}^p_n \Delta t \lambda_{n+1} \tag{8.5}$$

leading to the following Jacobian

$$\boldsymbol{J}\left(\boldsymbol{Y}_{n+1}\right) = -\boldsymbol{I}\boldsymbol{I} + \Delta t \boldsymbol{D}_{n+1} \otimes \frac{\partial \lambda_{n+1}}{\partial \boldsymbol{Y}_{n+1}} + \Delta t \lambda_{n+1} \frac{\partial \boldsymbol{D}_{n+1}}{\partial \boldsymbol{Y}_{n+1}} + \frac{\partial \boldsymbol{M}_{n+1}}{\partial \boldsymbol{Y}_{n+1}}. \tag{8.6}$$

In addition, static recovery of the backstress, see equation (2.18) can be considered with the parameter R leading to

$$\dot{\boldsymbol{\alpha}} = \frac{2}{3} C \dot{\boldsymbol{\varepsilon}}^p - \gamma \dot{\bar{\varepsilon}}^p \boldsymbol{\alpha} - R \boldsymbol{\alpha}. \tag{8.7}$$

For the determination of the material parameters n, K and R, further experimental data is needed, where dwell times in stress or strain and different strain rates are applied.

Nevertheless, with the three-dimensional formulation of the cyclic plasticity model and its numerical implementation into a finite element program, the effect of softening on the thermomechanical fatigue life of hot work tools can be assessed.

Chapter 9

Summary and conclusions

The state of the art shows that there are currently no mechanism-based models for the thermomechanical fatigue life prediction of hot working tools available.

In this thesis, the temperature-dependent cyclic material properties are determined for the martensitic hot work tool steel 1.2367 (x38CrMoV5-3) after time- and temperature-dependent softening. A model is proposed that describes the kinetics of microstructural changes during tempering.

Furthermore, the correlations of the microstructural changes with changes in the material properties of the Ramberg-Osgood model are determined and a model for its time- and temperature-dependent behavior is developed. With the model a description of the cyclic mechanical properties during tempering at various tempering times and temperatures is possible. It can well be integrated in mechanism-based models for thermomechanical fatigue life prediction of hot work tools.

Since, the Ramberg-Osgood model is not suitable for finite element calculations, a temperature-dependent incremental cyclic plasticity model with kinematic hardening and thermal softening is developed. With the model a continuous description of the cyclic me-

chanical properties during tempering at various tempering times and temperatures is possible and time- and temperature-dependent softening can be accounted for in finite element calculations.

The developed incremental cyclic plasticity model is implemented in the finite element Program ABAQUS via subroutines for implicit integration (UMAT) and explicit integration (VUMAT). Both subroutines use a predictor-corrector method. The calculation of the internal variables at plastic corrector step is done through implicit integration using the Newton-Method. For the calculation of the Jacobian the analytical derivatives are implemented.

The subroutines are used to simulate an exemplary hot work process. The results are compared with a calculation where no thermal softening is considered. The simulation with thermal softening by particle coarsening show a significant increase of plastic strain range. This demonstrates, if the developed model is not considered in tool design, unexpected tool failure might occur.

Bibliography

[Abe04] F. Abe. Coarsening behavior of lath and its effect on creep rates in tempered martensitic 9cr–w steels. *Materials Science and Engineering: A*, 387-389:565–569, 2004. doi:10.1016/j.msea.2004.01.057.

[Alt18] H. Altenbach. *Kontinuumsmechanik*. Springer Berlin Heidelberg, Berlin, Heidelberg, 2018. doi:10.1007/978-3-662-57504-8.

[BB17] A. Böge and W. Böge. *Technische Mechanik*. Springer Fachmedien Wiesbaden, Wiesbaden, 2017. doi:10.1007/978-3-658-16203-0.

[BBB+17] A. Bouguecha, B.-A. Behrens, C. Bonk, D. Rosenbusch, and M. Kazhai. Numerical die life estimation of a crack susceptible industrial hot forging process. AIP Conference Proceedings, page 190012. Author(s), 2017. doi:10.1063/1.5008225.

[Ber82] D. P. Bertsekas. Projected newton methods for optimization problems with simple constraints. *SIAM Journal on Control and Optimization*, 20(2):221–246, 1982. doi:10.1137/0320018.

[Ber99] G. Bernhart. High temperature low cycle fatigue behaviour of a martensitic forging tool steel. *International Journal of Fatigue*, 21(2):179–186, 1999. doi:10.1016/S0142-1123(98)00064-4.

[BM05] G. A. Berti and M. Monti. Thermo-mechanical fatigue life assessment of hot forging die steel. *Fatigue Fracture of Engineering Materials and Structures*, 28(11):1025–1034, 2005. doi:10.1111/j.1460-2695.2005.00940.x.

[BMN11] R. Bürgel, H.-J. Maier, and T. Niendorf. *Handbuch Hochtemperatur-Werkstofftechnik: Grundlagen, Werkstoffbeanspruchungen, Hochtemperaturlegierungen und -beschichtungen*. Praxis. Vieweg + Teubner, Wiesbaden, 4., überarb. auflage edition, 2011.

[BU17] Böhler-Uddeholm AG. Heat treatment of tool steel, 2017. URL http://www.uddeholm.com/files/heattreatment-english.pdf.

[CC89] E. Contesti and G. Cailletaud. Description of creep-plasticity interaction with non-unified constitutive equations: application to an austenitic stainless steel. *Nuclear Engineering and Design*, 116(3):265–280, 1989. doi:10.1016/0029-5493(89)90087-3.

[CDW+09] H. Chilukuru, K. Durst, S. Wadekar, M. Schwienheer, A. Scholz, C. Berger, K. H. Mayer, and W. Blum. Coarsening of precipitates and degradation of creep resistance in tempered martensite steels. *Materials Science and Engineering: A*, 510-511:81–87, 2009. doi:10.1016/j.msea.2008.04.088.

[Cha86] J. L. Chaboche. Time-independent constitutive theories for cyclic plasticity. *International Journal of Plasticity*, 2(2):149–188, 1986. doi:10.1016/0749-6419(86)90010-0.

[Cha89] J. L. Chaboche. Constitutive equations for cyclic plasticity and cyclic viscoplasticity. *International Journal of Plasticity*, 5(3):247–302, 1989. doi:10.1016/0749-6419(89)90015-6.

[Cof54] L. F. Coffin. A study of the effects of cyclic thermal stresses on a ductile metal. *trans. ASME*, 76(76):931–950, 1954.

[CSE+02] D. Caliskanoglu, I. Siller, R. Ebner, H. Leitner, F. Jeglitsch, and W. Waldhauser. Thermal fatigue and softening behavior of hot work tool steels. *Proceedings of the 6th International Tooling Conference*, pages 707–719, 2002.

[DB10] E. Doege and B.-A. Behrens. *Handbuch Umformtechnik: Grundlagen, Technologien, Maschinen*. VDI-Buch. Springer-Verlag Berlin Heidelberg, Berlin, Heidelberg, 2010.

[DeG03] E. P. DeGarmo. *Materials and processes in manufacturing*. Wiley, Hoboken, N.J., 9th ed. edition, 2003.

[DES18] Deutsche Edelstahlwerke Services GmbH. Thermodur 2367 superclean / thermodur 2367 efs: Werkstoffdatenblatt x38crmov5-3 1.2367, 2018. URL https://www.dew-stahl.com/fileadmin/files/dew-stahl.com/documents/Publikationen/Werkstoffdatenblaetter/Werkzeugstahl/Warmarbeitsstahl/2367_Thermodur_de.pdf.

[Eba10] R. Ebara. Fatigue crack initiation and propagation behavior of forging die steels. *International Journal of Fatigue*, 32(5):830–840, 2010. doi:10.1016/j.ijfatigue.2009.07.020.

[EBHG+17] A. Escolán, J. M. Bielsa, B. Hernández-Gascón, M. A. Jiménez, J. López, and R. Allende. Thermomechanical fatigue approach to predict tooling life in high temperature metal forming processes. *International Journal of Material Forming*, 10(4):535–545, 2017. doi:10.1007/s12289-016-1299-2.

[EL88] G. Engberg and L. Larsson. Elevated-temperature low cycle and thermomechanical fatigue properties of aisi h13 hot-work tool steel. In H. D. Solomon, G. R. Halford, L. R. Kaisand, and B. N. Leis, editors, *Low Cycle Fatigue*, pages 576–576–12. ASTM International, 100

Barr Harbor Drive, PO Box C700, West Conshohocken, PA 19428-2959, 1988. doi:10.1520/STP24507S.

[FA07] C. O. Frederick and P. J. Armstrong. A mathematical representation of the multiaxial bauschinger effect. *Materials at High Temperatures*, 24(1):1–26, 2007. doi:10.3184/096034007X207589.

[GKS08] A. Grüning, M. Krauß, and B. Scholtes. Isothermal fatigue of tool steel aisi h11. *steel research international*, 79(2):111–115, 2008. doi:10.1002/srin.200806325.

[GLS10] A. Grüning, M. Lebsanft, and B. Scholtes. Cyclic stress–strain behavior and damage of tool steel aisi h11 under isothermal and thermal fatigue conditions. *Materials Science and Engineering: A*, 527(7-8):1979–1985, 2010. doi:10.1016/j.msea.2009.11.031.

[HHH98] H. Hildebrand, G. Heinzel, and D. Heger. Aktivierungsenergie der wiederholten Karbidausscheidung in Stählen. *Materialwissenschaft und Werkstofftechnik*, 29(1):16–22, 1998. doi:10.1002/mawe.19980290107.

[HLWZ06] X. Hu, L. Li, X. Wu, and M. Zhang. Coarsening behavior of m23c6 carbides after ageing or thermal fatigue in aisi h13 steel with niobium. *International Journal of Fatigue*, 28(3):175–182, 2006. doi:10.1016/j.ijfatigue.2005.06.042.

[HS78] A. Hensel and T. Spittel. *Kraft- und Arbeitsbedarf bildsamer Formgebungsverfahren*. Deutscher Verlag für Grundstoffindustrie, 1978.

[JFG01] Q. C. Jiang, J. R. Fang, and Q. F. Guan. Thermomechanical fatigue behavior of cr–ni–mo cast hot work die steel. *Scripta Materialia*, 45(2):199–204, 2001. doi:10.1016/S1359-6462(01)01015-6.

[JS18a] A. Jilg and T. Seifert. Temperature dependent cyclic mechanical properties of a hot work

steel after time and temperature dependent softening. *Materials Science and Engineering: A*, 2018. doi:10.1016/j.msea.2018.02.048.

[JS18b] A. Jilg and T. Seifert. A temperature dependent cyclic plasticity model for hot work tool steel including particle coarsening. AIP Conference Proceedings, page 170007. Author(s), 2018. doi:10.1063/1.5035064.

[JSB17] A. Jilg, T. Seifert, and A. Bouguecha. Ermüdungslebensdauerbewertung von Warmumformwerkzeugen - Ein Überblick über den Stand der Forschung und Anwendung. *Materialwissenschaft und Werkstofftechnik*, 48(11):1057–1069, 2017. doi:10.1002/mawe.201700059.

[KGS81] V. Kumar, M. D. German, and C. F. Shih. *Engineering approach for elastic-plastic fracture analysis*. General Electric Company, 1981. doi:10.2172/6068291.

[KPJ+15] M. Kang, G. Park, J.-G. Jung, B.-H. Kim, and Y.-K. Lee. The effects of annealing temperature and cooling rate on carbide precipitation behavior in h13 hot-work tool steel. *Journal of Alloys and Compounds*, 627:359–366, 2015. doi:10.1016/j.jallcom.2014.11.189.

[Kuc14] H. Kuchlin. *PHYSIK, 21.A*. Carl Hanser Verlag, [S.l.], 2014.

[Kur16] J. Kurz. *Finite-Elemente-Berechnung eines Schmiedeprozesses mit Abaqus/Explicit zur Bewertung der Werkzeugbelastung*. seminar paper, University of Applied Sciences Offenburg, 2016.

[LH14] D. E. Laughlin and K. Hono. *Physical metallurgy*. Elsevier, Amsterdam, 5th ed. edition, op. 2014.

[LWL+15] T.-S. Li, F.-M. Wang, C.-R. Li, G.-Q. Zhang, and Q.-Y. Meng. Carbide evolution in high molybdenum nb-microalloyed h13 steel during annealing process. *Journal of Iron and Steel Research, Inter-*

national, 22(4):330–336, 2015. doi:10.1016/S1006-706X(15)30008-X.

[LY16] D. G. Luenberger and Y. Ye. *Linear and Nonlinear Programming*, volume 228. Springer International Publishing, Cham, 2016. doi:10.1007/978-3-319-18842-3.

[Man54] S. S. Manson. Behavior of materials under conditions of thermal stress. *NACA Technical Report*, 1170(1770):1–34, 1954.

[MBGA09] A. Medvedeva, J. Bergström, S. Gunnarsson, and J. Andersson. High-temperature properties and microstructural stability of hot-work tool steels. *Materials Science and Engineering: A*, 523(1-2):39–46, 2009. doi:10.1016/j.msea.2009.06.010.

[MHKA14] D. Mellouli, N. Haddar, A. Köster, and H. F. Ayedi. Hardness effect on thermal fatigue damage of hot-working tool steel. *Engineering Failure Analysis*, 45:85–95, 2014. doi:10.1016/j.engfailanal.2014.06.007.

[Mor77] J. J. Moré. The levenberg-marquardt algorithm: Implementation and theory. *Lecture Notes in Mathematics*, 630:105–116, 1977.

[MR10] D. C. Montgomery and G. C. Runger. *Applied Statistics and Probability for Engineers, Fifth Edition*. John Wiley & Sons, 2010.

[MZ14] E. Macherauch and H.-W. Zoch. *Praktikum in Werkstoffkunde*. Springer Fachmedien Wiesbaden, Wiesbaden, 2014. doi:10.1007/978-3-658-05038-2.

[Nas15] L. Nasdala. *FEM-Formelsammlung Statik und Dynamik*. Springer Fachmedien Wiesbaden, Wiesbaden, 2015. doi:10.1007/978-3-658-06630-7.

[NS89a] R. W. Neu and H. Sehitoglu. Thermomechanical fatigue, oxidation, and creep: Part i. damage mechanisms. *Metallurgical Transactions A*, 20(9):1755–1767, 1989. doi:10.1007/BF02663207.

[NS89b] R. W. Neu and H. Sehitoglu. Thermomechanical fatigue, oxidation, and creep: Part ii. life prediction. *Metallurgical Transactions A*, 20(9):1769–1783, 1989. doi:10.1007/BF02663208.

[ØP00] T. Ørts Pedersen. Numerical modelling of cyclic plasticity and fatigue damage in cold-forging tools. *International Journal of Mechanical Sciences*, 42(4):799–818, 2000. doi:10.1016/S0020-7403(99)00019-3.

[Pv08] E. J. Pavlina and C. J. van Tyne. Correlation of yield strength and tensile strength with hardness for steels. *Journal of Materials Engineering and Performance*, 17(6):888–893, 2008. doi:10.1007/s11665-008-9225-5.

[RBH06] J. Rösler, M. Bäker, and H. Harders. *Mechanisches Verhalten der Werkstoffe: Mit 31 Tabellen und 34 Aufgaben und Lösungen*. Lehrbuch Maschinenbau. Teubner, Wiesbaden, 2., durchges. und erw. aufl. edition, 2006.

[Rie87] H. Riedel. *Fracture at high temperatures*. Materials research and engineering. Springer-Verlag, Berlin and New York, 1987.

[RO43] W. Ramberg and R. O. Osgood. Description of stress-strain curves by three parameters: Technical note no. 902, 1943.

[SB97] C. Starling and J. Branco. Thermal fatigue of hot work tool steel with hard coatings. *Thin Solid Films*, 308-309:436–442, 1997. doi:10.1016/S0040-6090(97)00600-7.

[Sch91] R. Schmidt. *Ausscheidungsphänomene in Werkstoffen: Eine Einführung in die mathematische Modellierung ; mit 10 Tabellen*. Dt. Verl. für Grundstoffindustrie, Leipzig, 1. aufl. edition, 1991.

[Sch12] P. Schilg. Anlassen von Stählen (Vergüten), 2012. URL http://xn--werkstoffprfer-blog-gbc.de/?tag=martensit.

[Sch18] S. Schilli. *Implementierung und Validierung eines elastisch-viskoplastischen Werkstoffmodells in Abaqus/Explicit*. seminar paper, University of Applied Sciences Offenburg, 2018.

[Sei15] T. Seifert. Kontinuumsmechanik: Skript zur Vorlesung an der Hochschule Offenburg. 2015.

[Sei17] T. Seifert. Grundzüge der FEM: Skript zur Vorlesung an der Hochschule Offenburg. 2017.

[SMB+09] M. Shah, C. Mabru, C. Boher, S. Leroux, and F. Rezai-Aria. Crack propagation in tool steel x38crmov5 (aisi h11) in set specimens. *Advanced Engineering Materials*, 11(9):746–749, 2009. doi:10.1002/adem.200900044.

[SN14] R. E. Smallman and A. Ngan, editors. *Modern physical metallurgy*. Butterworth-Heinemann, Oxford, eighth edition edition, 2014.

[SR10] T. Seifert and H. Riedel. Mechanism-based thermomechanical fatigue life prediction of cast iron. part i: Models. *International Journal of Fatigue*, 32(8):1358–1367, 2010. doi:10.1016/j.ijfatigue.2010.02.004.

[SSS+10] T. Seifert, C. Schweizer, M. Schlesinger, M. Möser, and M. Eibl. Thermomechanical fatigue of 1.4849 cast steel – experiments and life prediction using a fracture mechanics approach. *International Journal of Materials Research*, 101(8):942–950, 2010. doi:10.3139/146.110363.

[SSW+07] C. Sommitsch, R. Sievert, T. Wlanis, B. Günther, and V. Wieser. Modelling of creep-fatigue in containers during aluminium and copper extrusion. *Computational Materials Science*, 39(1):55–64, 2007. doi:10.1016/j.commatsci.2006.03.024.

[SSWR08] C. Sommitsch, R. Sievert, T. Wlanis, and C. Redl. Lifetime evaluation of two different hot work tool steels in aluminium extrusion. *Computational Materials Science*, 43(1):82–91, 2008. doi:10.1016/j.commatsci.2007.07.054.

[SWHR08] C. Sommitsch, T. Wlanis, T. Hatzenbichler, and C. Redl. Creep and fatigue damage in hot work tools steels during copper and aluminium extrusion. *Key Engineering Materials*, 367:169–176, 2008. doi:10.4028/www.scientific.net/KEM.367.169.

[Sys16] D. Systèmes. *ABAQUS 6.16: Analysis User's Guide*. 2016.

[TKM01] M. Taneike, M. Kondo, and T. Morimoto. Accelerated coarsening of mx carbonitrides in 12%cr steels during creep deformation. *ISIJ International*, 41(Suppl):S111–S115, 2001. doi:10.2355/isijinternational.41.Suppl_S111.

[Tri18] D. Trischler. *Finite-Elemente Simulation des Wärmeübergangs vom Werkstück auf das Werkzeug während der Umformung*. seminar paper, University of Applied Sciences Offenburg, Offenburg, 2018.

[Tru08] S. Trute. *Einfluss der Prozesskette auf die Feinkornbeständigkeit von mikrolegierten Einsatzstählen*. Phd thesis, RWTH Aachen University, Aachen, 2008.

[VBDP05] V. Velay, G. Bernhart, D. Delanges, and L. Penazzi. A continuum damage model applied to high-temperature fatigue lifetime prediction of a martensitic tool steel. *Fatigue Fracture of Engineering Materials and Structures*, 28(11):1009–1023, 2005. doi:10.1111/j.1460-2695.2005.00939.x.

[vBE17] voestalpine BÖHLER Edelstahl GmbH & Co KG. Böhler w303: Warmarbeitsstahl, 2017. URL https://www.bohler-edelstahl.com/media/productdb/downloads/W303DE.pdf.

[VBP06] V. Velay, G. Bernhart, and L. Penazzi. Cyclic behavior modeling of a tempered martensitic hot work tool steel. *International Journal of Plasticity*, 22(3):459–496, 2006. doi:10.1016/j.ijplas.2005.03.007.

[VDI13] VDI-Gesellschaft Verfahrenstechnik und Chemieingenieurwesen. *VDI-Wärmeatlas*. VDI-Buch. Springer Berlin, Berlin, 11., aufl. edition, 2013.

[Wri08] P. Wriggers. *Nonlinear Finite Element Methods*. Springer Berlin Heidelberg, Berlin, Heidelberg, 2008. doi:10.1007/978-3-540-71001-1.

[Wüt82] C. Wüthrich. The extension of the j-integral concept to fatigue cracks. *International Journal of Fracture*, 20(2):R35–R37, 1982. doi:10.1007/BF01141264.

[ZBD08] Z. Zhang, G. Bernhart, and D. Delanges. Cyclic behaviour constitutive modelling of a tempered martensitic steel including ageing effect. *International Journal of Fatigue*, 30(4):706–716, 2008. doi:10.1016/j.ijfatigue.2007.05.003.

[ZDB04] Z. Zhang, D. Delanges, and G. Bernhart. Microstructure evolution of hot-work tool steels during tempering and definition of a kinetic law based on hardness measurements. *Materials Science and Engineering: A*, 380(1-2):222–230, 2004. doi:10.1016/j.msea.2004.03.067.

[ZDB07] Z. Zhang, D. Delanges, and G. Bernhart. Ageing effect on cyclic plasticity of a tempered martensitic steel. *International Journal of Fatigue*, 29(2):336–346, 2007. doi:10.1016/j.ijfatigue.2006.03.007.

[ZXS+11] Q. Zhou, W. Xiaochun, N. Shi, J. Li, and N. Min. Microstructure evolution and kinetic analysis of dm hot-work die steels during tempering. *Materials Science and Engineering: A*, 528(18):5696–5700, 2011. doi:10.1016/j.msea.2011.04.024.

Appendix

Derivatives

For the calculation of the derivatives the Voigt notation is used [Alt18, p. 328]. This allows symmetric 3x3 tensors to be written as 6x1 vectors. Thus, the derivations can be written with matrices rather than tensors of higher orders. Furthermore, the indexes of time-dependent variables are dispensed, since all variables apply for the time t_{n+1}.

To obtain the Jacobian (6.11) the determination of $\partial \bar{\boldsymbol{D}}/\partial \boldsymbol{Y}$ and $\partial \bar{\boldsymbol{M}}/\partial \boldsymbol{Y}$ is required and their calculation is described bellow starting with

$$\frac{\partial \bar{\boldsymbol{D}}}{\partial \boldsymbol{Y}} = \begin{bmatrix} \frac{\partial \boldsymbol{D}_{\boldsymbol{\varepsilon}^{\mathrm{p}}}}{\partial \boldsymbol{\varepsilon}^{\mathrm{p}}} & \frac{\partial \boldsymbol{D}_{\boldsymbol{\varepsilon}^{\mathrm{p}}}}{\partial \boldsymbol{\alpha}} & \frac{\partial \boldsymbol{D}_{\boldsymbol{\varepsilon}^{\mathrm{p}}}}{\partial r} & \frac{\partial \boldsymbol{D}_{\boldsymbol{\varepsilon}^{\mathrm{p}}}}{\partial \bar{\varepsilon}^{\mathrm{p}}} \\ \frac{\partial \boldsymbol{D}_{\boldsymbol{\alpha}}}{\partial \boldsymbol{\varepsilon}^{\mathrm{p}}} & \frac{\partial \boldsymbol{D}_{\boldsymbol{\alpha}}}{\partial \boldsymbol{\alpha}} & \frac{\partial \boldsymbol{D}_{\boldsymbol{\alpha}}}{\partial r} & \frac{\partial \boldsymbol{D}_{\boldsymbol{\alpha}}}{\partial \bar{\varepsilon}^{\mathrm{p}}} \\ \frac{\partial D_r}{\partial \boldsymbol{\varepsilon}^{\mathrm{p}}} & \frac{\partial D_r}{\partial \boldsymbol{\alpha}} & \frac{\partial D_r}{\partial r} & \frac{\partial D_r}{\partial \bar{\varepsilon}^{\mathrm{p}}} \end{bmatrix}.$$

As the following derivatives appear several times, new variables are introduced:

$$\frac{\partial \boldsymbol{N}}{\partial \mathrm{dev}(\boldsymbol{\sigma})} = d\boldsymbol{N}' \tag{9.1}$$

and

$$\frac{\partial \boldsymbol{N}}{\partial \boldsymbol{\sigma}} = d\boldsymbol{N}, \tag{9.2}$$

leading to

$$\frac{\partial \boldsymbol{D}_{\boldsymbol{\varepsilon}^{\mathrm{p}}}}{\partial \boldsymbol{\varepsilon}^{\mathrm{p}}} = -\boldsymbol{C} d\boldsymbol{N}', \ \frac{\partial \boldsymbol{D}_{\boldsymbol{\varepsilon}^{\mathrm{p}}}}{\partial \boldsymbol{\alpha}} = -d\boldsymbol{N}', \ \frac{\partial \boldsymbol{D}_{\boldsymbol{\alpha}}}{\partial \boldsymbol{\varepsilon}^{\mathrm{p}}} = -C d\boldsymbol{N} \boldsymbol{C} \tag{9.3}$$

and

$$\frac{\partial \boldsymbol{D}_{\boldsymbol{\alpha}}}{\partial \boldsymbol{\alpha}} = -Cd\boldsymbol{N} - \gamma \mathbf{I}.$$

The 6x1 vectors $\partial \boldsymbol{D}_{\boldsymbol{\varepsilon}^{\mathrm{p}}}/\partial r$, $\partial \boldsymbol{D}_{\boldsymbol{\varepsilon}^{\mathrm{p}}}/\partial \dot{\bar{\varepsilon}}^{\mathrm{p}}$ and $\partial \boldsymbol{D}_{\boldsymbol{\alpha}}/\partial \dot{\bar{\varepsilon}}^{\mathrm{p}}$ are equal to zero vector, whereas

$$\frac{\partial \boldsymbol{D}_{\boldsymbol{\alpha}}}{\partial r} = -\frac{2}{3}\frac{B_{\mathrm{c}}}{r^2}\boldsymbol{N} - \frac{C_{\mathrm{i}}B_{\infty} - B_{\mathrm{c}}C_{\infty,\mathrm{i}}}{\left(C_{\infty,\mathrm{i}}r^2 + B_{\infty}\right)^2}\boldsymbol{\alpha}.$$

All other derivatives are equal zero, or the zero vector. Following the same scheme, the derivatives for $\partial \bar{\boldsymbol{M}}/\partial \boldsymbol{Y}$ are calculated. The 6x6 matrix

$$\frac{\partial \boldsymbol{M}_{\boldsymbol{\alpha}}}{\partial \boldsymbol{\alpha}} = \frac{1}{C}\frac{\partial C}{\partial r}\mathrm{d}r\mathbf{I}.$$

The 6x1 vector $\partial \boldsymbol{M}_{\boldsymbol{\alpha}}/\partial r$ can be calculated by

$$\frac{\partial \boldsymbol{M}_{\boldsymbol{\alpha}}}{\partial r} = -\frac{1 + 2\frac{C_i}{B_C}r}{\left(\frac{C_i}{B_C}r^2 + r\right)^2}\boldsymbol{\alpha}\mathrm{d}r.$$

At least,

$$\frac{\partial M_r}{\partial r} = -2\frac{k}{r^3}.$$

All remaining derivatives are equal to $\mathbf{0}$, 0 respectively.

For purely elastic-plastic behavior, the deviation of the last line of the residual can be calculated by

$$\frac{\partial R_{\phi}}{\partial \boldsymbol{\varepsilon}^{\mathrm{p}}} = -\boldsymbol{C}^{\mathrm{e}}\boldsymbol{N},\ \frac{\partial R_{\phi}}{\partial \boldsymbol{\alpha}} = -\boldsymbol{N},\ \frac{\partial R_{\phi}}{\partial r} = \frac{B_{\mathrm{e}}}{r^2}$$

and

$$\frac{\partial \boldsymbol{R}_{\phi}}{\partial \phi} = 0.$$

Furthermore, the derivative of the plastic multiplier is

$$\frac{\partial \lambda}{\partial \boldsymbol{Y}} = \begin{bmatrix} \mathbf{0} & \mathbf{0} & 0 & \frac{1}{\Delta t} \end{bmatrix}^T. \tag{9.4}$$

Drawings

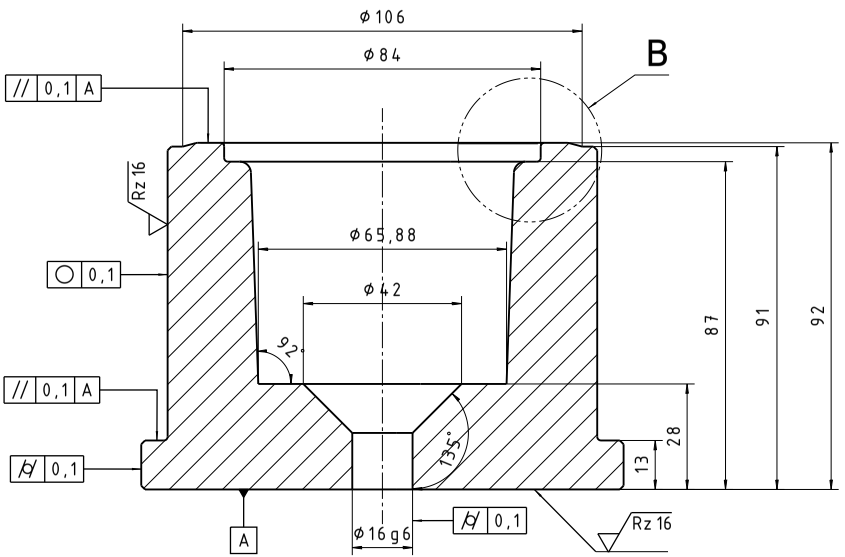

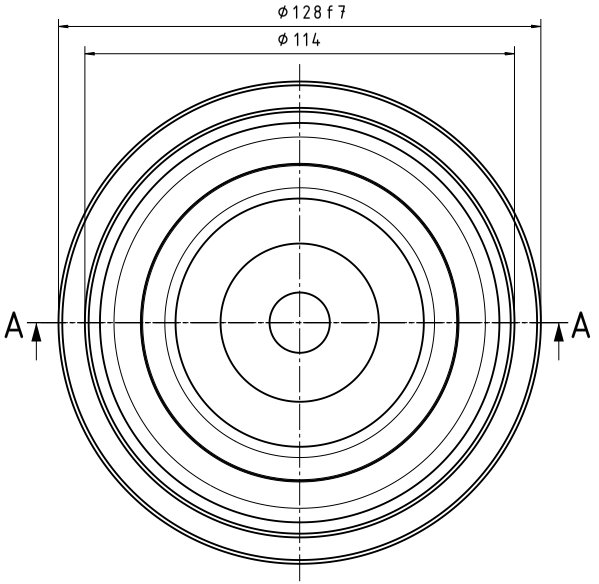

SchnittansichtA-A

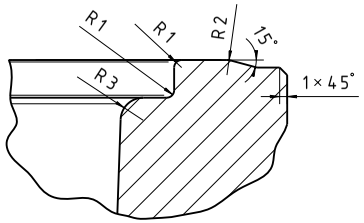

Detail B
Maßstab: 2:1

Rz 6,3 (Rz 2,5)

Oberflächen EN ISO 1302

gehärtet 54 HRC

alle nicht bemaßten Fasen 1 x 45°

Tolerierung ISO 8015		Untergesenk	
DRAWN BY Norman Heimes	DATE 30.08.2017	Allgemeintoleranzen ISO 2768-mK	Material X38CrMoV5-3 (1.2367)
CHECKED BY	DATE	SIZE A3	DRAWING NUMBER / REV
DESIGNED BY	DATE	SCALE 1:1	WEIGHT(kg) / SHEET 1/1

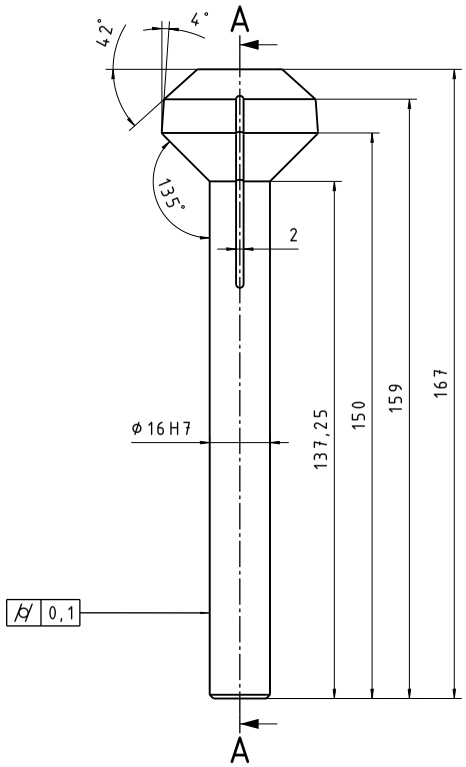

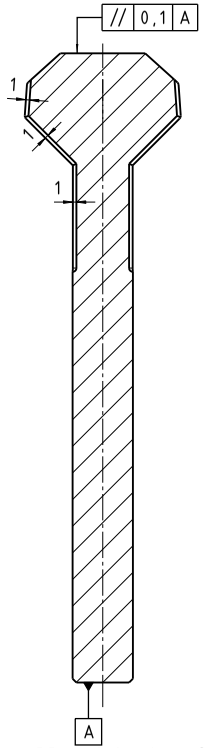

Schnittansicht A-A

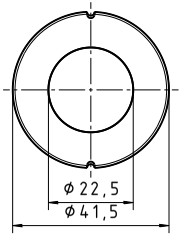

Rz 6,3 (Rz 2,5)

Oberflächen EN ISO 1302
gehärtet 54 HRC

alle nicht bemaßten Fasen 1 x 45°
alle nicht bemaßten Radien R1

Tolerierung
ISO 8015

Auswerfer

DRAWN BY: Norman Heimes	DATE: 30.08.2017	Allgemeintoleranzen ISO 2768-mK	Material: X38CrMoV5-3 (1.2367)
CHECKED BY	DATE	SIZE: A3	DRAWING NUMBER	REV: X
DESIGNED BY	DATE	SCALE: 1:1	WEIGHT(kg)	SHEET: 1/1

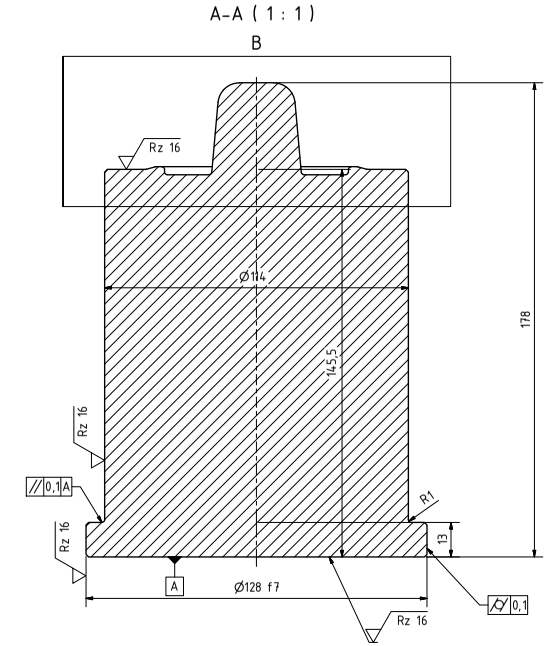

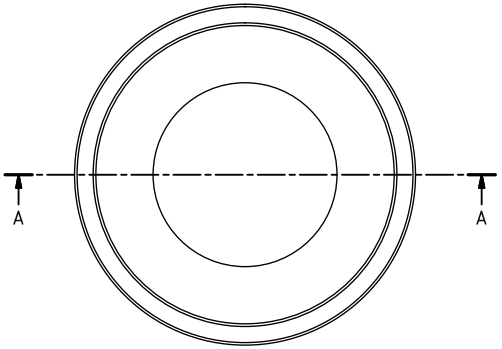

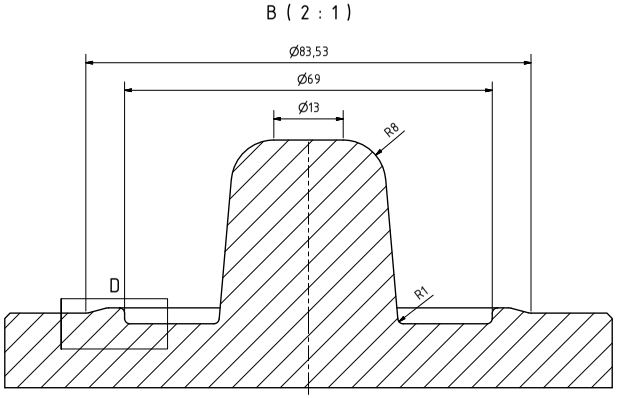

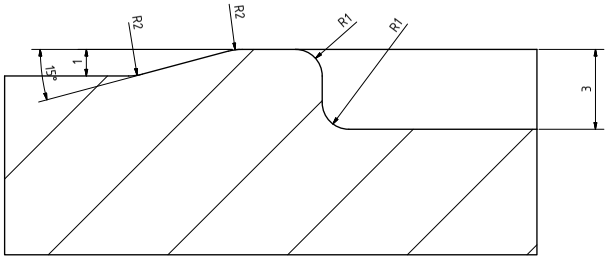

D (10 : 1)

Rz 6,3 (Rz 2,5)

Alle nicht bemaßten Fasen 1 x 45°
Oberflächen EN ISO 1302
gehärtet 54 HRC

Allgemeintoleranzen nach ISO 2768-mK				Tolerierung ISO 8015			
					Datum	Name	
				Gezeichnet	13.09.2019	Julius	
				Kontrolliert			
				Norm			
Status	Änderungen	Datum	Name				

Material: 1.2367

Obergesenk

1

A2